**Plasma Transferred Arc Additive Manufacturing Using 17-4 Precipitation Hardened Stainless Steel**

by

Sandy Ibrahim

A thesis submitted in partial fulfillment of the requirements for the degree of

Master of Science

in

Materials Engineering

Department of Chemical and Materials Engineering

University of Alberta

# Abstract

Plasma transferred arc additive manufacturing (PTA-AM) is a newly developed additive manufacturing (AM) process for the manufacturing of large industrial parts for the resource sector. A common material used in numerous industries is 17-4 precipitation hardened (PH) stainless steel, mainly due to its good corrosion resistance, ease of fabrication and an UTS of about 1310 MPa at peak age hardening. The objectives of the current research are to identify the operating parameters of 17-4PH stainless steel on the PTA-AM system. This is achieved by identifying process conditions that minimize printing defects in the final parts and identifying the printing parameters for basic shapes. The mechanical properties of printed shapes will be compared with parts manufactured using conventional processing techniques.

In the initial stages of printing, after identifying operating parameters for printing 17-4PH stainless, two types of voids were discovered in the AM parts: oxide layers and porosity. The oxide layer was attributed to the lack of continuous shielding atmosphere over the AM part while it is being printed. Supplying a continuous source of argon gas over the entirety of the part during the printing process ensured the elimination of the oxide layers. The other source of voids, porosity, was attributed to porosity in the initial powders and insufficient heat input during the printing process. Changing the powder supplier and raising the heat input during printing resulted in greatly reducing porosity in the final AM part. Peak aging was performed on the final part, with minimum defect. X-ray diffraction (XRD) and transmission electron microscopy (TEM) were conducted to verify the change of the lath martensite matrix into tempered martensite and the observed precipitated copper, respectively. No change in the martensitic matrix was noted. Hardness before and after aging was unaffected by changing processing parameters. It was demonstrated that an

operating solution to avoid oxide formation is the use of 5% hydrogen in the shielding, center and powder gas feeds.

In the second part of the project, processing parameters that yield minimum porosity and at least of comparable hardness and UTS relative to other manufacturing processes were desired. The PTA-AM system has numerous process parameters including shielding gas pressures and flowrates, current, voltage, angle of powder nozzle deposition relative to the welding direction and speed of an automated table connected to the PTA-AM system. The different combinations of the above parameters can result in a range of mechanical properties and microstructures of the AM samples. Taguchi design of experiments (DOEs) was used to identify the most influential parameters on the final mechanical properties and microstructure. Powder feed rate, current and table speed were determined to be key variables during the printing of the DOE, while all other parameters were kept constant. The printed parts had some variations, but all their mechanical properties fell within, or exceeded, the expected ranges of 17-4PH stainless steel parts manufactured with conventional techniques, before and after heat treatment. Electron backscatter diffraction (EBSD) analyses was used to verify that only a BCC microstructure is present in all stages of heat treated 17-4PH stainless printed using the PTA-AM system.

**Keywords:** Additive manufacturing; 17-4PH stainless steel; Plasma transferred arc additive manufacturing; defects; porosity; oxide layer; Taguchi design of experiments, mechanical properties

# Preface

Chapter 5 of this thesis has been published as S. N. El Moghazi, T. Wolfe, D. G. Ivey, and H. Henein, "Plasma transfer arc additive manufacturing of 17-4PH : assessment of defects," *Int. J. Adv. Manuf. Technol.*, 2020. The publication was in The International Journal of Advanced Manufacturing Technology. I was responsible for experimental work, analysis and the writing of the manuscript. My supervisors Prof. Hani Henein and Dr. Tonya Wolfe were the supervisory authors and were invovled with concept devlopment, analysis, manuscript review and editing. Prof. Ivey contributed the TEM analysis and editing.

# Acknowledgements

# Table of Contents

# List of Figures

# List of Tables

# 1 Introduction

Recent advances in many industries are resorting to different additive manufacturing (AM) techniques to print more complex parts and meet the particular needs of industry. AM processes require a 3D computer-aided design (CAD) model and additional software to define the printing sequence and path which is unique for each process. The software takes the CAD model as input and divides the desired component into 2D layers as output, typically in .G-code format which is the most widely used language for computerized machine automation. The AM machine will follow the toolpath program to reconstruct the model by depositing layers of material on top of another layer of material to produce a near-net shape part. [1]. However, the specifics of printing an AM part depend on which AM process is selected. There are seven main divisions of AM: direct energy deposition (DED) being one of them. DED is particularly widespread in many industries for its ability to both print new parts and components for damaged parts alike [2].

The plasma transferred arc welding machine is prevalently used in the oil sands and mining industries for making thick weld overlays on parts to increase the wear resistance of components in service. It has been adapted to an additive manufacturing system to print more complex and large shapes, such as pumps, nozzles and gaskets. This recent DED AM type of process, the plasma transferred arc additive manufacture ng (PTA-AM) system, has been proposed and requires the development of the understanding of the relationship between processing parameters, structure of the printed part and its subsequent mechanical properties [3].

Literature is found for many materials used for hard-facing using the PTA machine [4]–[6]; to the best of the authors' knowledge, no research was found on 17-4PH stainless steel printed using the PTA machine. The properties of 17-4PH stainless steel, including its corrosion resistance, fracture toughness and high tensile strength at temperatures up to 300°C, make it highly desirable for applications in the oil sands industry [7]–[9]. Because the selected processing parameters on the PTA-AM system vary from one material to another, the heat input and other required processing parameters required to print each specific material must be developed. Moreover, during the printing process, each material can pose a different set of printing defects. Some of the defects that arise during the printing process can be inherent to the material, to the process or to the

combination of the two [10]. Porosity due to lack of proper shielding is an example of a process related defect [11], [12], while the formation of oxide layers can be material specific [13].

This thesis will define the operating parameters required to enable the 3D printing of 17-4PH stainless steel using PTA-AM. Thus, the objectives of this thesis are as follows. First, identify the working parameters that can print a basic shape using 17-4PH stainless steel. Second, identify the defects that arise during the printing process and resolve them. Finally, test the mechanical properties of circular and square cross-sectioned tubes that were printed using the now-defined process parameters and compare them to properties of conventionally manufactured 17-4PH stainless steel.

# 2 Literature Review

Additive manufacturing is a manufacturing technique used to fabricate components through layer by layer deposition based on CAD models. This is opposed to the more conventional subtractive manufacturing techniques [3], [14] which start with a solid shape and remove material to end up with the final part. AM is gaining popularity in many industries for its ability to manufacture parts with complex designs and create products which reduce the number of individual components in an assembly. The slicing software divides the CAD model into multiple individual layers and determines the toolpath/deposition path depending on the AM process [14]. The success of a printing process is a function of the selected printing parameters and the chosen material [14]. To date, many AM processes have been successful in printing fully consolidated parts, with post processing treatments, using metals, ceramics and polymers, with mechanical properties better or equal to their counterparts that have been manufactured with conventional techniques [10].

Applications of AM can be found in many industries. In the aerospace industry, AM processes can print high strength, low density parts with very complex shapes. In the automobile industry, some manufacturers require small batches of very specific components, where it would be more cost effective to print a 3D component than to create a complex mold. In the biomedical industry, AM is gaining great recognition for its part customization capabilities that allow each patient to have implants customized based on individual needs [14]. The AM processes' capabilities are appealing to more and more industries, such as the construction, chemical and oil sands industries, due to its need for less inventory of spare parts, automation, freedom of design complexity and customization capabilities.

However, AM processes pose unique challenges. The layer by layer deposition for building each part means that the part poses anisotropic properties between its parallel and perpendicular sections. The change in phases between powder/wire from liquid to solid in each layer gives each separate layer its own thermal history. This thermal history is additionally affected by the layers below the deposited layer [10], [15]. Moreover, AM is still an expensive manufacturing technology, as compared to many conventional processes such as machining and casting. This makes it more of a challenge for industries to substitute it with conventional technologies. However, with the growing knowledge and capabilities of AM processes, the benefits of designing

and manufacturing using AM is making the business case more appealing [16]. An additional complexity of AM processes is that there are different AM processes to choose from, all with their own advantages and disadvantages. AM systems can be classified based on material feed stock, energy source and size of desired geometry [3], [10], [16].

## 2.1 AM Processes

According to the ASTM standard F2792, there are seven categories of AM processes [17]. This standard was made to overcome the lack of process categorization in the AM world, which made it difficult to identify similarities/differences between processes.

### 2.1.1 Binder Jetting

Binder jetting is an AM process that was first developed at Massachusetts Institute of Technology (MIT) in the 1990s but was only commercialised in 2010 [18]. During the printing process two materials are used: solid powders (metals, ceramics and polymers) and a liquid binder material that bonds the powders together [18]. Following the printing process, the part can be sintered to remove the binder and consolidate the part density. The biggest differentiator between binder jetting and other AM processes is that binder jetting requires post-processing treatments, such as sintering and infiltration. Moreover, binder jetting can be a relatively costly process because of all the post processing required, such as curing, de-powdering, sintering, annealing and finishing [19].

### 2.1.2 Material Extrusion

Material extrusion, also known as fused deposition modeling (FDM) or fused filament fabrication (FFF), is a process whereby thin polymer based filaments are fed through a nozzle or orifice and deposited into a desired shape given by a CAD model [1], [20]. Even though FDM is a good alternative to conventional manufacturing processes in certain structures, it can exhibit a set of geometrical inconsistencies. The accuracy and finish quality of the AM build are limited by the nozzle thickness and radius. Moreover, the accuracy and speed of material extrusion AM are relatively lower than other AM processes [1], [20].

### 2.1.3 Material Jetting

Material jetting is an AM process that creates 3D printed objects onto a build platform by spraying drops of the material [21]. Material jetting machines vary in complexity, but the principal printing method is the same in all of them. A nozzle moves horizontally across the build platform depositing drops of the material. Each printed layer is cured using ultraviolet light before the next layer is deposited [21]. Due to its method of drop deposition, material jetting AM is limited in the selection of available materials, mostly polymers and wax-like materials with very low melting temperatures.

### 2.1.4 Sheet Lamination

Sheet lamination process includes two subcategories: laminated object manufacturing (LOM) [22] and ultrasonic additive manufacturing (UAM) [2], [22]. The concept of sheet lamination is based on fusing together prefabricated sheets of the desired object. The LOM process is a layer by layer AM process often used for aesthetic purposes with paper as the raw material and adhesive as the binder between the layers. UAM uses metal prefabricated sheets and ultrasonic welding instead of the adhesive to connect the sheets together [2], [22]. Sheet lamination is a process that requires little energy since no melting is required. However, because it is a partially subtractive process, sheet lamination cannot deliver the same level of geometrical complexities as other AM processes [2].

### 2.1.5 Vat Photopolymerization

Vat polymerization, also known as stereolithography apparatus (SLA), is one of the main AM processes for polymers. The process occurs by exposing a vat of photopolymer resin to an ultraviolet laser beam, which cures the liquid monomers into solid polymers [2], [23]. The toolpath plan, developed from a CAD model, dictates the path of the UV laser beam. Like all other AM processes, controlling the process parameters (specifically the printing orientation) is a major factor in determining the quality of the AM part [23].

### 2.1.6 Powder Bed Fusion

Powder bed fusion (PBF) is one of the most common types of AM processes. All PBF processes involve the spreading of new powder, using a roller or a blade, over the previous layers [24]. The

heat source, either a laser or electron beam, is applied to melt and consolidate the powders. The powder bed gradually moves down as each layer is completed [24], [25].

As noted, PBF is classified into two types depending on the energy source: selective laser melting (SLM) and electron beam melting (EBM), shown in Figure 2-1 [25]. Both types of powder bed fusion achieve printed parts with high density, comparable mechanical properties to wrought parts and fine surface finish. However, the processes differ in toolpath planning, properties and chemistry of powder used, recoating techniques and atmosphere. SLM typically undergoes the printing process in an inert atmosphere with a cold powder bed, while EBM prints under vacuum in a powder bed with relatively higher temperatures [18]. Vacuum atmospheres are required with EBM to prevent air-electron interactions which can interfere with the electron beam and reduce beam energy [24]. *Table 2-1* shows the main differences between both processes.
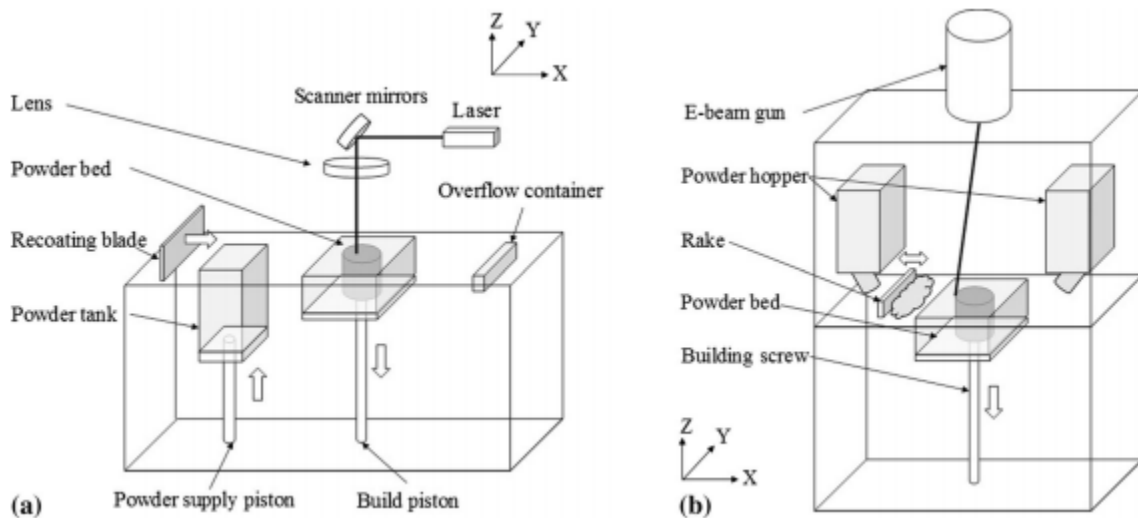


*Figure 2-1 Schematic of powder bed fusion equipment (a) selective laser melting and (b) electron beam melting [25].*

*Table 2-1 Characteristic features of SLM and EBM [26].*

|  | SLM | EBM |
|---|---|---|
| **Power source** | One or more fiber lasers of 200 to 1000 W | High power Electron beam of 3000 W |
| **Build chamber environment** | Argon or Nitrogen | Vacuum / He bleed |
| **Method of powder preheating** | Platform heating | Preheat scanning |
| **Powder preheating temperature (°C) [34,35]** | 100-200 | 700-900 |
| **Maximum available build volume (mm)** | 500 x 350 x 300 | 350 x 380(ØxH) |
| **Maximum build rate (cm³/hr)** | 20-35 | 80 |
| **Layer thickness (μm)** | 20-100 | 50-200 |
| **Melt pool size (mm)** | 0.1-0.5 | 0.2-1.2 |
| **Surface finish [7] (Ra)** | 4-11 | 25-35 |
| **Geometric tolerance (mm) [12]** | ±0.05-0.1 | ±0.2 |
| **Minimum feature size (μm) [39]** | 40-200 | 100 |

### 2.1.7  Direct Energy Deposition

Direct energy deposition is another well-developed AM process, which is especially widespread for its ability to not only print AM parts but also to repair damaged parts [2]. The process uses metal powder or wire as feedstock, which is melted using a directed energy source, and deposits the melted metal onto a substrate. The source of energy generally has a high density and can be a laser beam, an electron beam or welding arc, depending on the required application, size and surface finish required [2], [23].

### 2.1.7.1  Laser Beam

Laser engineered net shaping (LENS) is one example of a DED AM process (Figure 2-2) [2], [23]. In an inert gas chamber, a laser beam is focused on the substrate. At the same time, metal powder is deposited from a powder nozzle and directed to the same spot where the laser beam is focused,

thus melting the powder. A toolpath plan, developed from a CAD model, is used to direct the motion of the laser source based on the desired 3D shape. The first deposited track of melted powder is rapidly air cooled on the substrate, which forms the first layer of material [23], [25]. Depending on the design of the system, either the laser source moves, or the building stage moves (or both) to allow for subsequent layers to be deposited.
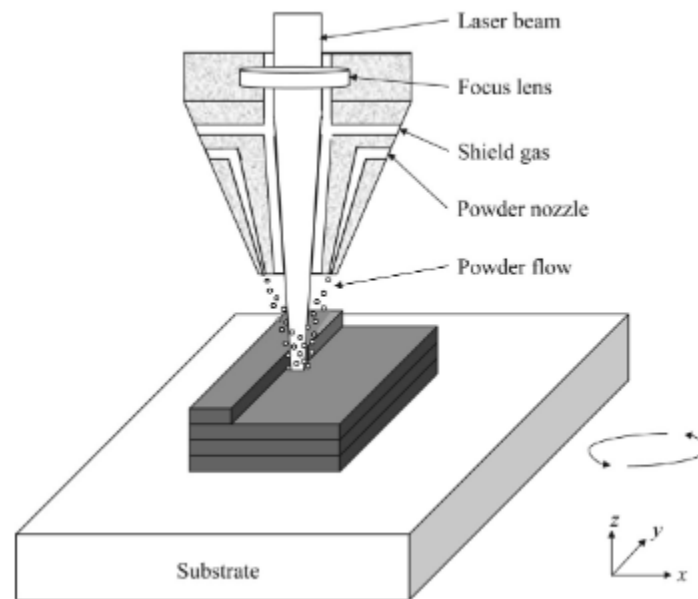


*Figure 2-2 Schematic of laser engineered net shaping process [23].*

### 2.1.7.2  Electron Beam

Electron beam freeform fabrication (EBF[3]) is another example of a DED process [2], [25]. This process uses an electron beam as the energy source and a metal wire for feedstock. The wire filament is continually fed into the electron beam and is melted and selectively sprayed onto the substrate. Electron beam is especially useful in applications requiring high accuracy and a very fine surface finish, such as required by the aerospace industry [23]. The vacuum environment allows for the printing of very reactive metals, such as titanium and aluminum since there is no interaction with atmospheric gases. However, the requirement for a vacuum environment inhibits the production of large scale AM parts [27]. Larger parts require more space for printing, and thus require more energy to achieve and maintain a vacuum environment, making the process expensive and infeasible for larger parts.

### 2.1.7.3 Wire Arc

Wire + arc additive manufacturing (WAAM) is a process that uses an electric arc as a heat source to melt a metallic drawn wire as a feedstock to print near net shape components in a layer by layer manner. The system is manipulated using a robot arm or a multi-axis table. One of the main advantages of WAAM is its ability to produce meter long builds with a relatively high deposition rate, while reducing material waste [28].

### 2.1.7.4 Plasma Arc

Plasma transferred arc welding (PTAW) is commonly used as a hard-facing technique for components susceptible to severe wear conditions in the oil sands and mining industries [29],[30]. PTAW is considered as a subcategory of plasma arc welding (PAW). Both welding processes employ a non-consumable tungsten electrode; however, the main difference is that PTAW uses powder as a feedstock that requires gas to be transported to the arc region while PAW uses wire [31].

Recently, the use of PTA as an AM process has been gaining attention in the AM world. The PTA system relies on both current and voltage for the plasma arc initiation. Current is controlled by inputting the desired current value in the system, which dictates the amount of current (electrons) that flows between the torch and the substrate. Voltage, on the other hand, is based on the difference in pressures between the torch and substrate, and it is controlled by changing the torch offset distance (distance between the torch and substrate). The plasma arc is then formed when the current ionizes the inert (plasma) gas between the torch and the substrate. In the PTA-AM system, metal powder is deposited from a powder hopper through a torch which contains the electrode and the plasma arc. The powders are melted as they are transported within the plasma arc and are deposited onto the surface. As the torch moves over the surface, the metal deposit solidifies leaving a bead of metal behind the moving arc.

Using PTA as an AM process allows for several advantages over other AM processes. The PTA-AM process is able to print parts with a homogeneous, gradation of different materials, which is not possible in other laser and electron beam AM processes. On the other hand, there is no method to ensure proportional powder delivery to the entire surface of a part in a LENS process, as limited by its use of a roller/blade technique [32][26]. Moreover, the PTA-AM can use a large range of

powder distribution, around 45-150 µm. The anticipated different microstructures of different powder sizes are not detrimental to the PTA-AM process since powders are fully melted. However, powder size distribution is more critical with LENS, for example, since powders are sintered and not melted. The PTA-AM system is also able to print bead widths up to 3 mm in thickness and only up to 0.1/0.2 for LENS/EBM processes, respectively, *Table 2-1* [26]. This allows for the faster production of same size parts using the PTA-AM system.

## 2.2  Challenges in AM

Additive manufacturing has brought many new applications and products to manufacturing and design, however, the tool does come with challenges that must be considered during the design process. Challenges in AM can include geometric stability and accuracy, cost, manufacturing time and material challenges; this thesis will only focus on material challenges. Some of the main materials challenges that commonly arise in many of the AM processes include porosity, oxide layers, excess heat, residual stress generation, balling effect and staircase effect, to be described below. All of these undesirable defects must be eliminated or greatly reduced to prevent their adverse effects on the mechanical properties of the AM part. Controlling these defects can help print more consistent and repeatable AM parts.

Porosity in AM parts can arise due to several reasons: porosity in powder, interactions between the molten droplet and atmospheric gases and improper selection of process parameters. The gas atomized powders can have entrapped gases within them that are not eliminated during the printing process and are carried through to the final AM part [10], [33]. Typically, most of the AM processes are operated under an inert gas atmosphere to prevent oxygen in the atmosphere from entering the melt pool during the welding process and forming gas porosity [34]. However, not all AM processes are operated under a complete inert atmosphere and may need additional sources of shielding (i.e. the PTA-AM process). Depending on how reactive a material is to interaction with atmospheric gases, poor shielding may result in the formation of oxide layers in the interlayers of an AM part, which can create inhomogeneity in the microstructure and mechanical properties. The final source of porosity formation is improper selection of parameters. If the heat input to the powders is not high enough, some of the powders might get transferred to the final AM part as unmelted powders and leave room for gaps to form around them [10].

Thermal gradients form in AM builds due to the continuous exposure of a heat source during the layer by layer deposition of material. The rapid heating and cooling cycles, with melting of new layers and the remelting of underlying, previously solidified layers can cause excessive thermal gradients and residual stresses in the final build [35]. It is a challenging process to determine the exact amount of heat needed to fully melt/sinter the delivered material from the feedstock (in powder or wire form). Insufficient heat input can lead to improper melting of the feedstock which can lead to adverse effects in the final build, including porosity and poor surface finish. Similarly, adverse effects of excess heat include slumping and poor surface finish [2], [16]. Additionally, residual stresses generated by the continuous rapid heating and cooling cycles of AM processes result in part distortion that can drastically affect build functionality [35].

Poor choice of process parameters can lead to other printing defects as well. A phenomenon known as the balling effect can arise during the deposition of the first layer or as a scale surface on the exterior/interior of finished builds. Balling effect can be a detrimental phenomena that occurs due to molten metal's tendency to reduce surface wettability under high surface tensions resulting in 'balls' of molten steel instead of smooth depositions [36]. It can cause the first layer to be discontinuous and produce individual spherical segments. The spherical shapes can produce an inhomogeneous deposit. If not resolved in the next few layers, they will cause delamination between the part and the substrate [37]. Moreover, metallic particles (due to the balling effect) can appear as scale on the surface of finished builds if improper selection of powder particle size, layer thickness and heat input is done [37]. To overcome the issue of delamination and the balling effect, which may additionally be due to poor substrate surface wettability (along with poor choice of process parameters), substrates are sometimes preheated. The preheating of substrates is also beneficial in reducing thermal stresses and cracking of components in some printing processes [38].

The staircase effect is created when a surface with step-like layers forms due to layer misalignment or excessive heating issues [10]. Finally, the stair effect is a phenomenon that occurs when the discrete layers of an AM part are visible and there is no complete homogeneity between the layers [37]. This leads to greater surface roughness in the final part and creates a noticeable difference in surface finish between the sides and the top surface of the part.

## 2.3 Material Properties

The numerous applications of 17-4 precipitation hardened (PH) stainless steel in many industries have led it to be extensively studied due to its superior mechanical properties and corrosion resistance. Additionally, its service temperature can go as high as 300°C, making it an excellent candidate for high temperature process applications [9]. These superior properties are mainly attributed to the martensitic matrix of 17-4PH stainless steel and the precipitation of copper upon heat treatment. By weight percent, 17-4PH stainless steel nominally contains the chemical composition given by ASTM A564 in *Table 2-2* [39]. The balance is iron. Depending on the temperature and time of the heat treatment, the mechanical properties resulting in tensile strength, ductility and impact strength can be controlled [40].

*Table 2-2 Chemical composition of 17-4PH stainless steel [39].*

| | | | | | | Composition, wt% | | | | | | | |
|---|---|---|---|---|---|---|---|---|---|---|---|---|---|
| UNS Designation | Type | C | Mn | P | S | Si | Cr | Ni | Al | Mo | Ti | Cu | Other Elements |
| S17400 | 630 | 0.07 | 1.00 | 0.04 | 0.03 | 1.00 | 15-17.5 | 3-5 | … | … | … | 3-5 | c |

c Niobium 0.15-0.45

### 2.3.1 Heat Treatment and Matrix

The heat treatment of 17-4PH stainless steel to obtain the good mechanical properties initially requires a solution treatment followed by an aging heat treatment (Figure 2-3) [41]. The solution treatment involves raising the temperature of the stainless steel to 1040°C then air quenching to room temperature. Raising the temperature to 1040°C dissolves the copper in the solution, while air quenching supersaturates it to room temperature and a lath martensitic matrix is expected. The properties of the stainless steel are determined by the time and temperature of the subsequent aging heat treatment process. Peak aging is found to occur after 1 hour at 480°C. Further aging, by increasing either temperature or time, leads to the overaging of copper precipitates and increased toughness/ductility in the stainless steel but lower tensile strength [9], [42]–[45].
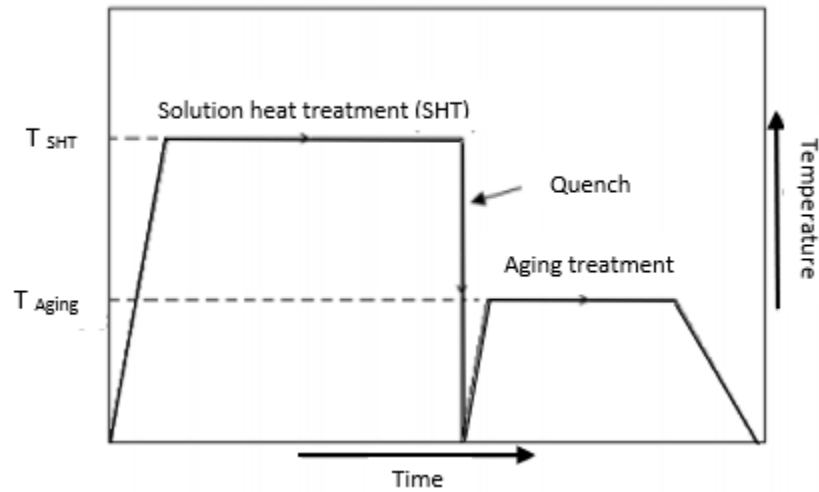
*Figure 2-3 Diagram showing the three steps of precipitation hardening [41].*

Upon aging the 17-4PH stainless steel, the lath martensite is transformed into tempered martensite. At this stage, the high tensile strength of the stainless steel, and the high hardness, are mainly attributed to the precipitated copper and not the tempered martensitic matrix [40], [46]. Interestingly, in 17-4PH multiple sources have referred to the reversion of austenite well below the $A_{C1}$ temperature [40], [42], [44], [46]. Although one of the studies tested the $A_{C1}$ temperature to be at 725°C after solutionizing, austenite was found to reform below 600°C. Multiple sources have attributed this to several factors. Primarily, increasing amounts of copper (and nickel) are theorized to depress the austenite to martensite transformation temperature allowing austenite to reform at lower temperatures. Secondly, copper in its overaged phase is an FCC structure and is thought to be a nucleation site for the formation of austenite, due to their similar FCC structures. However, not all sources agree. Some claim that the final matrix has retained austenite, while others claim that only martensite and ferrite are observed [28], [47], [48]. This could be attributed to the initial chemical composition of 17-4PH stainless steel that is used. Although 17 refers to the nickel content and 4 refers to the chromium content, both numbers come within a range by each supplier. According to the Schaeffler diagram (*Figure 2-4*), minor changes in the chemical composition of the material being studied can lead to changes in the matrix, where the ranges are given in *Table 2-2*.
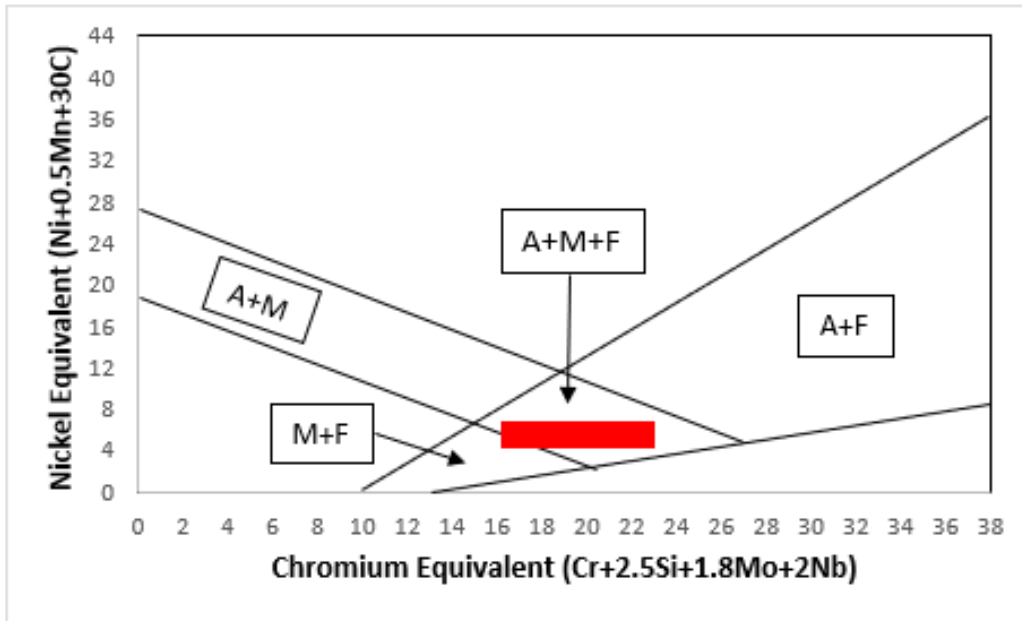
*Figure 2-4 A reproduction of the Schaeffler diagram showing the different expected microstructures based on nickel and chromium equivalents [43]. Presented are the stable phases of stainless at room temperature (with different compositions) after solutionizing for 30 minutes at 1050°C. The red rectangle marks the range of composition for the 17-4PH stainless steel used in the following chapters.*

Moreover, the type of martensite after heat treatment was anticipated by many to change from lath martensite to tempered martensite. However, it is unclear how the distinctions between both matrices are made, or if there is truly a difference between both. Especially that the lattice structures of both lath martensite and tempered martensite are closely related due to the low carbon content in the 17-4PH stainless steel [45], [49]–[51]. The tempering of the martensitic matrix is mainly desired to help release stresses from the matrix.

## 2.4 Conventional Manufacturing of 17-4PH Stainless Steel vs. AM Manufacturing

As an established engineering alloy, 17-4PH stainless steel has standardized heat treatments that are performed on wrought and cast alloys to ensure the consistency of the final microstructure. However, the effect of these standardized treatments towards AM built components is not completely clear. The thermal cycling in AM processes as each layer is deposited far exceed the

typical cooling rates in conventional manufacturing techniques of 17-4PH stainless steel [47]. The complexities of an AM process have rapid cooling effects on the solidification process of 17-4PH stainless steel, leading to microstructural heterogeneities and anisotropy. It was found that repetitive deposition of new layers in an AM process can lead to different degrees of thermal cycles [38]. Hence, during deposition, some areas can experience aging, underaging and overaging of precipitates. Comparative studies have been conducted on the processing of 17-4PH stainless steel using AM and conventional manufacturing techniques [28], [47]. The different manufacturing techniques have induced different microstructures and manufacturing defects, as will be further discussed. Moreover, different processing parameters, in either manufacturing technique, have been analyzed to understand their influence on the final 17-4PH stainless steel part.

The influence of heat treatments on the microstructural evolution of selective laser manufactured (SLM) and wrought 17-4PH stainless was compared [47]. XRD analysis was conducted on the microstructures on the SLM samples and the wrought samples in the as-built/as-received conditions, after solution treatment and after peak aging [47]. Because of the very low carbon content in 17-4PH stainless steel, the magnitude of lattice distortion in the BCT martensite phase is very small, making it indistinguishable from the delta ferrite's BCC lattice structure [47]. Hence, during the XRD analysis, both the peaks of the martensite and delta ferrite were considered as BCC peaks. The XRD results obtained from samples produced by SLM and wrought manufacturing techniques are shown in Figure 2-5. The microstructure of the as-received and solutionized wrought samples revealed a single BCC peak (110). Peak aging the wrought samples led to the formation of a small FCC austenite (111) peak. The AM as-built samples showed small FCC (111) peak before any heat treating conditions along with the ferrite BCC (110) peaks. Solutionizing the SLM samples led to the elimination of the FCC (111) peaks. Peak aging the samples led to the reformation of some austenite FCC peaks [47]. The difference in microstructure between both processes can have defining effects on each respective parts' mechanical properties, where the martensitic matrix is characteristic of 17-4PH stainless steel's higher tensile strengths and hardness, along with the copper precipitates.
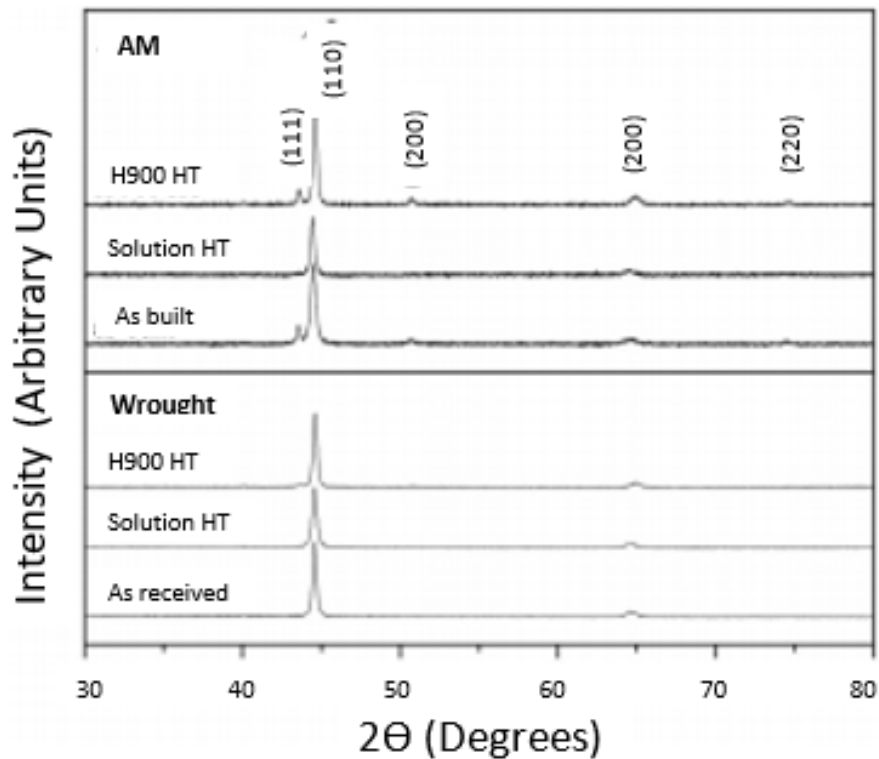
*Figure 2-5 XRD data from the as-built/as-received and heat treated 17-4PH stainless steel samples [47].*

It was reported that the microstructure of 17-4PH stainless steel is highly affected by the selected processing conditions during the printing process using AM techniques [38], [47]. Laser power affects the presence of retained austenite, as well as the chemical composition of the shielding gas used during an AM process. Using nitrogen in the shielding gas led to 50-75% volume fraction of retained austenite, as compared to only 8% volume fraction when only argon gas is used. One study showed that 17-4PH stainless steel built using a laser density of 61 $J/mm^3$ resulted in a fully columnar grain microstructure, while using a laser energy density of 107 $J/mm^3$ in another study resulted in fine blocks of martensite. The fine blocks of martensite were attributed to the presence of retained austenite at the grain boundaries which inhibited the growth of the martensite [52]. However, wrought 17-4PH stainless does not exhibit this microstructure dependable behavior on shielding gas/process parameters chemical composition. It was finally deduced that only post processing heat treatments would result in similar microstructures between AM and wrought 17-4PH stainless steel [47].

The effect of different process variables, mainly shielding gas composition and post processing heat treatment, on 17-4PH stainless printed using wire arc additive manufacturing (WAAM) was studied [28]. Two shielding gas chemical compositions were used: 38% He and 2% $CO_2$ in argon gas (higher heat input and referred to as SG1) and 2.5% $CO_2$ in argon (lower heat input and referred to as SG2). Different heat treatments were applied to samples deposited using both gas chemical compositions: as-deposited (AD), as-deposited and solution treated (AD+ST), as-deposited and peak aged (AD+H900) and as-deposited, solution treated and peak aged (AD+ST+H900) [28].

The thermal cycling due to the layer deposition of the AM process resulted in a heterogeneous microstructure in the AD condition. The solidification path of 17-4PH stainless steel from liquid state results in the formation of delta ferrite to austenite+delta ferrite to martensite+delta ferrite. Delta ferrite is the primary phase formed because 17-4PH stainless steel has a Cr/Ni ratio greater than 1.5. A chromium to nickel ratio is used to indicate the primary phase to form upon solidification, a ratio over 1.5 indicates primary ferrite, while a ratio lower than 1.55 indicates primary austenite formation [53]. The fast cooling rate of a DED AM process prevents the complete transformation of delta ferrite to gamma austenite, critically relying on solid state diffusion to allow for a phase transformation [28]. This explains why the microstructure of an AD part is a dendritic martensitic matrix with interdendritic delta ferrite. The average UTS of an AD part was found to be 994 MPa, as listed in *Table 2-3*. The AD+ST sample results in microstructural homogenization, because there is sufficient time for dissolution of all precipitates (such as copper or niobium carbides). After the solution treatment, a 100% martensitic lath microstructure was obtained since the slow cooling promotes the complete transformation from delta ferrite to austenite to martensite. AD parts show higher hardness results than ST parts; however, with standard deviation, they both have the same range of ultimate tensile strength, *Table 2-3* [28].

17

*Table 2-3 Tensile results from different heat treatments  of 17-4PH stainless steel [28].*

| Condition | Sample direction | PS (MPa) | Std Dev | UTS (MPa) | Std dev | Elongation % | Std dev |
|---|---|---|---|---|---|---|---|
| **AD** | **Average** | **790** | 73 | **994** | 39 | **11.9** | 0.6 |
| | Vertical | 738 | 30 | 979 | 13 | 12.2 | 0.7 |
| | Horizontal | 842 | 65 | 1009 | 55 | 11.6 | 0.3 |
| **AD+ST** | **Average** | **821** | 17 | **1003** | 6 | **12.6** | 0.4 |
| | Vertical | 827 | 4 | 1006 | 6 | 12.4 | 0.4 |
| | Horizontal | 815 | 24 | 1000 | 5 | 12.8 | 0.2 |
| **AD+H900** | **Average** | **1099** | 57 | **1208** | 95 | **7.3** | 1.2 |
| | Vertical | 1059 | 9 | 1124 | 5 | 6.5 | 0.3 |
| | Horizontal | 1140 | 57 | 1293 | 32 | 8.2 | 1.3 |
| **ST+H900** | **Average** | **1229** | 31 | **1352** | 8 | **13.8** | 0.9 |
| | Vertical | 1234 | 33 | 1351 | 11 | 13.8 | 0.5 |
| | Horizontal | 1225 | 36 | 1353 | 6 | 13.8 | 1.4 |
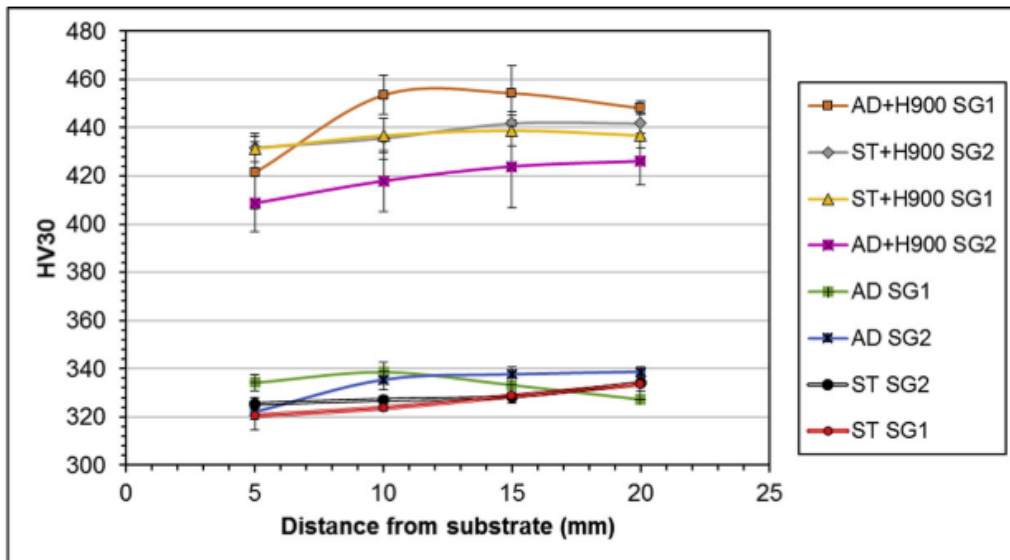


*Figure 2-6 Hardness results based on different heat treatments and different shielding gas composition. SG1 has 38% He and 2% C with a balance of Ar, while SG2 has 2.5% C with a balance of Ar [28].*

Results from AD+ST+H900 gave the highest tensile properties (1352 MPa) due to the homogenization of the microstructure. Conventionally manufactured 17-4PH stainless steel results in a UTS of 1310 MPa and 10% elongation, while AD+ST+H900 had a UTS of 1352 MPa and elongation of 13.8%. However, AD+H900 showed slightly higher hardness results than AD+ST+H900, *Figure 2-6*. Delta ferrite can also experience an increase in hardness as a consequence of the nucleation and growth of copper precipitates [28]. Additionally, thermal cycling during deposition explains why AD+H900 had higher hardness than AD+ST+H900, because ST resulted in the dissolution of precipitated particles. They concluded that obtaining tensile properties similar to wrought 17-4PH could only be achieved after ST was conducted before H900. ST guarantees a homogeneous microstructure and the dissolution of most segregated elements into solid solution, including copper and niobium particles that may have prematurely precipitated [38]. Moreover, they verified that using shielding gases which lead to higher heat inputs (i.e. the addition of helium) will cause slower cooling rates and thus yield less austenite and more martensite in the final structure. For the volume expansion from austenite to martensite to occur, plastic deformation must take place. Higher heat input delivered during printing will result in larger grains; larger grains require less yield stress to complete the transformation from austenite to martensite. Thus, higher heat inputs will result in more martensite in the final microstructure. Using helium as part of the shielding gas resulted in 0.12% area percentage retained austenite, as opposed to 0.85% with its counterpart, in the AD condition [28].

The effect of powder atomization techniques and various heat treatments on the final microstructure and mechanical properties of metal injection molded (MIM) 17-4PH stainless steel parts was analyzed [54]. It was found that water atomized powders had a much higher oxygen content (*Table 2-4*) as compared to gas atomized powders. Higher silicon and oxygen contents in the water atomized powders led to more $SiO_2$ inclusions, allowing the gas atomized powders to have superior mechanical properties. Peak aging heat treatments resulted in the highest tensile properties and elongation greater than 8%, irrespective of the atomization method. Mechanical properties of as-sintered and solution treated parts had lower mechanical properties as compared to those peak aged [54].

*Table 2-4 The carbon, nitrogen and oxygen contents and sintered densities of the two 17-4PH stainless steels after sintering [54].*

| Powder | Sintered Density (g/cm$^3$) | C (wt%) | N (wt%) | O (wt%) |
|---|---|---|---|---|
| W | 7.58±0.02 | 0.01725 | 0.00108 | 0.09824 |
| G | 7.66±0.03 | 0.02510 | 0.00120 | 0.00391 |

Other studies in the literature portray some types of defects that can occur with 17-4PH stainless steel made with conventional manufacturing techniques that are not experienced with AM techniques. The effects of casting porosity on the mechanical properties of investment cast 17-4PH stainless steel were analyzed [55]. Casting shrinkage porosity of 10% was found to reduce the ductility of peak aged 17-4PH stainless steel by 80%, portraying how detrimental casting shrinkage porosity can be on ductility. However, they concluded that the decrease in tensile strength of the alloy is not directly proportional to the overall part porosity but on the local porosity found on the fracture surface of tensile samples. Fracture occurs preferentially in locations with high local porosity, even if the bulk porosity in the sample is not high. Hence, casting shrinkage porosity has a very heightened effect on poor ductility but not on overall tensile strength [55].

## 2.5 Literature Review Summary

Selection of processing parameters in AM techniques plays a pivotal role in the final microstructure [47], and resultant mechanical properties, of the final 17-4PH stainless steel AM part [28], [38], [47]. This is opposed to parts manufactured using conventional techniques, which have defined microstructures based on the well-documented and standardized heat treatments of 17-4PH stainless steel. Moreover, the studies show that some defects can be inherent to AM processes, such as porosity caused due to improper selection of processing parameters, or they can be inherent to conventional manufacturing techniques, such as casting defects [55]. They can also appear in either technique if they were defects present in initial powders [54] or depend on the chemical composition of the shielding gases used [11].

Additionally, the requirement for production of large-scale AM parts for the resource, energy and mining industry cannot be tackled by all AM processes. Some processes inherently cannot produce AM parts using only metals (such as FFF or Vat Photopolymerization). Other processes are not

readily capable of producing large scale parts required for this particular industry, such as PBF processes. For those reasons, the PTA-AM system is a suitable AM process for the delivery of larger scale metal AM parts. However, no information in literature is found on the printing of 17-4PH stainless steel using the PTA-AM system. Process parameters, processing defects and final parts' mechanical properties are all unknown for the combination of 17-4PH stainless steel with the PTA-AM system. This thesis will identify the PTA-AM process parameters required to print basic shapes using 17-4PH stainless steel, with mechanical properties comparable to or greater than those produced by conventional manufacturing.

# 3 Experimental Procedures

The general apparatus and experimental procedures are highlighted in this section. Subsequent chapters will build upon these procedures based on the problem under evaluation.

## 3.1 Plasma Transferred Arc System

The AM process studied in this thesis is the plasma transferred arc additive manufacturing (PTA-AM) system, using a Kennametal Starweld 400A (PTA-AM) system (Figure 3-1) integrated with a 3-axis motion gantry table. The torch is stationary, and the gantry system controls the travel speed of the x- and y-directions according to the toolpath plan. The gantry platfrom drops in the z-direction after each layer is completed. When the integrated gantry system is not selected, the PTA system has basic travel features found in this commercial system, such as carriage/torch travel speed, torch oscillation width and speed, and arc length control (ALC) which control the stand off distance between the torch and the workpiece, (Figure 3-2). The control pendant allows for the selection and modification of parameters such as voltage, current, powder feed rate, dwell time, number of steps (if a multilayer part is being printed), and the length and width of the deposit. The pressure of the gas cylinder responsible for the center gas, shield gas and powder gas is set to 240 kPa (35 PSI). The individual gas flow rates are each manually set to the desired value, which is material specific, located on the Starweld 400A power supply console (Figure 3-3). The range of parameters that were used during the printing of AM parts in this thesis are listed in Table 3-1.

## 3.2 Integrated Motion Gantry System

A 3-axis motion gantry was integrated with the commercial PTA system to create the PTA-AM system. With the gantry system, the torch is stationary and the carriage/torch speed and oscillator speed are disabled. (Figure 3-4). The motion gantry is integrated into the PTA control panel, such that the process parameters and motion is controlled by a single computer. The motion of the gantry system is controlled by KMotion, a CNC software that translates G-code into machine motion. In the G-code used in this experiment, parameters such as the three-axis speeds of the table can be controlled, along with the powder feed rate, current and pilot arc initiation. Examples

of G-codes used for different geometries are given in Appendix A. The range of speeds of the x-, y- and z-axis of the 3D table are given in Table 3-2.
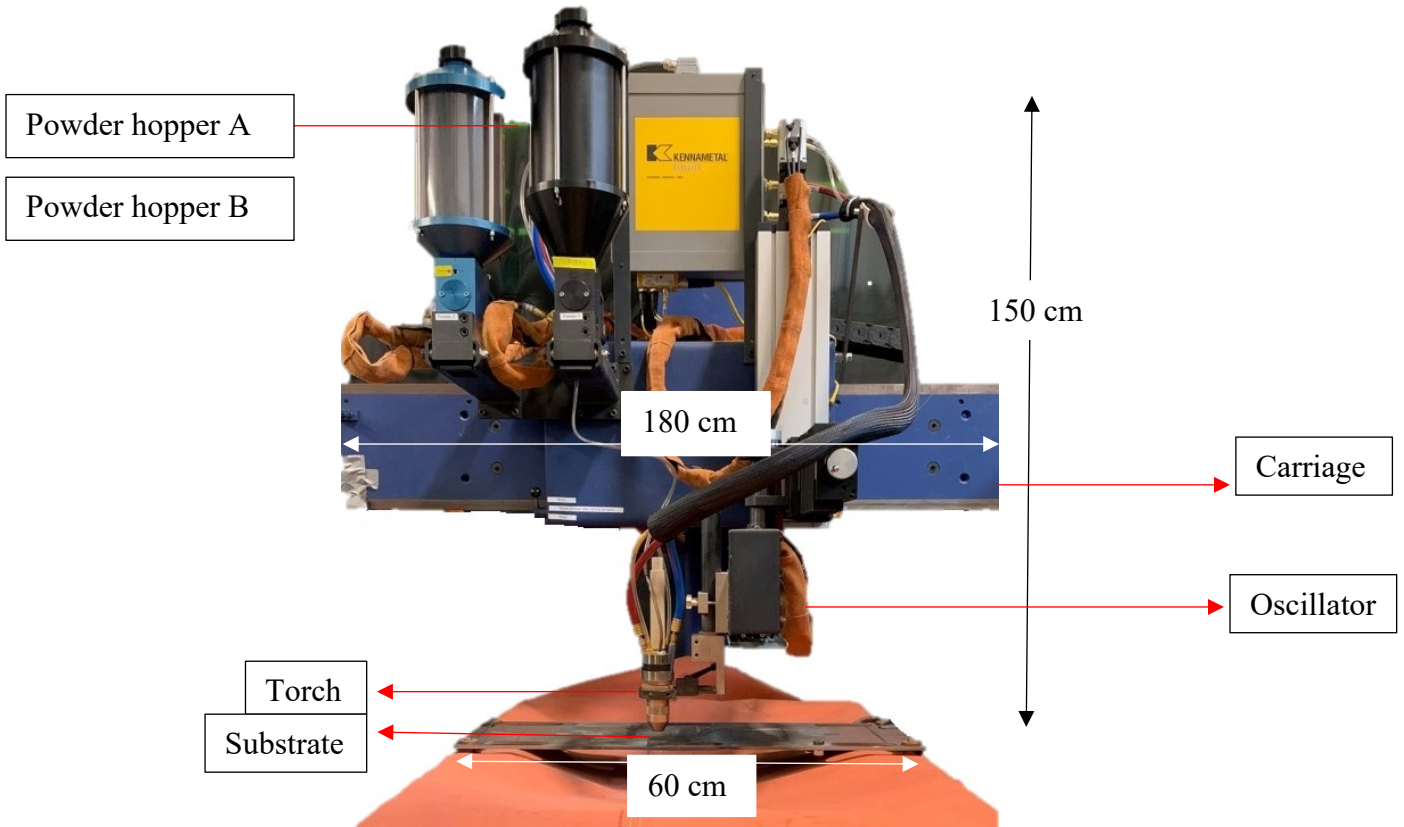


*Figure 3-1 Photograph of the PTA-AM system, when only the commercial movement parameters are selected.*



*Figure 3-2 Photograph of the Kennametal control panel.*

*Figure 3-3 Photograph of the Starweld 400A power supply console.*

*Table 3-1 Range of process parameters used in PTA-AM trials.*

| Parameter | Range of values |
|---|---|
| Carriage speed | 1-4.2 mm/s (2.5-10 in/min) |
| Oscillator speed | 12.7-17 mm/s (30-40 in/min) |
| ALC | 23-35 V |
| Powder feed rate | 25-175 g/min |
| Current | 50-180 A |
| Dwell time | 0-0.2 s |
| Center gas | 0.001-0.0025 $cm^3$/min (1-2.5 lpm) |
| Shielding gas | 0.001-0.0025 $cm^3$/min (1-2.5 lpm) |
| Powder gas | 0.01-0.015 $cm^3$/min (10-15 lpm) |
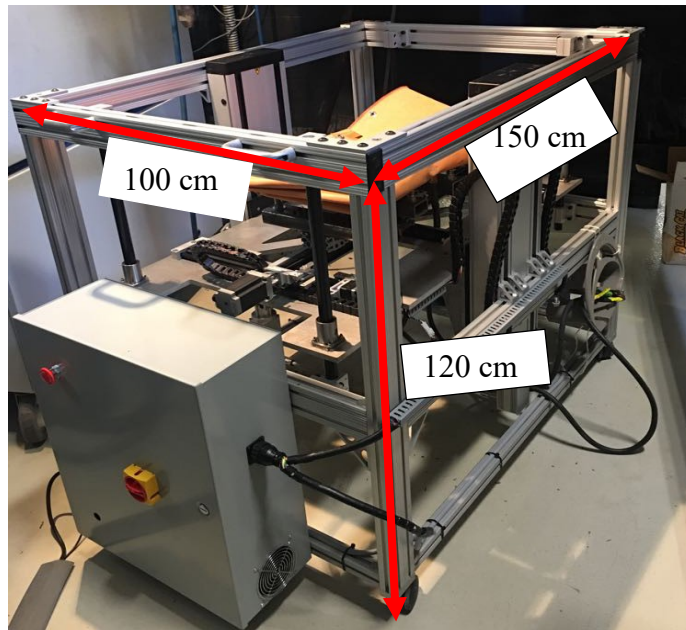
*Figure 3-4 The 3-axis integrated motion gantry table.*

*Table 3-2 Range of speeds for the motion table.*

| Axes | Speed Range |
|---|---|
| X-axis range | 0-90 m/min |
| Y-axis range | 0-90 m/min |
| Z-axis range | 0-9 m/min |

## 3.3 Powder Feeding Systems

The Kennametal PTA system is designed with two powder hoppers (Figure 3-1), in order to enable deposition with either one or two different materials. Only one hopper was used in these experiments. The powder feed rate was calibrated daily, as well as when the powder type was changed. The calibration is complete once the desired powder feed rate is reached to an accuracy of two decimal places. It is important to calibrate the system each time a different powder is used because the difference in powder densities plays a role in the powder calibration.

## 3.4  Substrates

Non-preheated, hot rolled, low carbon steel plates were used as substrates for the deposition of the AM samples. A range of sizes of carbon steel plates were used throughout the experiments: 5.08x20.32x1.27 cm (2"x8"x0.5") plates, 10.16x20.32x1.27 cm (4"x8"x0.5") plates, 10.16x15.24x1.27 cm (4"x6"x0.5") plates and 15.24x15.24x0.635 cm (6"x6"x0.25") plates. Initially, the plate sizes were not kept constant. It was realized early on that the dimensions of the plate played a role in the dissipation of heat during the deposition process, so that the plate dimensions were kept constant for each set of unique experiments to ensure the reproducibility of the build. The initial work that will be described in Chapter 5 of this thesis was printed on hand ground 5.08x20.32x1.27 cm (2"x8"x0.5") plates, while the work conducted in Chapter 6 was printed on sandblasted 15.24x15.24x0.635 cm (6"x6"x0.25") plates. However, initial printed layers did not show any difference in wettability between both surfaces.

### 3.4.1  Pre-heating of Substrates

Preheat of the substrates was studied to determine the influence of preheating on part build consistency. Non-preheated plates reached a temperature of 200°C after the welding process, which was measured using a Type K thermocouple.  The temperature measurement was taken from the surface of the substrate after a typical printing run was complete and the plasma arc was turned off (heat input was 180 J/mm). For this reason, 200°C was selected as the preheating temperature. A furnace was preheated to 200°C, and a substrate was placed inside until its surface temperature reached 200°C then left to soak for 20 minutes. The substrate was taken out and immediately used for the printing process. No visual difference was observed in the AM parts with preheated versus non-preheated substrates, the adhesion between the deposited melted powder and substrate was unaffected. For this reason, preheating substrates was not used in any of the experimental procedures described in this thesis.

## 3.5  Gases

The gas type used for all three gas ports (center, shield and powder) in the PTA-AM system is typically only argon gas with a purity of 99.999%. An example of the range of gas flow rates used in the initial experiments with 17-4PH stainless steel is given in Table 5-1. , The effect of gas

composition on the deposition process was explored. Nitrogen gas with a purity of 99.999% was used for the powder gas, while argon gas was used for the center and shield gases as used in other work [11], [12], [56]. The addition of 5% $H_2$ to 95%Ar gas mix (99.99% purity) for all three gas ports (center, shield and powder gases) was also explored.

To increase the volume of the inert environment surrounding the deposition, a shielding hood was designed. The size and design of the shielding hood are described in Chapter 5. The use of the shielding hood supplements the smaller, more local shielding protection that comes directly from the torch. To ensure homogeneity of gas distribution, aluminum wool was placed in the shielding hood. The shielding hood was connected to a separate argon cylinder. The shielding hood gas pressure ranged between 240-275 kPa (35-40 PSI).

## 3.6  Metal Powders

The metal powder with the composition of 17-4PH stainless steel was obtained from two different suppliers (Supplier A and Supplier B) and were both gas atomized. The powder from Supplier A had a size range of 53-125 μm, whereas the size range for Supplier B was 45-105 μm. Both size ranges were suitable for the narrow powder ports in the PTA-AM system and did not result in any blockages as the ideal size range for PTAW is 45-180μm. The powder ranges were provided by each supplier; however, no powder distribution was given for either powder. Table 3-3 gives the nominal composition of the powders as provided by the suppliers. Supplier B's nominal composition was similar to Supplier A's powder nominal composition with the exception of the oxygen and nitrogen contents. Supplier B was 0.06 wt.% max for oxygen and 0.02 wt.% max for nitrogen. Supplier A's powder was used for the initial experiments in the thesis; however, Supplier B was the powder supplier used for experiments in both Chapters 5 and 6.

## 3.7  Metallurgical Characterization

To evaluate the microstructure of the deposited samples, coupons were sectioned using a band saw and a silicon carbide blade. The coupons were hot mounted with a thermosetting phenolic powder in a 1.25" (31.75 mm) mould. The sample preparation included grinding and polishing procedures on the EcoMet 250 Buehler polisher/grinder: 80 grit paper, 240 grit paper, 600 grit paper, 800 grit paper, and then polished at 9, 6, 3 and 1 um polycrystalline diamond suspension, respectively.

*Table 3-3 Nominal Chemical composition of 17-4PH stainless steel powders, wt%.*

| Element | Supplier A |
|---------|------------|
| C | 0.01 |
| Mn | 0.2 |
| Si | 0.3 |
| Cr | 16.4 |
| Ni | 4.1 |
| Mo | 0.01 |
| Cu | 4.3 |
| S | n.d. |
| P | 0.007 |
| Nb+Ta | 0.3 |
| O | 0.04 |
| N | 0.03 |
| Fe | Bal. |

Samples were observed using an Olympus BX-UCB optical microscope. Images of the microstructure, porosity and oxide layer were captured. The chemical composition of the oxide layers was analysed with an energy dispersive x-ray (EDX) spectrum on the scanning electron microscope (SEM) Zeiss Sigma 300 VP-FESEM. The SEM was operated with 15kV and a working distance of 8.0 mm; it was used to image the mounted powder particles to observe the particles morphology, sphericity and internal porosity. The images analyzed using Fiji Image J, version 1.8.0_172, image analysis software quantify the porosity and oxide layers within each sample.

Hardness testing was conducted on the surface of the polished samples using the Wilson VH3100 hardness machine with a load of 1 kg and an indentation time of 5s. Depending on the size of the samples, a matrix of 5x5 points was tested with 2 mm between each indent. Else, a line of five data points was tested with 2 mm between each point.

For microstructural analysis, Kalling's reagent was used (1.5g $CuCl_2$ + 33ml $H_2O$ + 33ml HCl + 33ml ethanol) at room temperature and to reveal a matrix of martensite and ferrite [57]. Samples were immersed in the reagent, and etching times varied between 3 to 7 seconds.

X-ray diffraction (XRD) was used to characterize the microstructure. A Rigaku Ultima IV XRD system was utilized with a Cu x-ray source, operated at 40 kV and 44 mA.

To study the copper precipitates after the samples were subjected to various heat treatments, transmission electron microscopy (TEM) and EDX spectroscopy in a JEOL JEM-ARM 200CF TEM, operated at 200 kV, were used.

## 3.8  Aging

The heat treatment of 17-4PH stainless steel is conducted to allow for the precipitation of copper particles and the tempering of the lath martensitic matrix. Depending on the required strength and hardness of the 17-4PH stainless steel, the time and temperature of the heat treatment is varied. The solution heat treatment is conducted prior to peak aging, at 1040°C for 0.5 hrs in an ElectroFuel vacuum furnace. The samples were then left to cool to room temperature inside the furnace by backfilling it with argon gas. The aging heat treatment followed well-established conditions to achieve peak aging, which is 480°C for 1hr [46]. Samples were left to air cool after the heat treatment. Samples following both peak aging, and solutionizing followed by peak aging in order to compare the effect of various heat treatments on the microstructure and mechanical properties.

## 3.9  Mechanical Property Evaluation

The tensile samples were made in accordance with ASTM E8 standards [58] and a subsidized version of ASTM SS-25, ASTM SS-12.5 [59]. The ASTM SS-25 is based off the smallest tensile flat samples in the ASTM E8/E8M standard. The yield strength, UTS, elongation and reduction of area were measured using an Instron 8501 with a strain rate of 0.25 mm/min.

## 3.10 Taguchi Design of Experiments

A Taguchi design of experiments (DOE) was selected to conduct a set of concise experiments that can determine the influence of the different process parameters on the final AM sample. Taguchi DOEs are typically used instead of the more time consuming full factorial experiments. Depending on the number of process parameters, and the level of each parameter, a Taguchi DOE is selected. A set of 18 experiments following Taguchi's L'18 DOE, based on eight process parameters that were to be tested. The process parameters were offset distance between substrate and torch, center gas, powder gas, shield gas, nozzle angle, powder feed rate, current and table speed. All parts were printed on 15.24x15.24x0.635 cm (6"x6"x0.25") substrates. The samples were metallurgically characterized following the methods in sections 3.7-3.9. Results from the walls' L'18 experiment were collected and analyzed on Minitab using signal to noise ratio equations to rank the influence of each process parameter. The second set of experiments only used three process parameters to limit the variability that occurs when varying eight process parameters, this ensures reproducibility and repeatability. The three selected process parameters were ranked the most influential from the L'18 DOE, requiring a set of nine experiments to be conducted based on Taguchi's L'9 DOE. This was conducted to hone in on the influence of varying the three selected parameters on final mechanical properties and microstructure.

The next chapter of this thesis, Chapter 4, will explain how some of the above experiments were used to begin the early trial printing stages of 17-4PH stainless steel on the PTA-AM machine. The results go through the different outcomes of using different process parameters, shielding gases and powder quality on the final printed AM part.

# 4  Results and Early Trials

The following chapter is going to explain the early experimentation that was conducted to understand the complexity of depositing 17-4PH stainless steel using the PTA-AM system. Early trials were conducted to determine the initial working parameters of the PTA-AM system with 17-4PH stainless steel. The effect of various processing parameters and different shielding gases on the internal microstructure was identified.

## 4.1  Selection of Range of Process Parameters

As there was no literature found describing deposition of 17-4PH stainless steel using the PTA-AM a trial and error approach was adopted to explore various parameters. The PTA-AM system has over eight different process parameters, each with a range of values that can be explored. The parameters that were selected for the initial experiment are listed in *Table 4-1*. Due to the large number of process parameters, and their interrelated factors, it was challenging to test all factors in a rigorous manner. Powders Supplier A were used for the initial trials.

Initial experiments were conducted using only the PTA-AM system's gantry (carriage, oscillator and ALC) (Figure 3-1). Single beads of 7-8 cm in length were deposited subsequently on top of each other, with up to 20 layers to a height of 5-10 cm. *Table 4-1* shows some of the selected parameters from the deposition and the outcome of each combination of parameters. The selection of the parameters was chosen to identify the possible range of feasible process parameters. Small walls were formed, but the beads were not always continuous, and the balling effect commonly occurred. The substrates low wettability and non-optimal choice of process parameters caused poor adhesion between the deposit and the substrate's surface [36]. When the balling effect was more pronounced in the first layer, the following layers often eventually filled in the gaps between the formed balls; however, the parts were inconsistent in shape and size due to the formed pillars.

The resultant microstructure of the samples was evaluated. The unetched sample is shown in (Figure 4-1 (a)). Kalling's reagent (2.5g $CuCl_2$ + 33ml $H_2o$ + 33ml HCl + 33ml ethanol) revealed the expected martensitic matrix of 17-4PH stainless steel (Figure 4-1 (b)). A high degree of porosity was noted in the sample microstructure.

To explore distributing the plasma heat over longer distances, the exploration phase was extended to building long stringer beads (Figure 4-2). This used the gantry's carriage but not oscillator, along with the selected process parameters in Table 4-2. The objective was to give the part more time to cool down with the larger surface area. However, the heat input seemed too high and the parts were quickly slumping with additional layers.

*Table 4-1 Parameters and values of the initial printed samples from the PTA-AM system using 17-4PH stainless steel.*

| Parameter | Value | | | |
|---|---|---|---|---|
| Sample number | 1 | 2 | 3 | 4 |
| Sample image |  |  |  |  |
| Powder feed rate (g/min) | 125 | 100 | 100 | 100 |
| Width (mm) | 70 | 70 | 80 | 80 |
| Oscillator speed (mm/min) | 889 | 889 | 889 | 1016 |
| Current (A) | 80 | | | |
| Voltage (V) | 19 | | | |
| Center gas (lpm) | 2.5 | | | |
| Dwell time (s) | 0 | | | |

(a)



(b)

*Figure 4-1 Microstructure of 17-4PH deposited under conditions noted (sample 3 in Table 4-1) (a) unetched and (b) etched using Kalling's reagent.*

*Figure 4-2 Image of the first printed stringer beads.*

*Table 4-2 The values of selected process parameters for stringer beads in Figure 4-2.*

|  | Sample 1 | Sample 2 | Sample 3 |
|---|---|---|---|
| **Current (A)** | 150 | 80 | 80 |
| **Volts (V)** | 23.5 | 23.5 | 23.5 |
| **Carriage Speed (mm/min)** | 3.4 | 3.4 | 2.1 |
| **Powder feed rate (g/min)** | 70 | 50 | 50 |
| **Length (mm)** | 100 | 100 | 100 |

Long weave deposits were proposed as structures with larger surface areas that would allow for more cooling time before the next layer is deposited and to minimize the accumulation of heat. To overcome the initial balling effect that occurred between the substrate and the first layer of deposited melted powders, a high heat input was used by increasing voltage to 23 V and current to 150 A. However, proceeding with the high heat input throughout the build would cause slumping. In order to ensure proper adhesion between the first layers of the build piece and the substrate while avoiding slumping due to high heat, current during the deposition process was initially 130 A and decreased with each layer number to 110 A and held at that value for the

remainder of the build. Figure 4-3 shows the long weave build using 17-4PH stainless steel on the PTA-AM system using the process parameters shown in Table 4-3



(a)



(b)

*Figure 4-3 (a) Top view image of 10-step weave overlay and (b) side view image.*

*Table 4-3 The process parameters of the 10-step weave overlay.*

| Parameter | Value |
|---|---|
| Current | 130 A then 110 A (after step four) |
| Voltage | 26 V |
| Powder feed rate | 50 g/min |
| Length | 165 mm |
| Width | 25 mm |
| Height | 19 mm |

However, as the sample in *Figure 4-3* cooled, the sample began to detach from the substrate on one side due to high internal residual stresses and improper complete adhesion. A large amount of porosity was observed in the cross section of the part, as viewed in *Figure 4-4*, similar to what was noted in Figure 4-1 (a). Another defect that was observed in the cross-section of the weave overlay was the presence of clear segregation between each deposited layer (Figure 4-4). This layer was suspected to be an oxide layer, to be discussed in later sections.
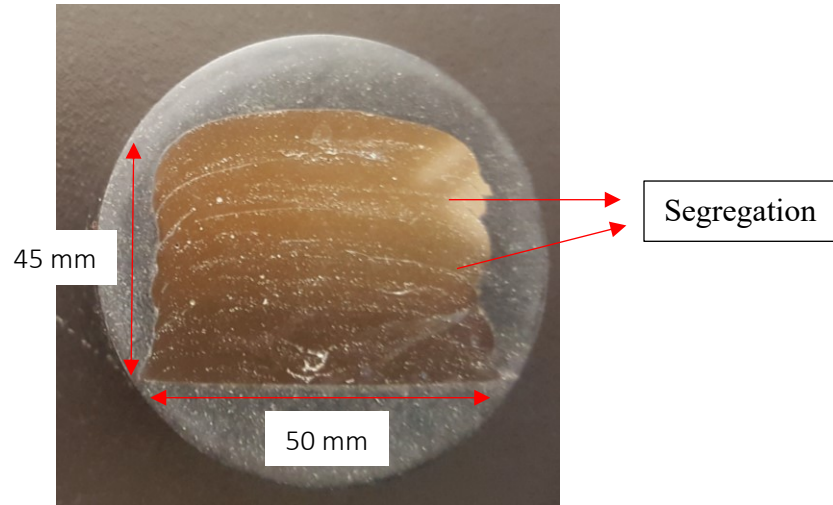


*Figure 4-4 A cross-section of the weave overlay in Figure 4-3 showing segregation between the interlayers of the part.*

The steps taken to understand and mitigate the porosity, lack of adhesion and segregation that arose during the printing process of the weave overlay will be discussed in the following section.

## 4.2  Effect of Shielding Gas

An EDX point scan was conducted on SEM images collected from a cross-sectional surface of the weave deposit. It was found that the oxygen content in the sample was higher than the nominal chemistry provided by Supplier A in a 17-4PH stainless steel (Figure 4-5), possibly entering the molten pool from the atmosphere and creating porosity. Research in literature was conducted on methods to reduce porosity during additive manufacturing, and the use of nitrogen as a shielding gas instead of argon was recommended for 17-4PH with laser AM ([11], [12]). The use of nitrogen as a shielding gas had proven to reduce porosity during laser welding by stabilizing the keyhole;

however, no literature was present on using nitrogen gas with 17-4PH stainless steel and the PTA-AM system.
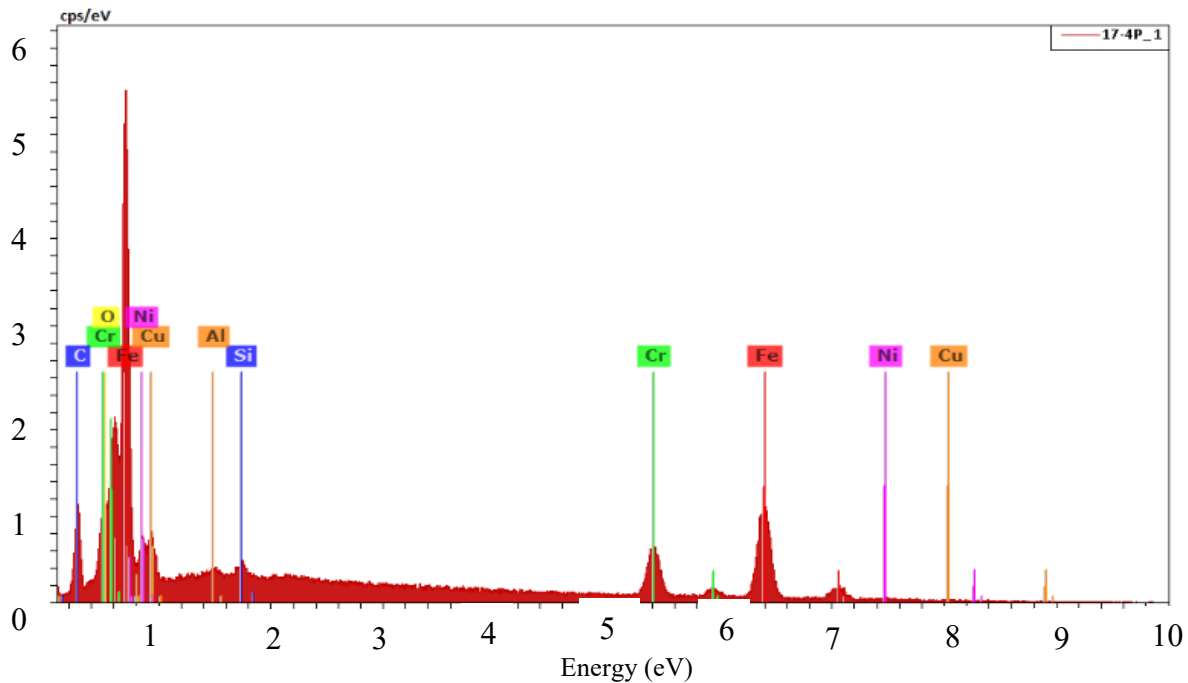


| Analysis | Method | Units | 01 |
|----------|--------|-------|-----|
| Oxygen | Combustion | % wt | 0.035 |

*Figure 4-5 EDX results showing oxygen content in a cross-section of the weave overlay.*

Nitrogen was explored as a shielding gas for depositing 17-4PH on the PTA-AM system. However, the deposition process was not stable as a lot of spatter from the powder was getting stuck to the powder ports and the end surface of the torch. Additionally, more porosity was present in the final sample, which could be observed both internally and externally, as compared to samples printed using argon in all three gas ports. Figure 4-6 is a weave deposited with parameters identical to those used in Table 4-3, with the exception of the nitrogen as the shielding gas. It was soon discovered that nitrogen was being supplied to the powder gas and not the shield gas, as was intended. This meant that all the builds using nitrogen gas had argon gas be supplied as shield gas and center gas, while nitrogen was being supplied to the powder gas. It was later understood that the PTA-AM system cannot supply a separate gas to the shield gas, it can only do that with the powder gas.

*Figure 4-6 Image of the 10-step weave overlay using nitrogen gas.*

Further analysis on samples deposited using nitrogen as a powder gas hypothesized that the supply of nitrogen as a powder gas may have caused nitrogen absorption into the molten pool, increasing the amount of porosity in the build [60]. Additionally, it was found that with poor gas shielding, a melted weld pool is more prone to the absorption of nitrogen and oxygen from the surrounding atmosphere [61], [62]. The use of nitrogen was discontinued; later experiments were conducted with 100% argon gas for all three gas ports. More images of nitrogen samples are given in Appendix B.

It was decided that further experimentation was to be conducted on the original 10-step weave deposit shown in Figure 4-3 to resolve the existing issues of delamination. Preheating the substrate before the deposition process may enhance the adhesion between the melted powders and the substrate's surface and increase wettability [63], [64]. Temperature measurements were taken directly after the deposition of another build piece to record the highest temperature of the substrate; which was measured to be 208°C. The 10-step weave deposit shown in Figure 4-3 was duplicated on preheated substrates at a temperature of 200°C; however, the deposit still detached from the substrate. Other trials were made with samples using other process parameters, and the preheating of the substrate did not seem to influence the wettability of the surface in the case of printing 17-4PH stainless steel using the PTA-AM system. Preheating substrates was discontinued and complete adhesion to the substrate was sought by further increasing initial heat input to ensure wettability with surface and then reduced to prevent excess heating and slumping.

Initial parameters that were used to build the small samples in *Table 4-1* were used as a starting point to develop the appropriate parameters used to build a complete 10-step weave as shown in

*Figure 4-3*. Issues of porosity and oxide layer found in the 10-step weave are discussed and mitigated in the next chapter.

## 4.3  Summary

This chapter summarizes the initial trials that were conducted to identify the working parameters of the PTA-AM system while printing 17-4PH stainless steel. Process defects (excess heat) and material defects (porosity and oxide layers) were identified that arose during the printing process. An initial range of process parameters to print overlayers was identified, and the usage of nitrogen as a shielding gas was eliminated due to increased porosity in the final part.

The next two chapters of the thesis are written for publication as paper-based chapters. Chapter 5 covers the initial defects (porosity and oxide layer formation) found in the printing of 17-4PH stainless steel printed using the PTA-AM system and the remedial procedures taken to alleviate them. The chapter has been peer reviewed and successfully published as a journal article in the International Journal of Advanced Manufacturing Technology. The second chapter, Chapter 6, goes through a more systemic approach to identifying the suitable process parameters that print basic AM shapes with mechanical properties higher or comparable to those manufactured with conventional techniques. The chapter is a manuscript in preparation and is to be sent for publication.

# 5 Plasma Transferred Arc Additive Manufacturing of 17-4PH: Assessment of Defects[1]

Sandy El Moghazi[1], Tonya Wolfe[2], Douglas G. Ivey[1], Hani Henein[1]

[1]University of Alberta, Edmonton, Alberta, [2]Innotech Alberta, Edmonton, Alberta

# Abstract

Plasma transferred arc additive manufacturing is a growing technology in the additive manufacturing world. The Plasma transferred arc additive manufacturing system's ability to produce large samples, compared with other common additive manufacturing techniques, makes it highly desirable in many industrial applications. The selected material in this additive process is 17-4 precipitation hardened stainless steel, which is widely used in numerous fields, such as the aerospace, chemical and mining industries. However, two types of voids were found in the deposits and these voids are detrimental to the mechanical properties. The identified voids were oxide layers and porosity. The presence of oxide layers was correlated to the interaction of atmospheric oxygen with the chromium present in the stainless steel. A shielding hood was designed to provide continuous shielding with inert gas to prevent oxide layer formation. The other source of voids was attributed to the porosity in the initial powders and to the choice of welding process parameters. Changing the powder supplier and optimizing the process parameters, mainly by increasing the heat input to ensure complete melting of the powders, greatly reduced the amount of porosity in the finished part. Hardness measurements were obtained from multiple samples. Hardness was only affected by the ageing process, during which copper precipitates formed within the 17-4 precipitation hardened stainless steel matrix. X-ray diffraction and transmission electron microscopy analyses were conducted to characterize the martensitic matrix before and after the heat treatment and to view copper precipitation after the heat treatment. It is demonstrated that an operating solution to avoid oxide formation is the use of 5% hydrogen in the shield, center and powder gas feeds.

Keywords: Plasma Transferred Arc; Additive Manufacturing; 17-4PH Stainless Steel; Voids; Oxide Layer; Porosity; Hardness

## 5.1 Introduction

Additive manufacturing is a rapidly growing manufacturing technology, where the production of complex 3D shapes is attained by a process of layer-by-layer deposition [65], [66]. The freedom of design, ability to manufacture complex shapes and the variety of materials that can be used

make AM a very desirable manufacturing technique in numerous industries [65]. The parts are produced to a near-net shape once the process is completed.

### 5.1.1 Material Printed: 17-4PH Stainless Steel

17-4PH stainless steel, a martensitic stainless steel, has attracted significant attention in many industries due to its excellent corrosion resistance, ease of fabrication and relatively high strength [7]–[9]. Its corrosion resistance is mainly attributed to the chromium content, while its high strength is due to the precipitation of fine copper precipitates in its martensitic matrix [46]. The heat treatment cycle of 17-4PH stainless steel leads to its strength, hardness and microstructure (Figure 5-1) [67]. The alloy is initially austenitized at a temperature of 1040°C, where any copper precipitates dissolve in the matrix [46]. The solid solution is then quenched to room temperature, supersaturating the copper in the matrix and giving an average hardness between 250 and 300 Hv [42], [46], [68]. To increase strength and hardness of the 17-4PH stainless steel, an aging heat treatment is needed to precipitate the copper. Depending on the desired mechanical properties of the alloy, the temperature and time of the heat treatment are varied. A heat treatment at 480°C for 1 h delivers the highest hardness values, due to optimal aging of the copper precipitates [6]. This optimum heat treatment results in a tensile strength of approximately 1300 MPa, elongation of 9% and hardness of 450 Hv. [40], [46], [54]. Increasing the temperature to a range between 500 and 600°C for 1 h produces a notable reduction in the hardness of the 17-4PH stainless steel, with an increase in ductility. This is attributed to overaging of the copper precipitates, which considerably coarsen at higher heating temperatures, and further tempering of the martensitic matrix [46] [42].

The main microstructural changes that occur during the heat treatment are the precipitation of copper and the transformation of the matrix from lath martensite to tempered martensite [40], [46]. The hardness values before and after the optimum aging process were compared and verified the effect of the copper precipitates on increasing the hardness, as will be discussed below. Changes in the cooling rates affect the resultant microstructure and precipitation of copper. The cooling rates reported in AM can be much faster than those in casting, resulting in microstructures that are very different than those achieved through traditional processing [69]. Therefore, controlling the process parameters in AM is important as this determines the final microstructure and mechanical properties of the alloy.
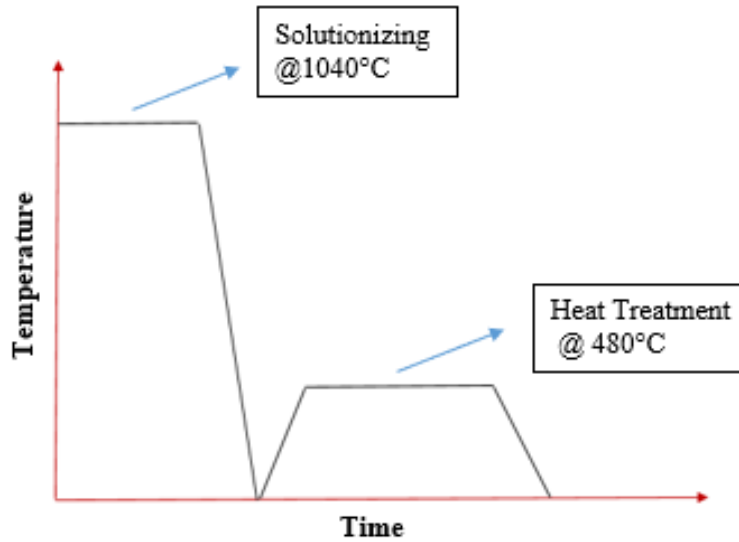
*Figure 5-1 Heat treatment curve of 17-4PH stainless steel.*

### 5.1.2 AM and PTA-AM

Typically, metal AM parts are manufactured using laser or electron beam welding. Recently, however, there has been an interest in adapting arc welding processes to AM due to their high productivity as compared with laser processes. Among the arc welding processes, plasma transferred arc is of particular interest. Its lower heat input and good productivity make it an excellent candidate for AM [14]. Plasma transferred arc welding (PTAW) is widely used for overlay welding to enhance the wear resistance of surfaces used in highly corrosive environments. This is achieved by the deposition of a protective abrasion/corrosion resistant layer on the surface of the part [70]. Compared with other overlaying techniques, such as thermal spraying, PTAW offers higher deposition rates, thicker overlays, good deposition efficiency and relatively lower dilution of the base material [71]. For the aforementioned reasons, a plasma transferred arc additive manufacturing (PTA-AM) machine has been developed to additively manufacture whole parts for industries like the energy sector, in particular oil sands mining. By doing so, many costly hours of unplanned operational shutdown waiting for part replacements can be eliminated and more complex parts can be manufactured that will yield operational improvements. When compared with laser and electron beam AM, PTA-AM is highly desirable as a cost effective solution for larger industrial applications. Fabricating AM parts using PTA-AM allows for faster production of larger parts when compared with laser and electron beam AM. Additionally, because PTA-AM

has multiple powder hoppers, it is not limited to producing parts with just a single material; composite materials and gradations between two or more materials can be achieved [14], [66].

Powder bed fusion (PBF) AM processes, including laser and electron beam, have successfully built parts using 17-4PH stainless steel. The studies behind these experiments sought a general understanding of the influence of the separate processing parameters on the properties of the final 17-4PH stainless steel part. Issues of interest include density, hardness and defects [67]. The general findings from those processes indicated that defects such as porosity and lack of fusion (LOF) defects were common, especially in processes like powder bed fusion [16] [56]. Samples printed using the PTA-AM system had the same types of general defects, as will be discussed in this paper. Porosity is also a common finding when casting 17-4PH stainless steel and, likewise, can be attributed to the processing parameters during casting. Both shrinkage porosity and gas porosity can be eliminated by optimizing process parameters such as the casting temperature, design of cast and solidification time [72]. It can thus be concluded that defects found in the AM parts while printing 17-4PH stainless steel using the PTA-AM system were common findings in other AM processes and not specific to the PTA-AM process.

*Figure 3-1* shows a photograph of the PTA-AM system at InnoTech Alberta. The powders are delivered in an inert gas medium from the hopper to the torch. Inert gas (argon) is required for the center, powder and shield gases during the welding process. A high current ionizes the inert gas that is fed into the torch system and transforms it into a plasma. The plasma generates very high temperatures that melt the feed alloy powder which then deposit on a substrate [66].The properties of the final product are highly dependent on the alloy used and the selected process parameters during deposition [14], [65], [73]. Furthermore, the effect of different thermal histories on the deposited AM part allows for more anisotropy in the parallel and perpendicular directions during deposition. As such, the controllable process parameters and the quality and properties of the material play crucial roles in the microstructure and thus the mechanical properties of the final product.

### 5.1.3   AM Process Defects

AM processing is a highly competitive and attractive field. Like any growing field of interest, AM parts have associated process defects that need mitigation. In AM, some of the defects appear as voids. The first type of defect observed in fabricated samples of 17-4PH stainless steel is associated with the formation of oxide layers between the interlayers of AM [74]. The formation of oxide layers is not common to all AM processes; it is more specific to direct energy deposition (DED) processes due to the lack of a continuous inert gas environment over the whole AM surface as it is being fabricated. The type of stainless steel used in any application is dependent on the corrosion resistance that is required and, hence, determines the necessary chromium content in the stainless steel. To achieve the desired corrosion resistance, a thin chromium oxide layer forms on the surface of the steel sample to isolate the stainless steel from corrosion and environmental degradation [75]. Hence, most stainless steels are very reactive during processing and must be shielded from the atmosphere when using an AM-DED process. In addition to voids formed due to oxide layers, porosity has been detected as the second type of defect. Pore formation in AM parts has been reported for different processes.  For example, hatch speed and hatch spacing were found to directly affect the amount of porosity present in direct metal laser sintered (DMLS) parts) [76].

A study conducted found that porosity originated from two sources: gas porosity or LOF porosity [10]. The first type is induced by the absorption of atmospheric gases such as nitrogen, oxygen or hydrogen in the liquid pool [3]. The second type forms as voids around non-fully melted powders during the solidification process [10]. Both types of porosity can be detrimental to the longevity of the produced AM part, since porosity has been identified as a major cause of crack propagation in AM samples [16]. Additionally, porosity present in the initial powders is another detrimental cause of porosity in the final part, as will be discussed later.

Solidification shrinkage, alongside porosity, is another detrimental feature in AM parts. During the deposition of melted droplets over the previous solidifying layer, or the cooler substrate, anisotropic shrinkage occurs between the layers of the AM part. The dissimilar thermal gradients between the deposited layers lead to substantial overall thermal stresses, which can result in premature failure [15]. The present paper will, however, only focus on the former of the mentioned AM issues; namely, void formation due to oxide layers and porosity due to initial powders and LOF.

While research has been conducted on each of the above issues, no previous research has been found addressing the fabrication of 17-4PH stainless steel using PTA-AM. The focus of this paper is to explore different experimental methodologies to alleviate the issues of oxide layer and pore formation in the AM part of 17-4PH stainless steel using PTA-AM.

## 5.2   Experimental Procedures

### 5.2.1   Description of the PTA-AM System

An image of the PTA-AM system used in this study is shown in Figure 3-1. It  is integrated with a 3-axis motion linear drive table, which allows for the production of more complex AM designs [14]. The integrated system is able to control most of the parameters in this process, such as movement direction, shielding gas, powder gas and center gas flow rates, powder feed rate, current, voltage and coordinated travel speed. The commercial PTA system used is a Kennametal Starweld 400 PTA Welding system, with a Kennametal Stellite Excalibur Torch. An image of the torch is presented in Figure 5-2 where the nozzle of the center gas, powder gas and shielding gas are presented alongside the non-consumable tungsten electrode. It is important to note that the torch provides a shielding atmosphere around the powder being deposited; however, it is localized to the area directly beneath the torch. The PTA-AM geometry is created by defining a set of parameters, from the aforementioned controllable parameters, by inputting them into the machine's control panel. The control panel is the interface between the user and the PTA-AM system. It allows for the selection and control of all the process parameters during the printing process.
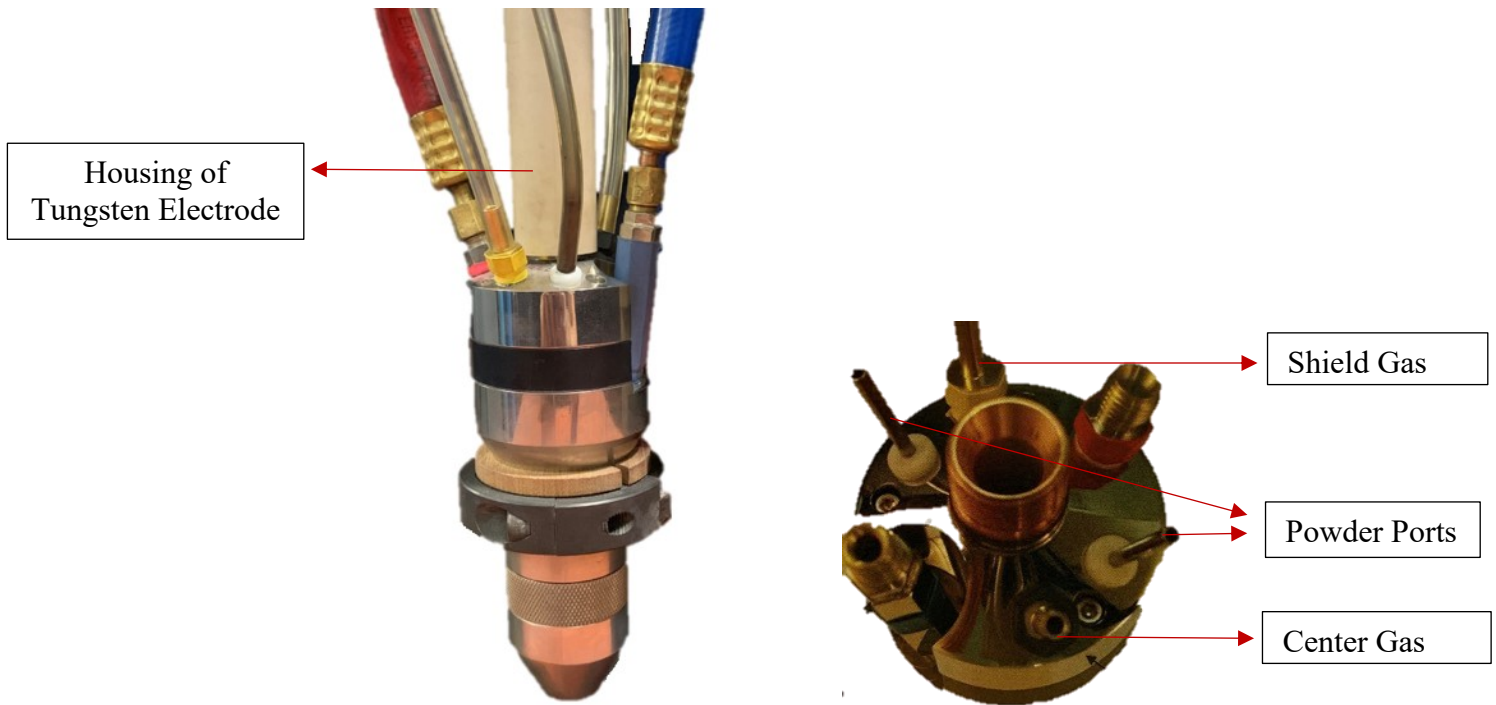
*Figure 5-2 Front view (left) and top view (right) of Kennametal Stellite Excalibur Torch.*

## 5.2.2 Shield Hood Design

To generate a protective, inert atmosphere over the entire AM part while it was being fabricated, a shielding hood was designed, constructed and installed around the torch (Figure 5-3). This ensured that the deposited parts were continuously shielded with a continuous flow of an inert gas. The process parameters are given in Table 5-1. Aluminum wool was added inside of the shielding hood to act as a gas distributor. A visualization experiment using a glycerine mist was conducted to ensure that the inert gas flow coming from the shielding hood covered the complete deposit.
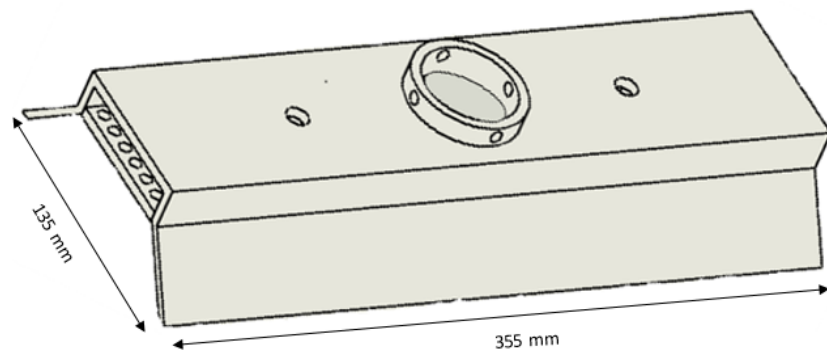


*Figure 5-3 Design of the shielding hood.*

*Table 5-1 Test parameters for the PTA-AM system using 17-4PH stainless steel.*

| Parameter | Range of Parameters |
|---|---|
| Feed rate | 0.42-0.58 g/s (25-35 g/min) |
| Travel speed | 1.3-1.7 mm/s (3-4 in/min) |
| Current | 50-120 A |
| Voltage | 25-28 V |
| Shield hood gas flow rate | 240 kPa (35 Psi) |
| Center gas | (0.002 $cm^3$/min) 2 lpm |
| Powder gas | (0.001 $cm^3$/min) 1 lpm |
| Shielding gas | (0.01 $cm^3$/min) 10 lpm |
| **Part Dimensions** | |
| Length of sample | 152.4 mm (6 in) |
| Number of layers | 10 |

### 5.2.3 Powder Parameters Used for Printing

The 17-4PH stainless steel powders were obtained from two different suppliers; both were argon gas atomized. For Supplier A, the powder was sieved to a size of 53-125 µm, which is ideal for the PTA-AM system, and results in continuous powder flow from the nozzle. The powder size distribution of Supplier B was 45-105 µm. The chemical composition of both powders is given in Table 5-2. Before the powders were placed in the PTA-AM powder hopper, they were well mixed by manually shaking the powder bottle before it is emptied into the powder hopper.

*Table 5-2 Chemical composition of 17-4PH stainless steel powders, wt%.*

| Element | Supplier A | Supplier B |
|---|---|---|
| C | 0.01 | 0.07 max |
| Mn | 0.2 | 1 |
| Si | 0.3 | 1 |
| Cr | 16.4 | 15.0-17.5 |
| Ni | 4.1 | 3.0-5.0 |
| Mo | 0.01 | - |
| Cu | 4.3 | 3.0-5.0 |
| S | n.d. | 0.03 |
| P | 0.007 | 0.04 |
| Nb+Ta | 0.3 | 0.15-0.45 |
| O | 0.04 | 0.06 |
| N | 0.03 | 0.02 |
| Fe | Bal. | Bal. |

### 5.2.4   Operating Parameters for Printing

The 17-4PH stainless steel powders were melted and deposited onto a carbon steel substrate. A range of parameters, given in Table 5-1, was used to achieve a complete build deposit. The deposit was produced using an oscillation width of 25 mm with an oscillation speed of 15 mm/s. A multi-layered deposit, the sample, was produced for the evaluation of printing.

### 5.2.5   Characterization of Samples

Each of the 150 mm (6 in) fabricated parts was cut into 2.5 mm (1 in) sections, using a silicon carbide blade. The sectioned samples were hot mounted with a thermosetting phenolic powder for hardness testing and optical imaging. The mounted samples were ground and polished with an EcoMet 250 Buehler grinder/polisher. The samples were first ground using 240, 400, 600, 800 and 1200 grit silicon carbide abrasive papers and then polished using 9, 6, 3, and 1 μm polycrystalline diamond suspension, followed by 0.05 μm alumina suspension. After grinding and polishing, optical and scanning electron microscope (SEM) images were used for microstructural analyses. An Olympus BX-UCB microscope was used for optical imaging and a Zeiss Sigma 300 VP-FESEM was used for SEM imaging. The hardness values of the samples were measured with a Wilson VH3100 hardness machine. A 5x5 hardness matrix was taken over the cross-section of the samples, with indentations 5 mm apart in width and 2 mm apart in height. Vickers hardness values

were measured along the width of the sample and across the different layers, using a 1 kg load and a 5 s indentation time.

A tensile test of the unshielded sample was carried out following the ASTM E8 standard. Copper precipitates were imaged and analyzed using transmission/scanning electron microscopy (TEM/STEM) and energy dispersive x-ray (EDX) spectroscopy in a JEOL JEM-ARM 200CF TEM, operated at 200 kV. Extraction replicas were prepared using the following procedure. The sample surface was immersed in Kalling's reagent (copper chloride, ethanol, water and hydrochloric acid) for five minutes to preferentially etch the matrix, so that the precipitates protruded from the surface. A thin layer of carbon was evaporated onto the surface of the etched sample. Squares, ~2 mm x 2 mm in size were scribed in the deposited carbon. The sample was then placed back into the etchant, allowing some of the scribed squares to release from the steel sample and float to the surface. Individual squares were then captured with 3mm diameter Cu TEM grids. Extracted precipitates, embedded in the carbon film, were ready for imaging in the TEM.

X-ray diffraction (XRD) was used to characterize the microstructure before and after aging. A Rigaku Ultima IV XRD system was utilized with a Cu x-ray source, operated at 40 kV and 44 mA.

### 5.2.6    Aging Process

The 17-4PH stainless steel requires an aging heat treatment to precipitate the supersaturated copper; this increases the strength of the material. Depending on the desired strength, hardness and microstructure of the part, the heat treatment of 17-4PH stainless steel can be varied according to Figure 5-1. Based on the results obtained from as welded samples, samples with the lowest porosity and amount of oxide layers were heat treated at the optimum heat treatment at a temperature of 480°C for 1 h [46].

### 5.2.7    Pore Size and Distribution

Fiji Image J, Version 1.8.0_172, was used to quantify the porosity in the fabricated parts. All voids in the matrix were marked with a different color than the background in order to determine the void fraction.  AM samples were sectioned, mounted, ground and polished and then imaged in the SEM. Each SEM image was analysed and the porosity percentage was determined. This was done

on images from multiple locations across each AM sample to ensure an accurate estimation of the porosity.

## 5.3 Results and Discussion

### 5.3.1 Oxide Layer and Porosity

This work addresses methodologies to reduce or remove oxide layers and voids. Microscopic images identified two types of voids: voids due of the formation of the oxide layers and porosity voids (Figure 5-4 and Figure 5-5). The first type of voids was present in the interlayers of the samples. The segregated interlayers were analyzed using energy dispersive x-ray (EDX) spectroscopy. The interlayers had high levels of both chromium and oxygen (Figure 5-6), which was likely due to the formation of protective $Cr_2O_3$ at the interlayers of the build pieces [74], [75]. The oxide layer forms over the 17-4PH deposit, and likely has traces of the stainless steel, as shown in the EDX spectrum (Figure 5-6). Similarly, the lack of copper can be explained by its absence in the specific region where the EDX analysis was done. Although $Cr_2O_3$ is generally considered to be beneficial from a corrosion perspective, its formation in the interlayers of the AM part acts as a barrier to the continuous formation and development of the internal microstructure, ultimately leading to anisotropic mechanical properties in the fabricated part. Associated with this oxide layer were segregated sections in each of the interlayers, due to poor adhesion that occurs between the oxide layer and the next layer of deposited melted powders. This segregation further intensifies the poor adhesion of the AM part [75]. Analysis of the fracture surface of a tensile sample, produced from one of the sample deposits, indicates that the fractures were initiated along the oxide layers (Figure 5-7). This illustrates how the oxide layer reduces the mechanical properties through poor interlayer adhesion. The presence of voids, both in the form of oxide layers between the interlayers and spherical porosity, makes the part heterogeneous and is detrimental to the functionality of the final AM part [55], [67].

The other type of voids observed was in the overlays (Figure 5-4) that formed due to spherical gas entrapment pores and LOF during the welding process [77]. Porosity is typical of AM parts manufactured by different processes and research has been ongoing in an attempt to mitigate them [56]. One such mitigation technique is the use of hot isostatic pressing (HIPing) as a post-welding

heat treatment. However, HIPing is a costly and time consuming method [78]. Identifying the different sources of voids in the AM deposits would aid in their mitigation.

The average volume percent of voids present in multiple fabricated parts was determined, for the same operating conditions, to be 18±2% (Table 5-1). This high percentage of voids is detrimental in applications with any loading, and as such the parts are required to be fully dense [10]. In order to enhance the densification of PTA-AM parts and to fabricate near net shape products, the two types of voids must be eliminated.
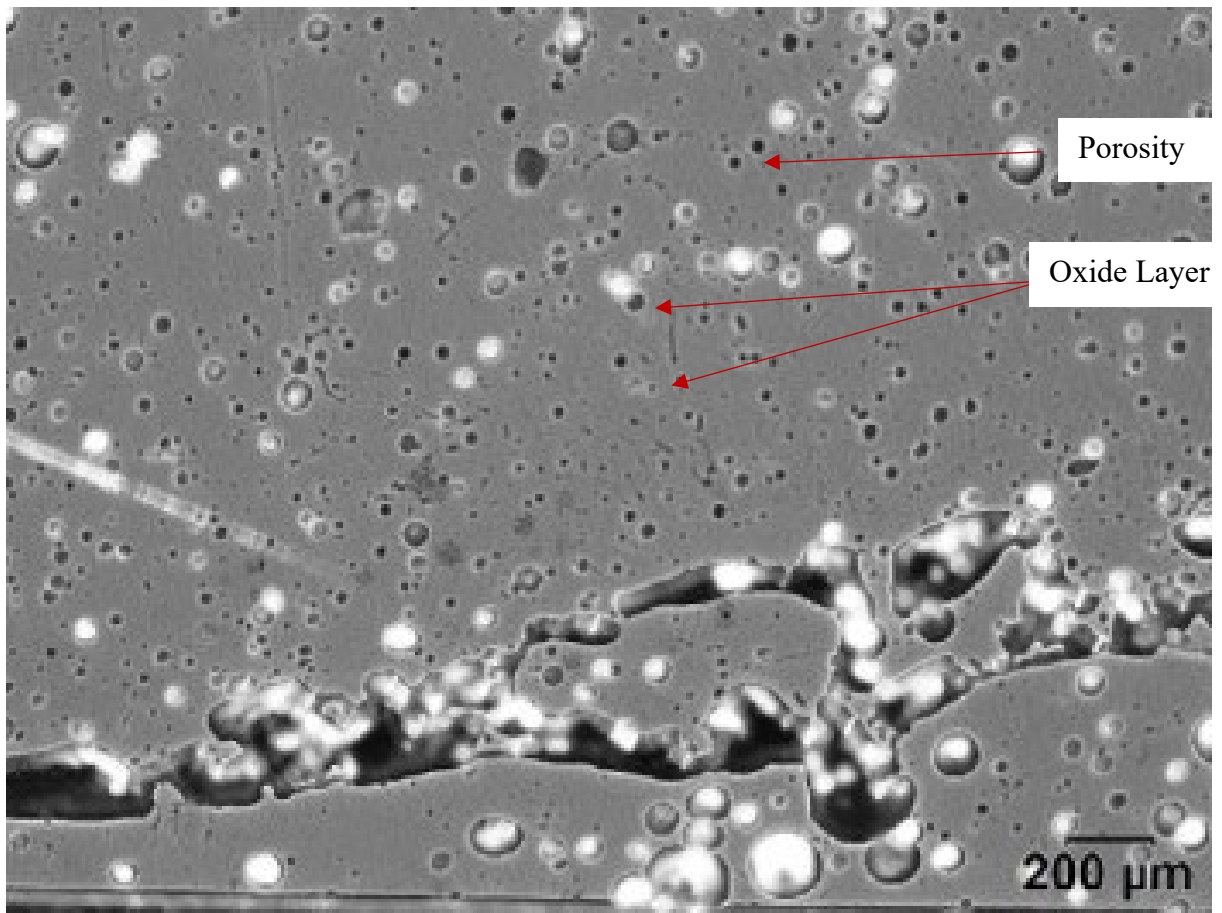


*Figure 5-4 Optical image showing the oxide layer and porosity.*
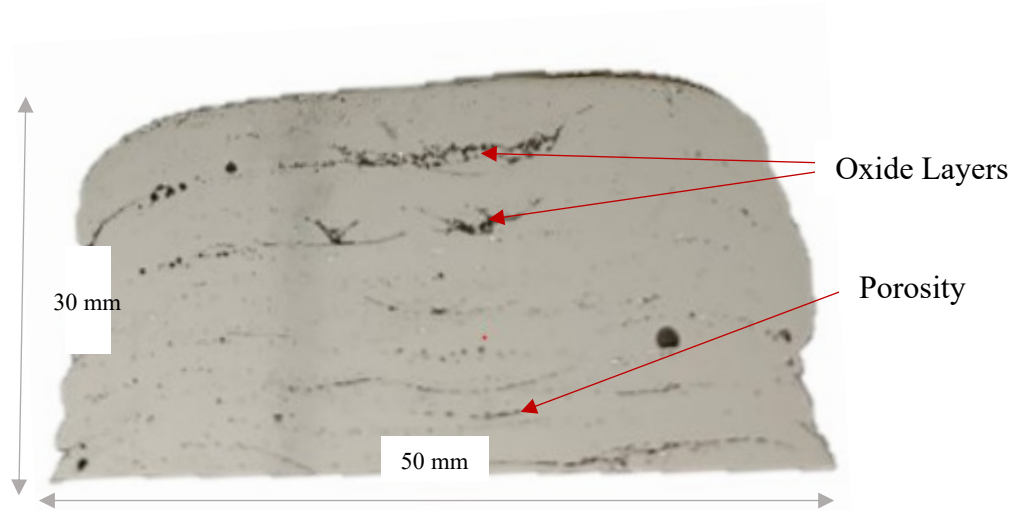
*Figure 5-5 Cross section of deposit showing oxide layers (black transverse lines) and porosity.*

### 5.3.2   Shielding Hood

The high level of chromium content in stainless steel is required to enhance the room temperature corrosion resistance of the material. Chromium in the stainless steel reacts with atmospheric oxygen to form an oxide layer on the surface of the stainless steel [74], [75]. Even though this process provides the stainless steel with good corrosion resistance, its formation at the interlayers of an AM part has an adverse effect on layer adhesion. Very fast cooling rates in this process mean that the AM part is solidified as the torch is moving; as mentioned earlier, the torch has its own local shielding atmosphere. The $Cr_2O_3$ layer, however, forms if there is no inert shielding atmosphere over the part at temperatures above 947 K. Thus when the torch changes positions and the temperature of the part is at a higher temperature, an oxide layer will form (Figure 5-5 and Figure 5-6) [74], [75]. In order to prevent the formation of these oxide layers, a shielding hood was designed to ensure the continuous flow of a shielding, inert atmosphere over the AM deposit during processing, preventing the reaction of chromium with oxygen (Figure 5-3). Samples were fabricated using the same process parameters as in Table 5-1, with the addition of the shielding hood. The pressure of the shielding hood gas (inert gas pressure) was varied. For the optimum shielding gas pressure (Table 5-1) the volume percent of voids decreased to 10±2% (Figure 5-8). This reduction in voids was correlated to the elimination of oxide interlayers, as shown in Figure

5-9. Removal of the oxide layers leads to better adhesion and increased densification of the deposit as a whole.
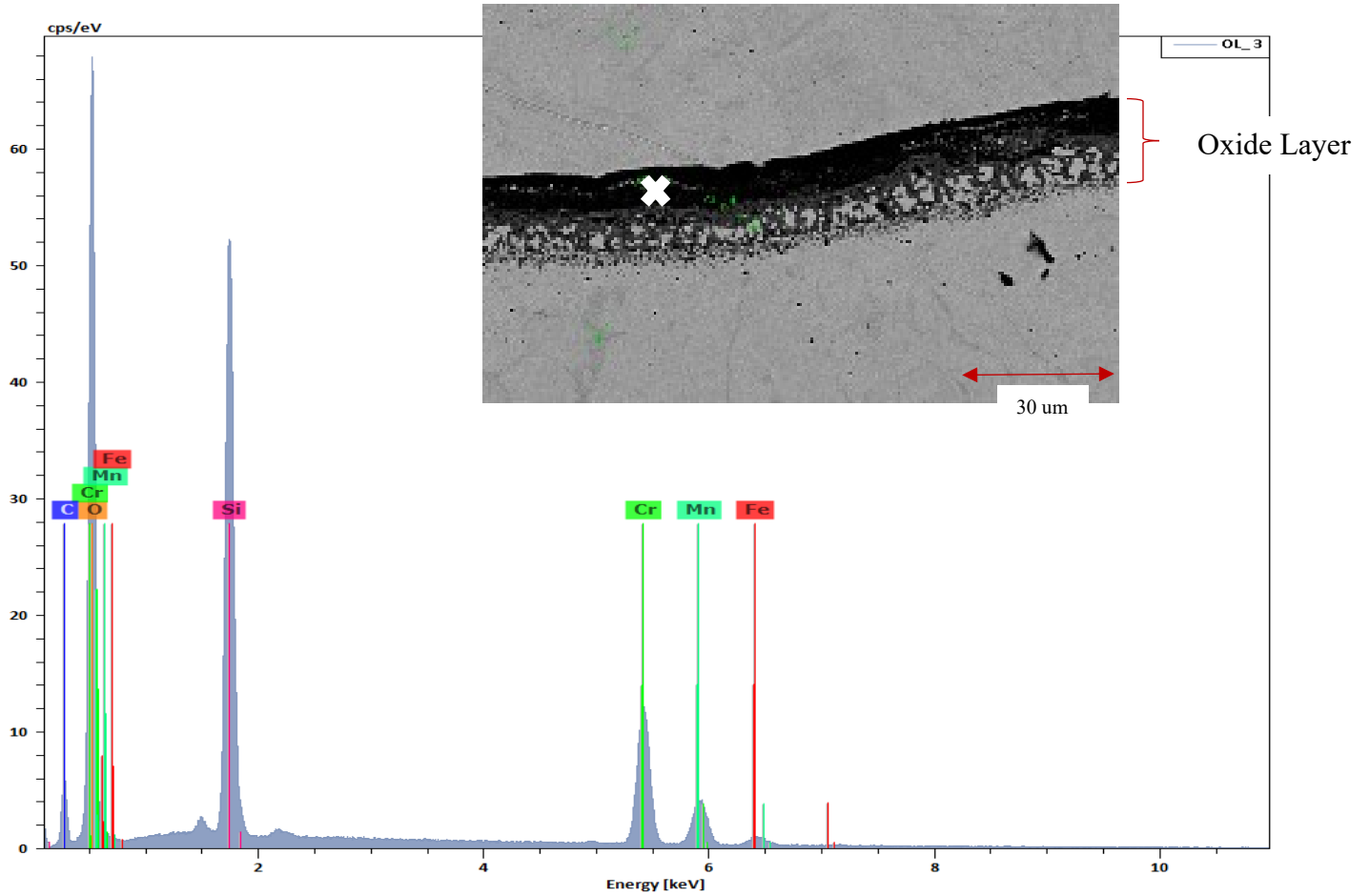


*Figure 5-6 EDX spectrum from the region indicated with an 'X' in the inset image; this region is the oxide layer between two deposited layers.*

*Figure 5-7 Surface of tensile sample showing initiation of cracks along the oxide layers and the brittle fracture of the sample.*



*Figure 5-8 Comparison of void percentage (and oxide layer elimination) without (top) and with (bottom) the shielding hood. Both blue and green represent the voids (porosity and oxide layer) present in the part.*
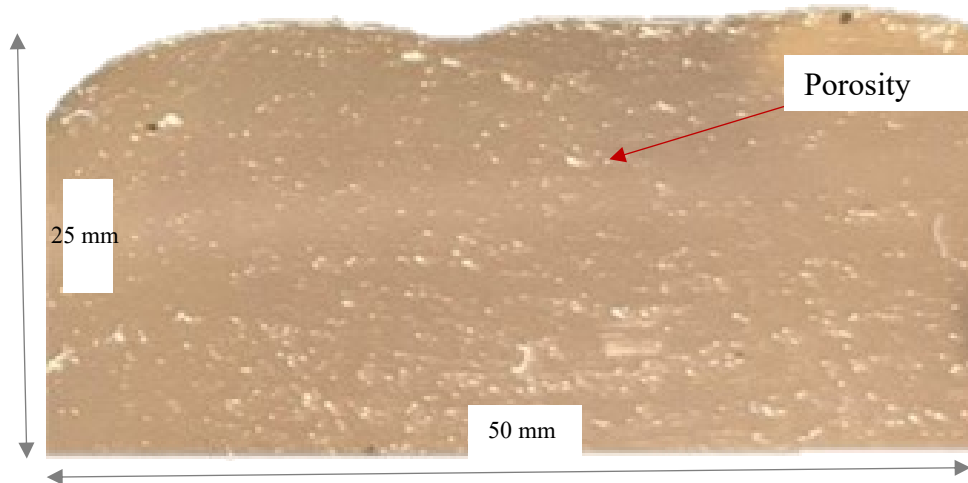
*Figure 5-9 Cross section of deposit showing porosity, but elimination of oxide layers.*

### 5.3.3 Process Parameters

The combination of process, material and operational parameters that yield a dense, near net part is a challenging quest [10], [79]. In the PTA-AM system, for example, plasma gas or shielding gas flow rate (Table 5-1) can be used to control the temperature of the weld pool; hence, controlling the cooling rate and the residual stresses generated. Other PTA-AM process parameters, such as the current, voltage or travel speed, can impact the formation of voids inside the deposit and the temperature of the weld pool as well. By reducing the heat input (current and voltage), the part is made more susceptible to the formation of LOF porosity. Similarly, very high travel speeds may not provide sufficient time for complete melting of the powder. Efforts to print a sample required the raising of the heat input, by increasing current or decreasing travel speed, to ensure complete melting of all the powders and the inhibition of the associated internal porosity and, thus, print a part with minimum porosity [10]. For the above reasons, the heat input was increased by almost 15% using the process parameters as shown in Table 3. Higher heat inputs, with and without the shielding hood, resulted in a lower volume percent of internal voids compared with lower heat inputs. With an almost 15% higher heat input, through a combination of increased current and voltage and without the shielding hood, the volume percent of voids dropped from 18% to 8%. Similarly, using the increased heat input and the shielding hood dropped the porosity from 10% to 2%, due to elimination of the oxide layers and LOF porosity. A void volume percent of 2% is still unacceptable in the finished component. Therefore, the source of these voids was investigated.

Table 5-3 *Optimized parameters for the PTA-AM system using 17-4PH stainless steel.*

| Parameter | Range of Parameters |
|---|---|
| Feed rate | (27-30 g/min) |
| Travel speed | 1.3-1.7 mm/s (3-4 in/min) |
| Current | 110-120 A |
| Voltage | 25-27 V |
| Shield hood gas flow rate | 240 kPa (35 Psi) |
| Center gas | (0.002 cm$^3$/min) 2 lpm |
| Powder gas | (0.001 cm$^3$/min) 1 lpm |
| Shielding gas | (0.01 cm$^3$/min) 10 lpm |
| **Part Dimensions** | |
| Length of sample | 152.4 mm (6 in) |
| Number of layers | 10 |

### 5.3.4 Powder Characterization

After eliminating the oxide layer and a large number of voids through parameters' optimization and enhanced shielding, the deposits contained approximately 2 volume percent porosity. A study found that if the initial powders are porous, then there is a greater possibility that porosity will be transferred to the final fabricated part [10]. The presence of porosity in the powders obtained from the first supplier was analyzed. Image analysis of polished samples of the as received powder indicated that there was almost 9 volume percent porosity present within the powder particles. To determine the effect of internal porosity of powder on the final deposit, new powders (Powder B)

were obtained from a different supplier, which had an initial powder porosity of only 0.3 volume percent. Figure 5-10 shows images of the porosity in both powders.

The deposit formed from the initial powder (Powder A), using the shielding hood and the optimized process parameters (Table 5-3), had a total void content of 2 volume percent. However, using the new powder (Powder B), the deposit, with identical process parameters and the shielding hood, had an overall void percentage of only 0.4 volume percent. Figure 5-11 shows sample deposits using Powder A and Powder B, with corresponding images in Figure 5-12. The influence of powder quality on the homogeneity of the deposit is clearly apparent. Figure 5-13 shows a cross-section of a sample from the part fabricated with Powder B (Figure 5-11), using the shielding hood.

### 5.3.5   Hardness

Hardness tests were conducted on all the different samples produced from the different stages of the above experiments. A set of four samples (Table 5-4) was taken to represent the four main categories of experimentation, and the results are shown in Figure 5-14. A 5x5 hardness matrix was conducted on each of the samples, and the average results tabulated. All samples were fabricated with the same optimized welding parameters (Table 5-3); the differences were in the type of powder used and the addition/removal of the shielding hood. It should be noted that there is no obvious effect, within error, of the process variables on the sample hardness (Figure 5-14). The range of the hardness values for the four samples falls within the range given in the literature for unaged samples, 250-300 Hv [42], [46], [68]. The error bars represent standard deviation from each set of 25 readings taken per sample.

In order to enhance the hardness of the samples, an aging heat treatment was conducted at the optimal aging temperature and time, which was reported to be 480°C for 1 h. Sample D, the sample with the lowest porosity and no oxide layers, was selected from Table 5-4 to undergo the heat treatment. The build layer does not have an effect on the hardness value. The optimal hardness was achieved following the prescribed quench and temper heat treatment and the results are compared in Figure 5-15. Clearly, there is a significant increase in hardness following heat treatment.
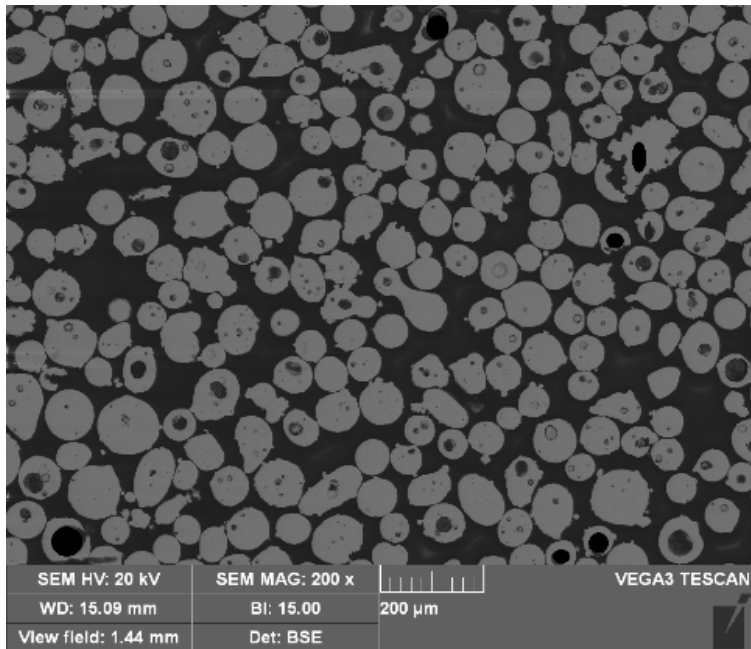
(a)
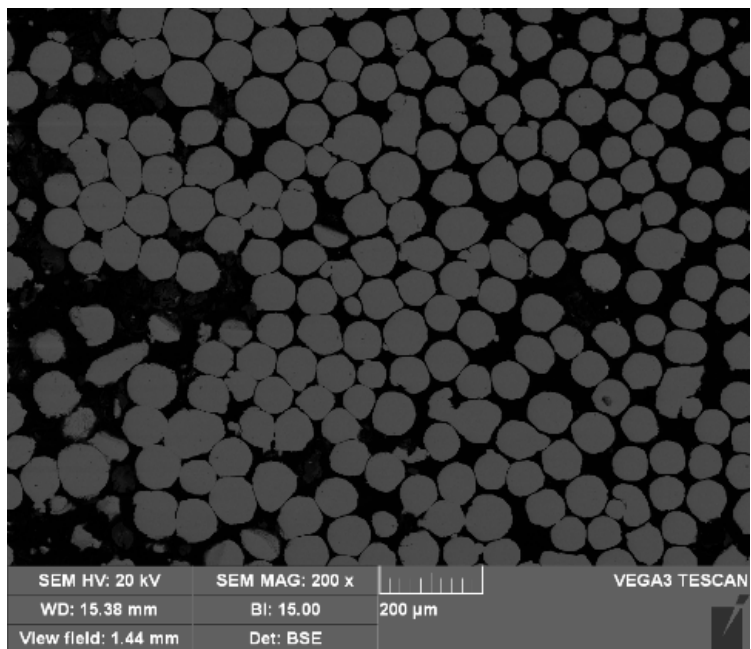


(b)

*Figure 5-10 SEM backscattered electron (BSE) images of porosity in powder A (a) and powder B (b).*

*Figure 5-11 View of the surface of samples fabricated with powder A (left) and powder B (right) using identical process parameters.*

### 5.3.6 Matrix and Precipitates

In order to understand the effect of the heat treatment on the microstructure of the welded samples, XRD and TEM analysis were conducted. From the literature, the expected matrix of the sample before heat treatment is lath martensite that transforms into tempered martensite after heat treatment [46]. However, because 17-4PH stainless steel has a low carbon content, the differences between lath martensite and tempered martensite (composed of ferrite and very low amounts of cementite) are not discernible using optical microscopy (Figure 5-16) [80]. XRD was done before and after heat treatment to validate the literature and to differentiate between lath martensite (martensite peaks) and tempered martensite (ferrite peaks). The XRD analysis from samples done in this experiment are in Figure 5-17; both samples shows peaks which are identified as ferrite peaks, even though the peaks from the first sample were expected to be martensite. This result is due to the low carbon content (0.07 wt.% max.) of 17-4PH stainless steel, which leads to a c/a ratio close to one for the body-centered tetragonal structure of the martensite [49][45][50][51]. The c/a ratio is one for a perfect cube, like the body-centered cube structure that forms ferrite. A deviation from one in the c/a ratio results in a body-centered tetragonal structure, similar to that found in

martensite. Additionally, the content of the carbon is further reduced within the matrix because carbon combines with other elements in the stainless steel to form precipitates (Figure 5-18). Moreover, the almost identical overlap of the XRD peaks before and after the heat treatment, even though copper precipitated, is related to the relative size of the copper atoms to the iron atoms. Copper is present as substitutional atoms in the iron lattice before heat treatment, because the two atoms are similar in size. When the copper precipitates out of the iron lattice, there is little distortion of the iron lattice, so that any shift of the XRD peaks (change in the two theta angle) in the XRD pattern is essentially undetectable. Copper peaks were undetected in XRD after heat treatment.

TEM analysis was done on extraction replicas to verify that copper precipitated during aging. STEM bright field (BF) and annular dark field (ADF) images, as well corresponding x-ray maps, of an aged sample are shown in Figure 5-18. Larger NbC particles are visible, along with small localized copper regions. The copper particles are ~10 nm or smaller in size and can account for the increase in hardness during aging. The XRD results showed no change in the matrix and, according to the literature, the precipitation of the copper is the main factor accounting for the increase in the hardness values during heat treatment.

*Table 5-4 Legend for sample parameters.*

| Sample ID | Powder Type | Shielding | Porosity/Oxide Layer |
|---|---|---|---|
| A | A | No | Both |
| B | A | Yes | Porosity |
| C | B | No | Oxide |
| D | B | Yes | Neither |
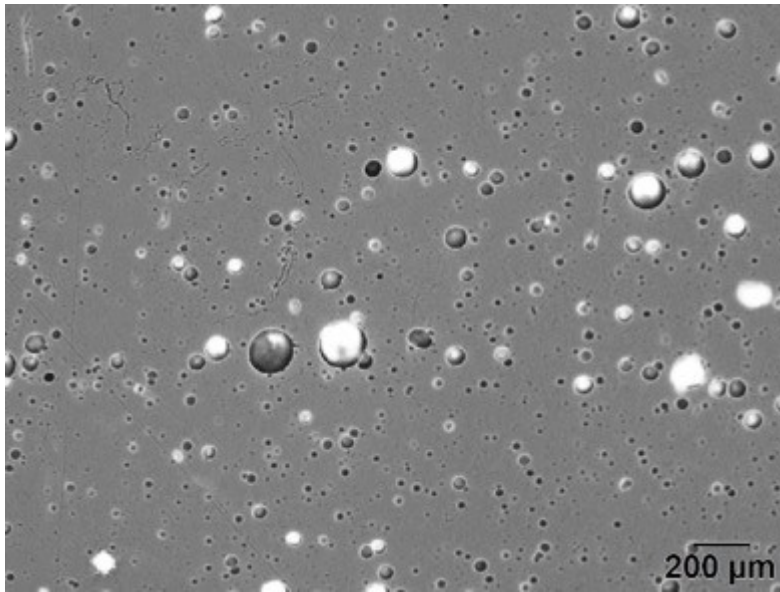
(a)
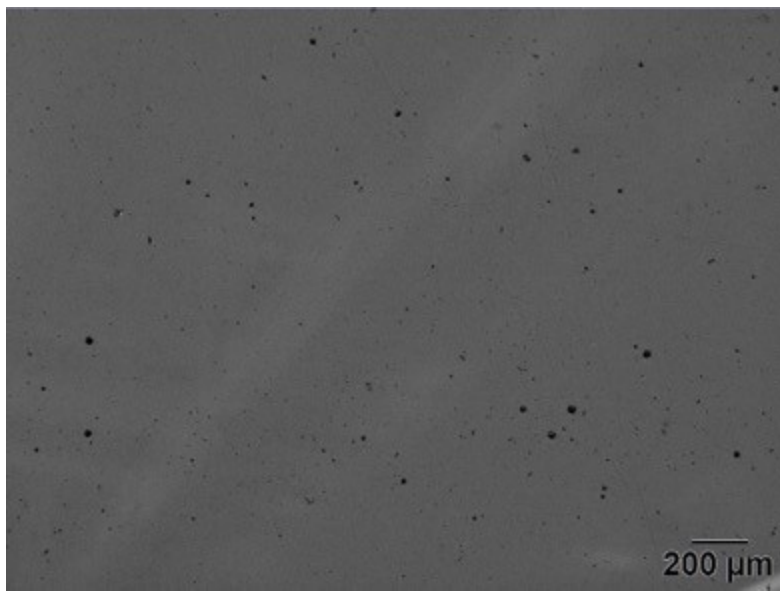


(b)

*Figure 5-12 Optical microscopy images of parts fabricated with powder A (a) and powder B (b) with identical process parameters.*

*Figure 5-13 Cross section of deposit using powder B showing elimination of both the oxide layers and porosity.*
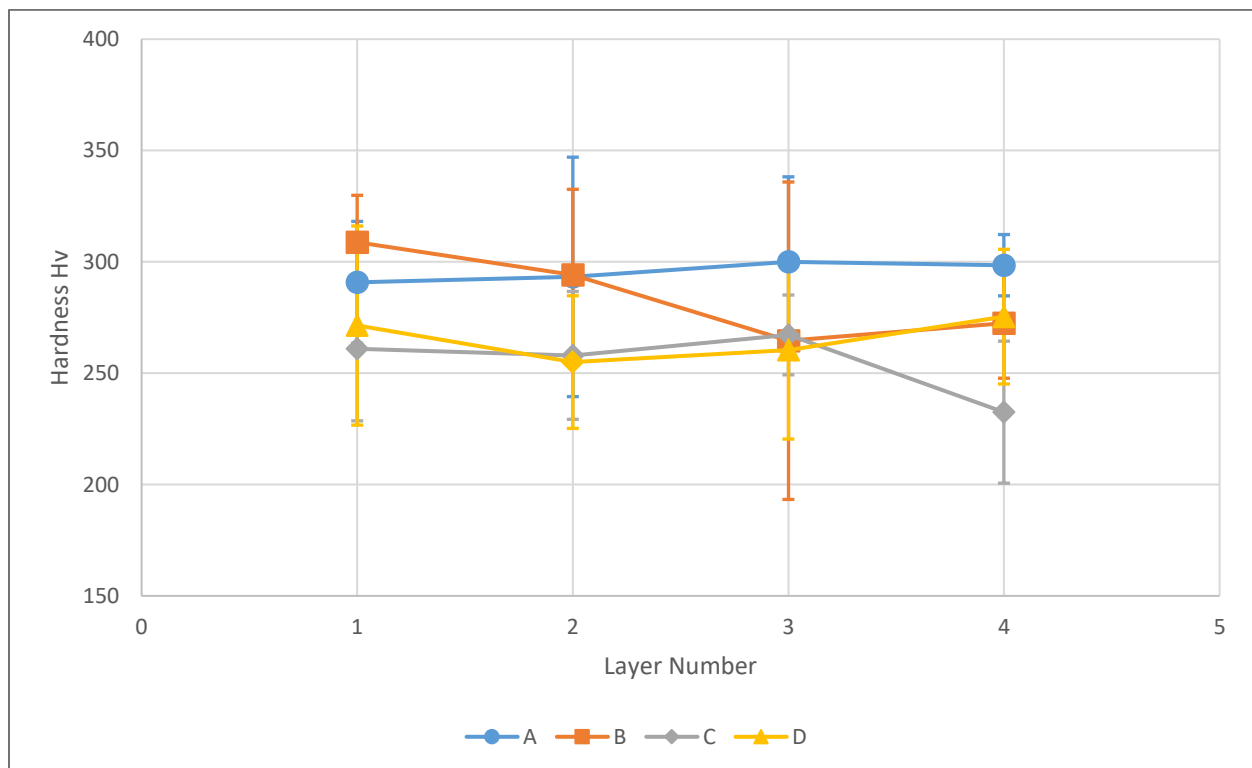


*Figure 5-14 Hardness vs. layer number for samples fabricated with different processing parameters (Table 5-4).*
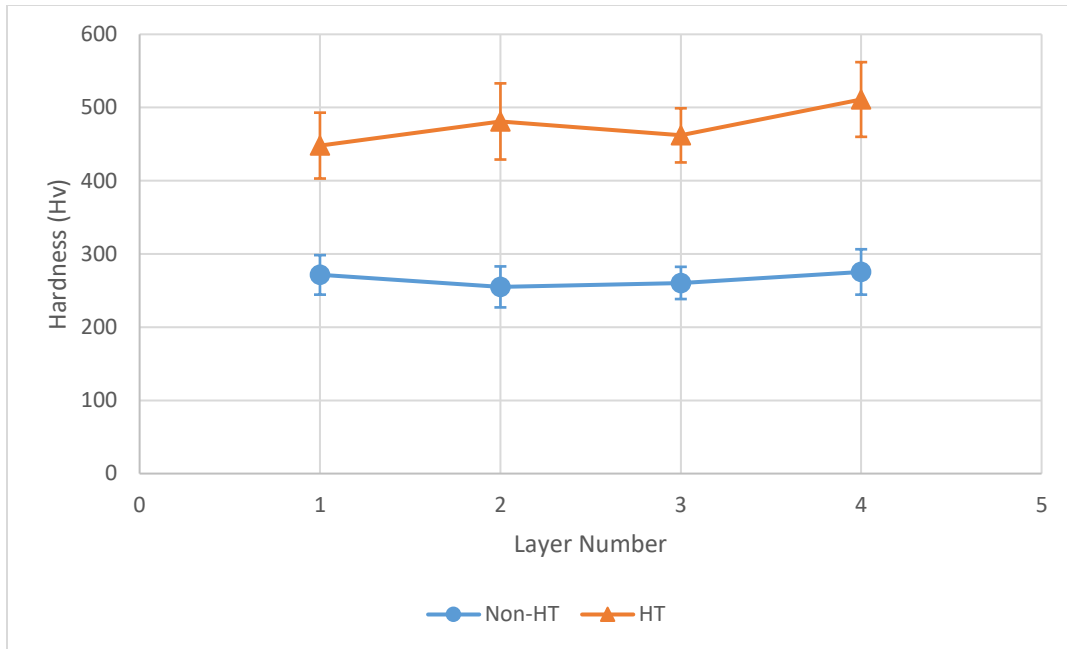
*Figure 5-15 Hardness vs. layer number for non-heat treated (Non-HT) and heat treated (HT) samples after aging at 480°C for 1 h.*

Additionally, because the hydrogen in the 5% $H_2$+95% Ar gas mix requires higher energy to ionize, as compared to the argon, there is a higher heat input during the welding process [81]. Hydrogen requires higher energy to ionize because the energy is needed to go into dissociating the hydrogen molecule into two hydrogen atoms. Cross sections from parts built with the 5% $H_2$+95% Ar gas mix were compared to samples built with pure argon, without using the shielding hood in either part. It can be seen in Figure 5-19 (a) that no oxide layers are present in the final part with the 5% $H_2$+95% Ar gas mix, which was calculated to have around 0.4% voids, as opposed to 7% voids Figure 5-19 (b). Without the oxide layers included, Figure 5-19 (b) has a porosity count of around 0.4%. This verifies that the use of the 5% $H_2$+95% Ar gas mix does not attribute to any addition in porosity and is free of any oxides.
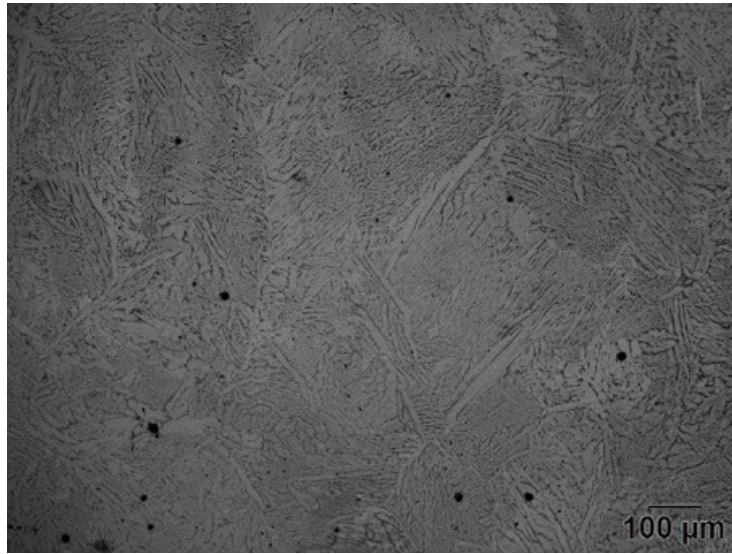
(a)
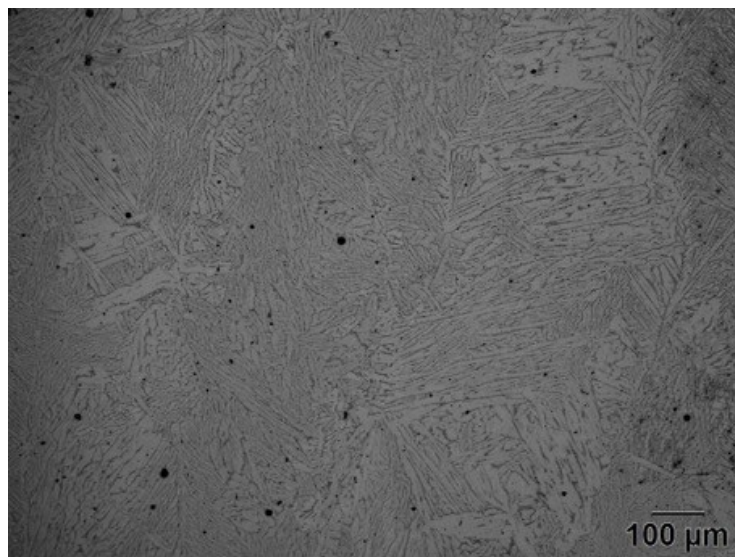


(b)

*Figure 5-16 Optical images for 17-4PH stainless steel before (a) and after (b) aging heat treatment for 1 h at 480°C.*
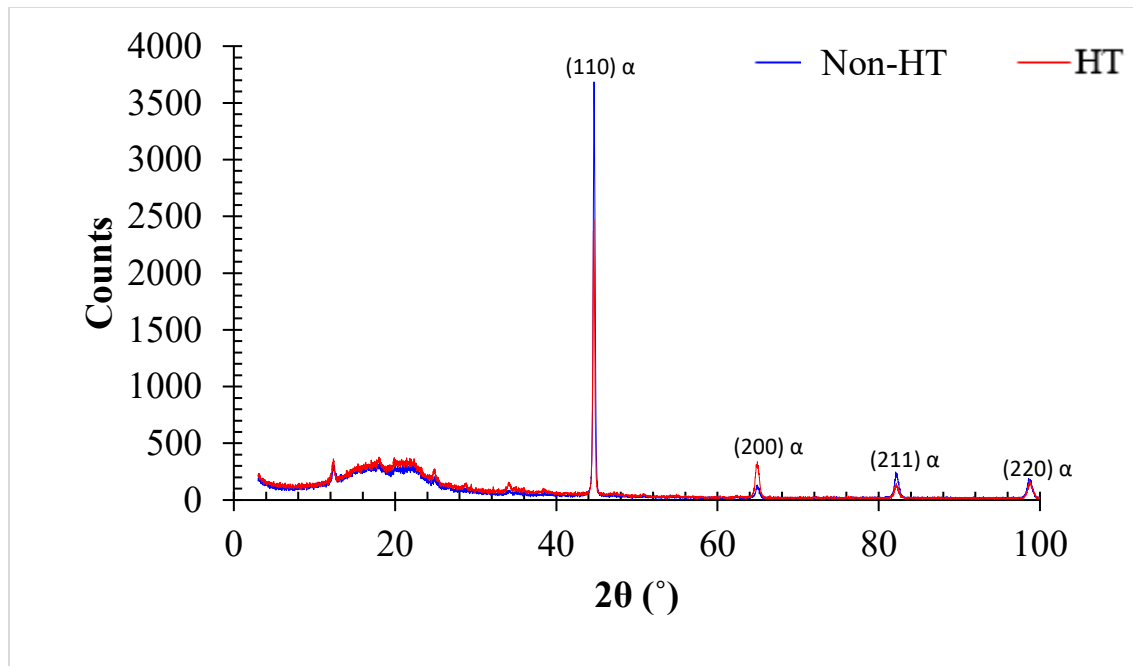
*Figure 5-17 XRD patterns of heat treated (HT) and non-heat treated (Non-HT) samples.*

### 5.3.7    Hydrogen Gas Mix

The shielding hood is an instrument that was designed to verify the mechanism by which the formation of the oxide layer can be completely prevented. After the verification of this mechanism, a mix of 5% $H_2$+95% Ar gas was used, without the shielding hood, instead of the pure argon gas with the shielding hood. The gas mix is used to source all the three gas ports: shielding, center and powder. There are several advantages to using this gas mix: preventing the formation of the oxide layer and providing higher heat inputs during welding [81]–[83]. Because hydrogen is a reducing agent, it reacts with the atmospheric oxygen and hinders the formation of the oxide layer.
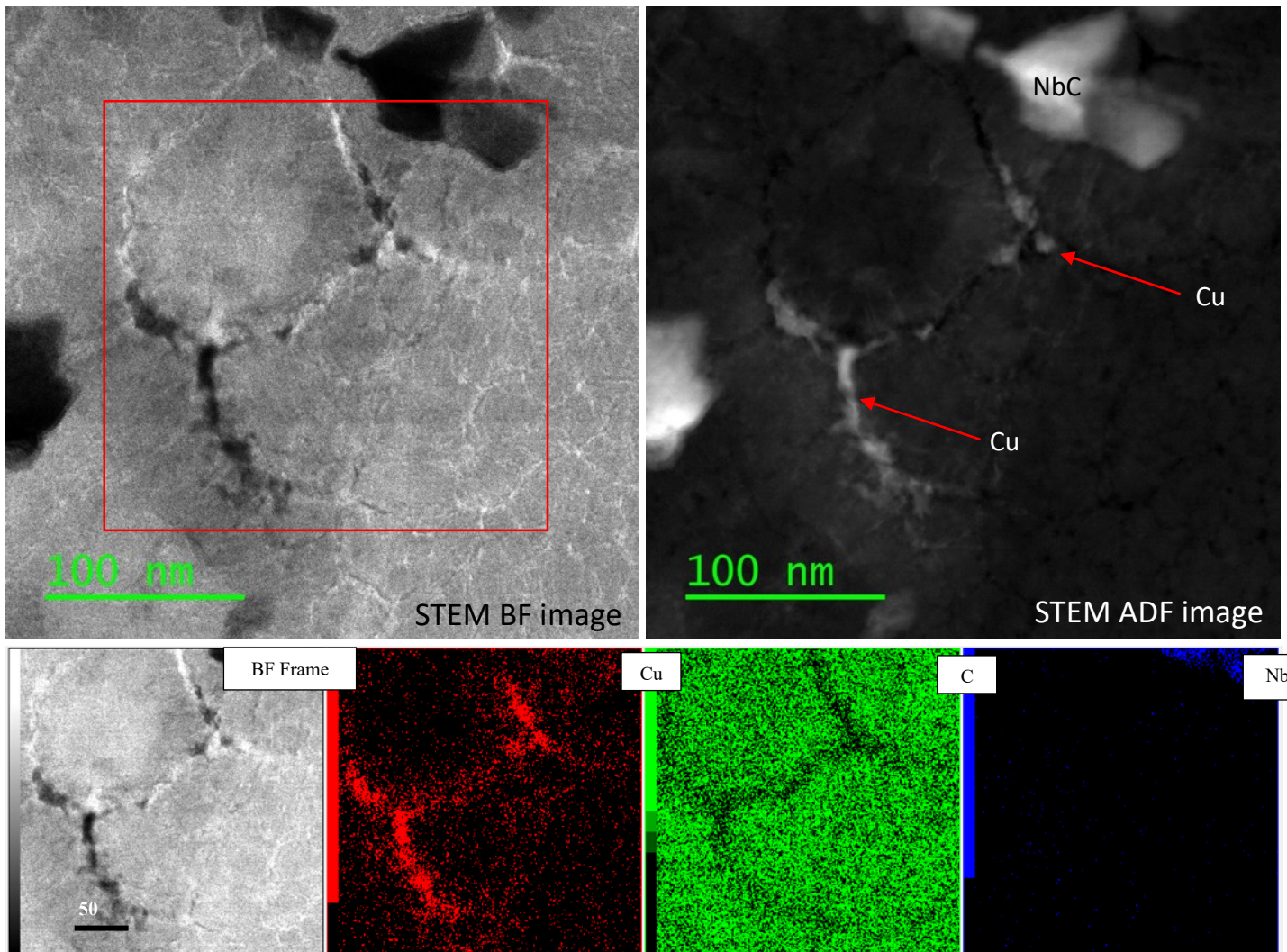
*Figure 5-18 STEM BF image, ADF image and X-ray maps (Cu, C and Nb) of an aged sample; localized regions rich in copper correspond to copper precipitates.*
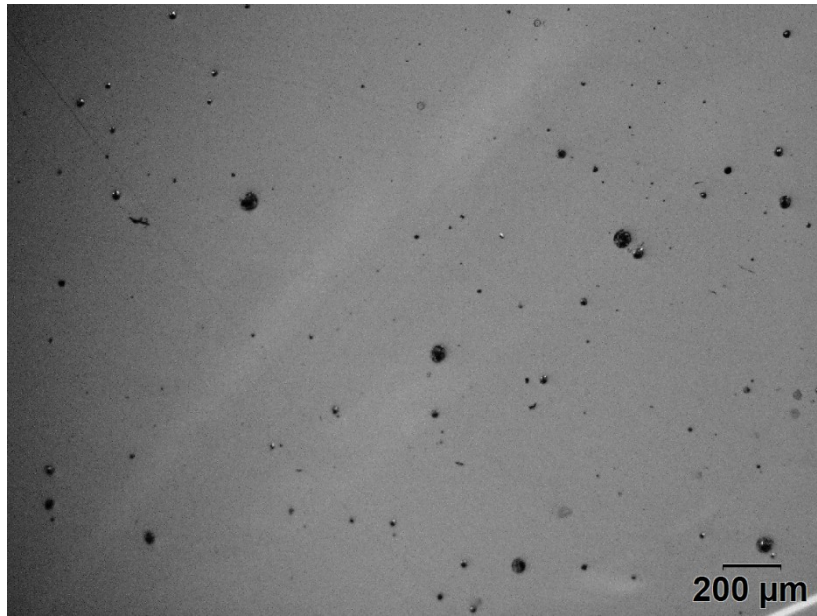
(a)
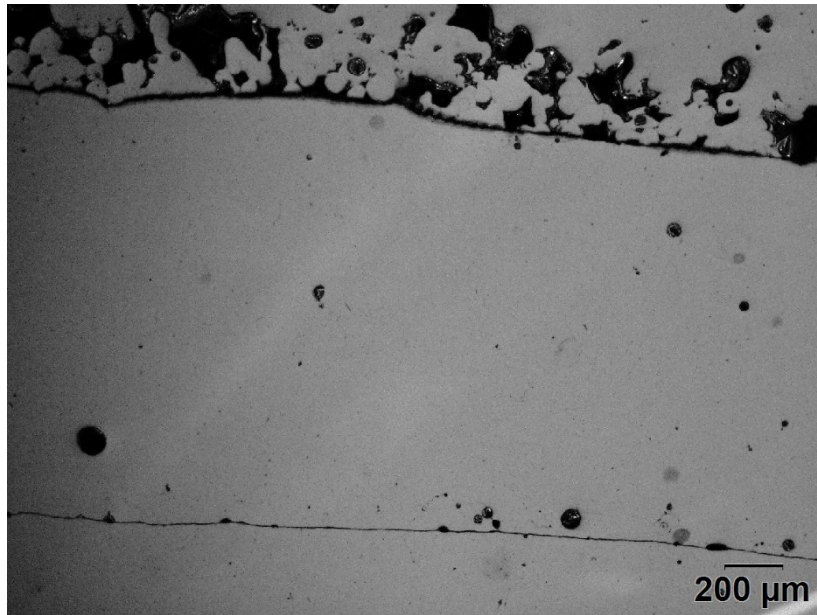


(b)

*Figure 5-19 (a) AM part with 5% H₂+95% Ar gas mix (b) AM part with pure Ar gas.*

## 5.4 Conclusion

Several problems were encountered when processing 17-4PH stainless steel using plasma transferred arc additive manufacturing (PTA-AM). Voids were found both at the interface of the interlayers (oxide layers) and within the bulk of a given layer (porosity). The first of these was attributed to the lack of shielding from the atmosphere, resulting in oxygen combining with the chromium present in the 17-4PH stainless steel to form oxide layers. These oxide layers led to poor adhesion between the different layers of the sample. Bulk porosity formation was sensitive to the initial powder quality and process parameters [32]. These two void defects were mitigated as follows:

- The oxide layer was eliminated by the use of a shielding hood, which ensured a continuous, protective inert atmosphere for each layer during deposition.

- Process parameters were optimized by increasing the heat input by up to 15%, which eliminated the formation of lack of fusion (LOF) porosity.

- Pore formation in the bulk layers was traced back to the quality of the powders utilized. Initial porosity in the powders was detrimental to the density and compactness of the fabricated parts. Powders with lower initial porosity produced parts with significantly lower porosity.

- Aging of the fabricated parts led to an increase in hardness, due to the precipitation of copper nanoparticles.

The hardness of the samples was independent of powder quality, process parameters or layer height. The hardness values coincided with typical values for aged 17-4PH stainless steel. The addition of 5% hydrogen to argon was found to prevent the formation of oxides, thus eliminating the use of the shielding hood.

## 5.5 Acknowledgments

# 6 Selection of Process Parameters on PTA-AM 17-4PH Using the Taguchi Method

## 6.1 Introduction

Additive manufacturing (AM) is a new manufacturing process establishing itself as a pivotal tool in prototyping and complex manufacturing. The AM process involves the processing of a 3D computer model, which on a 3D printing machine is built through a layer-by-layer addition of materials to fabricate a physical component [65], [66]. Typically, a laser or electron beam are used as the heat source to melt the materials in metal based AM. However, recent work explored the use of arc welding processes for AM applications [28]. Plasma arc transferred welding is commonly used for hard facing equipment exposed to severe wear and corrosive environments. Incorporating this welding process as a heat source in metal AM is generating interest as it has a higher deposition rate and ability to handle larger particle sizes as well as metal matrix composites [14]. It uses its plasma arc as the energy source to melt the metal powders, and it can build functionally graded materials using two powder hoppers. In this research, plasma transferred arc additive manufacturing (PTA-AM) will be explored. The apparatus used is shown in *Figure 3-1*.

Stainless steels, are used in industries where corrosion and oxidation resistance are critical [65]. One such popular stainless steel is 17-4 precipitation hardened (PH) stainless steel. It has been frequently used in mining and oil and gas sectors. The properties of the martensitic 17-4PH stainless steel include high corrosion resistance, high tensile strength and good fracture toughness at working temperatures below 300°C [7]–[9]. Depending on the applied heat treatment, the precipitation hardened stainless steel results in a variety of mechanical properties. Traditional processing of 17-4PH stainless steel involves an austenitizing treatment at 1040°C, where the copper particles are dissolved in solid solution [46]. When the 17-4PH stainless steel is quenched from 1040°C to room temperature, the copper becomes supersaturated in the martensitic lath matrix and has an average Vickers hardness of 250-300 Hv [40], [42], [46]. For optimal mechanical properties, the 17-4PH stainless steel is subsequently tempered at a temperature of 480°C for 1 h to precipitate the copper and reach an average hardness of 450 Hv. The martensite matrix is transformed to a tempered martensite during the peak aging heat treatment [46]. Even though the

matrix changes from lath martensite, a harder phase, to tempered martensite, a tougher phase, the hardness of the 17-4PH stainless steel increases due to the precipitation of copper [40], [42], [46]. Raising either time or temperature of the aging heat treatment leads to overaging the copper precipitates and a reduction in hardness [42], [46].

Different AM processes, such as laser based processes [52], [84] and wire arc AM (WAAM) [28], have been used to print 17-4PH stainless steel. From the different AM processes, the initial microstructure of as-deposited 17-4PH stainless steel in AM processes is yet to be agreed upon in literature. Literature using selective laser melting to print 17-4PH stainless, used different chemical compositions for shielding gas. Using a 100% nitrogen atmosphere resulted in up to 75% by volume retained austenite, while using 100% argon atmosphere resulted in only 8% retained austenite [52]. Effects of laser energy density on the microstructure of 17-4PH stainless were also studied. Using a laser energy of 61 J/mm$^3$ resulted in fully columnar grain structures [52], while using a laser energy density of 107 J/mm$^3$ resulted in fine blocks of martensite [84]. Using WAAM with 17-4PH stainless steel, different chemical compositions of shielding gas were explored [28]. The first gas contained 2.5% $CO_2$ gas with argon, while the second gas contained 38% He gas and 2% $CO_2$ gas with argon. The first gas resulted in 0.85% area percentage of retained austenite as opposed to only 0.12% area percentage with the second gas. The authors concluded that the additional heat coming from using helium in the shielding gas resulted in slower cooling rates and the formation of a predominantly martensitic matrix [28]. The combination of varying process parameters from different AM processes apparently yields different as-deposited microstructures. Changing the composition of the protective gas seems to have a direct effect on the induced heat input going into melting the powders and the solidification of the printed part. Variations in energy delivered by the heating source, table speed, powder feed rate, chemical composition of shielding gas are all examples of process parameters that can also alter the final microstructure.

Another factor affecting the microstructure of 17-4PH stainless steel in AM processes is the chemistry of the alloy. The ranges of each element in the standard chemical composition of 17-4PH stainless steel can alter the initial formed phases in the alloy. According to the Schaeffler diagram (Section 6.2.3), changes in the chromium and nickel equivalents can result in different microstructures. Because 17-4PH stainless steel has a range of acceptable compositions in weight % for chromium (15.0-17.5), nickel (3.0-5.0), copper (3.0-5.0) and niobium (0.15-0.45), the actual

chemical composition for 17-4PH stainless steel used in different processes can result in different microstructures, which will be further discussed in a later section. Moreover, with AM processes that use shielding gases other than argon, such as WAAM, the combinations of shielding gas compositions can directly influence heat input [28]. For example, the addition of helium to argon can induce a higher heat input during the deposition process and would result in lower amounts of retained austenite, and more martensite in the as-deposited stage [47], [52]. Thus, higher heat inputs result in more martensite than retained austenite in the final microstructure [28]. Conversely, shielding gases that induce lower heat inputs are likely to form more retained austenite in the as-deposited microstructure. Based on the above findings, the selection of process parameters, like shielding gas composition, is critical on the resultant final microstructure. This is especially noteworthy for a material like 17-4PH stainless steel that can have martensite, austenite, ferrite or a combination of them, depending on process parameters and cooling rates.

Studies investigating microstructure and mechanical properties have been conducted on 17-4PH stainless steel using several AM processes, such as WAAM [28] and laser based processes [48], [85]; however, the PTA-AM system has yet to be explored. The influence of each process parameter of the PTA-AM system on the final mechanical properties of the build has not been fully developed. Like most AM processes, it has microstructural defects that are due to lack of control of the operating parameters in the respective AM process, such as the presence of porosity in the build due to inconsistent shielding. A significant effort is being made to reduce the gas porosity [10], [56] and lack of fusion (LOF) created during many AM processes [10]. Gas porosity is due to the entrapment of atmospheric gases, such as oxygen, nitrogen or hydrogen, within the molten metal pool during the welding process or the manufacturing of the initial powders [61], [62]. The LOF porosity results from insufficient heat input for complete melting of the metal feedstock powders which can act as crack initiators and can result in premature failure of the component; it can also cause disbanding between layers [10]. These two defects can be avoided by selecting the appropriate process parameters as was shown in the previous Chapter [13]. Heat input is calculated based on Equation 6.1.

$$\text{Heat input} = \frac{Voltage X Current}{Table\ speed} \qquad \text{(Equation 6.1)}$$

In addition to porosity, oxide layers are prone to forming between layers during the printing of 17-4PH stainless steel using AM processes in processes that are not enveloped by a shielding atmosphere, giving room for interaction with atmospheric gases, such as the PTA-AM system. When building a layer, due to the nature of the high chromium content in 17-4PH stainless steel, a $Cr_2O_3$ layer may form on the layer surface during the printing process due to interactions with atmospheric gases [74]. The formation of this oxide layer is desirable under typical operating environments, however, in the case of AM processing it is an unwanted addition because it creates anisotropy due to the delamination that occurs between layers.

All the above defects, whether process or material related, are detrimental to the quality of the AM build. The porosity and formation of $Cr_2O_3$ oxide layer were eliminated by using a powder feedstock with lower internal porosity and by increasing the heat input by increasing voltage and current and using a gas mix of $5\%H_2+95\%Ar$, as discussed in Chapter 5 [13]. The addition of hydrogen to the gas feed in PTA-AM has other additional benefits to the process. The center, shielding and powder gases in the PTA-AM system are required to provide a stable arc, create an inert environment around the molten pool, and deliver the powder to the arc region, respectively. The chemical composition of the gas will affect arc properties, like plasma initiation and stability, plasma temperature profile and heat transfer in the system. Adding hydrogen to the argon gas increases the heat input of the arc and creates a reducing atmosphere. The higher heat input can partially be attributed to the energy required to dissociate the diatomic hydrogen bonds into atomic hydrogen. Additionally, the presence of the hydrogen in the gas mix increases the current-carrying capacity of the argon, allowing for higher heat input [81]. Hydrogen gas, being a reducing agent, helps reduce the formation of oxides on the surface of stainless steels and produce a clean surface free of oxides without the need for using a shielding hood [81]–[83]. Moreover, the increased heat input will increase the temperature of the powder, which will allow for better bonding between powders, reducing the LOF porosity [83].

There are eight process parameters in the PTA-AM system that can affect the quality of the build: offset between nozzle and substrate, center gas flow rate, powder gas flow rate, shield gas flow rate, nozzle angle between powder outlet flow relative to printing direction, powder feed rate (PFR), current and table speed. With these numerous parameters that need to be controlled in the PTA-AM system, it is prohibitive to determine the appropriate level of each individual parameter

as well as the interaction between the parameters in order to ensure a defect free build. Therefore, it was advantageous to identify a range of parameters that would yield a successful build 17-4PH stainless steel, using the PTA-AM system. The operating parameters which yielded a successful overlay deposition of 17-4PH stainless steel using the PTA-AM system have been identified and discussed in Chapter 5 [13]. The focus of the next step in this study is to determine the most influential parameters that result in an AM build with good mechanical properties and to compare the resultant properties to those achieved by conventional processes. It is believed that variation of each independent process parameter will influence the final mechanical properties. In addition, the interaction between parameters will also have an influence on the mechanical properties of the printed component. Completing a full factorial experimental design with all the possible operating parameters would be a lengthy and costly study. Taguchi's design of experiments (DOE) methodology was selected to identify the most influential parameters in the process for printing 17-4PH stainless steel parts using the PTA-AM system [86]. The Taguchi DOE provided a statistical analysis to determine the most influential parameters using a minimal number of experiments.

This Chapter will discuss two Taguchi DOEs that were designed to identify the window of parameters for the PTA-AM system using 17-4PH stainless steel. The first DOE will identify key parameters that result in the fabrication of multilayer walls. Build height, wall thickness, maximum deviation of wall thickness, hardness and porosity of each run will be analyzed. A statistical analysis will be conducted to identify the most influential parameters of the printing process. A second DOE will be developed based on the outcome of the first DOE to verify the selection of the more influential process parameters on the PTA-AM system and which will be used to build cylindrical and square tubes. The experimental procedure and analysis of the printed samples are presented.

## 6.2 Experimental Procedure

In this section, the details of the experimental setup, along with the characterization techniques conducted on the final samples, will be described. The experimental setup includes the machine setup, gases used, powder characterization and the design of the experiments methodology. This

is followed by the characterization techniques used on the printed AM coupons and the accompanying analysis of the results.

### 6.2.1 PTA-AM System

The PTA-AM system is shown in *Figure 3-1*. The commercial PTA system is a Kennametal Starweld 400PTA Welding system, with a Kennametal Excalibur torch. Blended metal powders are contained within a powder hopper where they flow through into the torch fluidized by a carrier gas and exit two powder ports in the nozzle to be deposited onto a substrate. Mixing the metal powders prior to pouring into the powder hopper ensures an equal dispersion of the different powder sizes across each batch. The shielding gas provides an inert environment around the molten deposit to prevent the atmospheric gases from entering into the melt pool. The center gas is responsible for creating the plasma arc. The plasma arc is formed when the center gas is ionized due to the high currents delivered to the electrode, establishing a plasma between the torch and the substrate. The control pendant is used to set many of the operating parameters of the PTA system, including the voltage given by the standoff distance between the torch and the substrate. A 3-axis gantry table is integrated with the PTA unit to create the PTA-AM system. The component is processed into G-code, which is the computer language required to control the 3-axis motion of the table (*Figure 3-4*), as well as the arc ignition, current and powder feed rate. The range of axis speeds of the 3D table is given in *Table 3-2*.

### 6.2.2 Gas Mix

The 5%$H_2$+95%Ar gas mix, with a 99.999% purity, is used for the three gas inlets in the PTA-AM system.

### 6.2.3 Powders

The powders used in these experiments had an initial powder porosity of 0.3v%. This value was obtained by viewing the cross section of the powder using an optical microscope and analysing the porosity using image analysis (Fiji Image J, version 1.8.0_172). The powders were gas atomized and had a size range of 45-105 μm, with a chemical composition provided by the supplier and shown in Table 6-1. Upper and lower limits of the ranges of chemical compositions provided in *Table 6-1* are used to identify the potential microstructure on the Schaeffler diagram (*Figure*

*2-4*), marked by a red rectangle. It is expected that possible phases could be martensite, ferrite and austenite. To confirm the present phases, electron backscattered diffraction (EBSD) analysis was conducted on the surface of one of the samples; results will be discussed in Section 6.3.2.4.

*Table 6-1 Chemical composition of 17-4PH powders, wt%.*

| Element | Composition (Supplier B) |
|---|---|
| C | 0.07 max |
| Mn | 1 |
| Si | 1 |
| Cr | 15.0-17.5 |
| Ni | 3.0-5.0 |
| Mo | - |
| Cu | 3.0-5.0 |
| S | 0.03 |
| P | 0.04 |
| Nb+Ta | 0.15-0.45 |
| O | 0.06 |
| N | 0.02 |
| Fe | Bal. |

### 6.2.4 Taguchi Design of Experiments

### 6.2.4.1 Building Walls (First DOE)

An L'18 Taguchi was designed to conduct 18 experiments using a defined combination of operating parameters from the PTA-AM system. The G-code developed for walls defined a single linear bead track, that prints 130 mm long in a back and forth manner. Using a back and forth deposition manner, as opposed to a unidirectional deposition manner, eliminates the effect of the initial bead thickness that results in gradual misalignment between either side of a build [87]. The layer height in the slicing software was set to 500 μm and a total build height of 20 mm. As a result, 40 layers were deposited for each experiment to create the walls. The thickness of the wall is a function of the size of the arc, the travel speed and powder feed rate. Each process parameter had three levels, except the nozzle offset parameter, which had two levels. Table 6-2 shows the value of each level for each respective parameter. The minimum and maximum ranges of each parameter in Table 6-2 were predetermined by previous experimental procedures that resulted in

an approximate range of the working window for each of the parameters [13]. The techniques used to analyze the resulting built walls will be discussed in Section 6.3.1.

*Table 6-2 L'18 Taguchi DOE with parameters' values.*

| Run Number | Parameter | | | | | | | |
|---|---|---|---|---|---|---|---|---|
| | Offset (mm) | Center gas (lpm) | Powder gas (lpm) | Shield gas (lpm) | Nozzle angle (degrees) | P.F.R. (g/min) | Current (A) | Table speed (mm/min) |
| 1 | 9 | 1 | 1 | 10 | 0 | 25 | 70 | 600 |
| 2 | 9 | 1 | 1.5 | 13 | 45 | 30 | 80 | 700 |
| 3 | 9 | 1 | 2 | 15 | 90 | 35 | 90 | 800 |
| 4 | 9 | 1.5 | 1 | 10 | 45 | 30 | 90 | 800 |
| 5 | 9 | 1.5 | 1.5 | 13 | 90 | 35 | 70 | 600 |
| 6 | 9 | 1.5 | 2 | 15 | 0 | 25 | 80 | 700 |
| 7 | 9 | 2 | 1 | 13 | 0 | 35 | 80 | 800 |
| 8 | 9 | 2 | 1.5 | 15 | 45 | 25 | 90 | 600 |
| 9 | 9 | 2 | 2 | 10 | 90 | 30 | 70 | 700 |
| 10 | 7 | 1 | 1 | 15 | 90 | 30 | 80 | 600 |
| 11 | 7 | 1 | 1.5 | 10 | 0 | 35 | 90 | 700 |
| 12 | 7 | 1 | 2 | 13 | 45 | 25 | 70 | 800 |
| 13 | 7 | 1.5 | 1 | 13 | 90 | 25 | 90 | 700 |
| 14 | 7 | 1.5 | 1.5 | 15 | 0 | 30 | 70 | 800 |
| 15 | 7 | 1.5 | 2 | 10 | 45 | 35 | 80 | 600 |
| 16 | 7 | 2 | 1 | 15 | 45 | 35 | 70 | 700 |
| 17 | 7 | 2 | 1.5 | 10 | 90 | 25 | 80 | 800 |
| 18 | 7 | 2 | 2 | 13 | 0 | 30 | 90 | 600 |

## 6.2.4.2  Building Shapes (Second DOE)

Based on the results obtained from the first DOE, an L'9 Taguchi was designed to print both circular and square cross-sectioned tubes (Table 6-3). These basic shapes identify the geometric

stability of the system, as well as the influence of the powder delivery angle and the travel direction. Two separate L'9 Taguchi DOEs were conducted, one for each geometry. Table 6-3 shows the value of each level used for each respective parameter. The designed circular tube size was 50 mm high and 50 mm in diameter, and each square tube was designed to be 50 mm high, 40 mm long and 40 mm wide. The dimensions of both geometries would yield similar layer perimeters (157.1 mm for circular tubes and 160.0 mm for square tubes), ensuring the heat input per deposited layer would be similar given the same process parameters. The layer height for each pass was selected to be 750 µm instead of 500 µm that was used for the walls. Even though layer height and total part height had constant values in the toolpath plan as executed by the G-code, minor manual adjustments on the control pendant were carried out to increase the torch standoff distance during the printing process of the walls to maintain a constant voltage of 34 V. It was observed that that the layers deposited for the walls were thicker than 500 µm. By increasing layer thickness in the second DOE to 750 µm, it was hypothesized that any manual adjustments during the printing process would be minimized. All shapes were single track, multi-layer builds with 66 layers. The height of 50 mm of the shapes was selected because the build process appeared to have reached steady state in terms of wall surface roughness after approximately 20 mm of build height. The perimeter dimension was selected based on the surface area of the substrates being used, where the size of four builds could fit on one substrate, while one build was printed at a time.

### 6.2.5   Characterization

### 6.2.5.1   Geometric and Metallurgical Analysis

The sample height and thickness of each build were measured using a Vernier caliper, with an accuracy of 0.01 mm. A vertical section was cut from each sample in both DOEs for metallurgical evaluation.  The sections were mounted in a thermosetting phenolic powder, ground using 240, 600, 800 µm grit papers and then polished with 9, 6, 3 and 1 µm polycrystalline diamond suspension on an EcoMet 250 Buehler polisher machine. An Olympus BX-UCB microscope was used for optical imaging. The optical images were used to detect and calculate the percentage of porosity on the surface of each sample using Fiji Image J, Version 1.8.0_172. A Wilson VH3100

Vickers hardness machine was used to obtain the hardness of the samples by taking 5 linear points on the surface of each sample, with a 5 s dwell time and 1 kg load.

*Table 6-3 L'9 Taguchi DOE with range of variables used.*

| Run Number | Parameter | | |
| --- | --- | --- | --- |
| | P.F.R. (g/min) | Current (A) | Table speed (mm/min) |
| 1 | 25 | 50 | 600 |
| 2 | 25 | 60 | 700 |
| 3 | 25 | 70 | 800 |
| 4 | 30 | 50 | 700 |
| 5 | 30 | 60 | 800 |
| 6 | 30 | 70 | 600 |
| 7 | 35 | 50 | 800 |
| 8 | 35 | 60 | 600 |
| 9 | 35 | 70 | 700 |

### 6.2.5.2 Mechanical Testing

Tensile specimens were taken from two square tubes from the second DOE to compare ultimate tensile strengths of samples printed using the PTA-AM system with other conventional manufacturing processes. The tensile specimen dimensions were made based on a sub-size version of the ASTM (SS-25), where the 25 refers to the gauge length in mm, the sub-size version had half the initial gauge length, making it ASTM (SS-12.5) [59]. The ASTM SS-25 sample dimensions are based off the smallest tensile flat samples in the ASTM E8/E8M standard [58]. An Instron 8501 tensile machine was used for the mechanical property testing using a 100 KN load cell at a deformation rate of 0.25 mm/min.

### 6.2.6 Minitab

Minitab 18 (Multilanguage) statistical analysis software, using a signal to noise ratio calculation, was used to determine the most influential parameters from the DOE on the final properties of the AM part, including build height, wall thickness, deviation of wall thickness and porosity from each printed part. Collected results are discussed in Section 6.3.1.

### 6.2.7 Heat Treatments

Several samples were heat treated to compare mechanical properties and hardness values. A solutionizing heat treatment was carried out in an ElectroFuel vacuum sintering furnace at 1040°C for 0.5 hrs. The temperature inside the furnace was ramped up to its fastest heating rate at 10°C per min to minimize any effect of grain coarsening. After the treatment was completed, the furnace was turned off and the samples were left in the furnace to cool to room temperature under an argon atmosphere. The peak aging of 17-4PH stainless steel was conducted at 480°C for 1 h in a Fisher Scientific furnace, where any dissolved copper will  precipitate [46]. After the heat treatment, samples were left to air cool outside the furnace to reach room temperature. The various combinations of heat treatments that were explored are listed in *Table 6-4*.

*Table 6-4 Heat treatments conducted on some of the samples.*

| Referred to in-text | Heat Treatment | Process |
|:---:|:---:|:---:|
| Non-HT | Non-heat treated | As-deposited |
| CA | Condition A (solutionized) | 1050°C for 0.5 hrs |
| H900 | H900 (peak aged) | 480°C for 1 hr |
| CA+H900 | Condition A+H900 | 1050°C for 0.5 hrs then 480°C for 1 hr |

### 6.2.8 FIB and EBSD

Focused ion beam (FIB) milling and electron backscatter diffraction (EBSD) were conducted on the surfaces of as-deposited samples to verify the microstructure. A Zeiss Orion machine was used

for the FIB analysis. The acceleration voltage of the gallium ions used in the FIB analysis was 30 kV, and the beam current was 7 nA. A Sigma FESEM Zeiss machine, with an Oxford NordlysNano detector was used for EBSD analysis. The acceleration voltage of electrons was 20kV. A working distance of 9.5 mm and a step size of 0.2 μm were used in collecting results.

## 6.3  Results and Discussion

### 6.3.1  First DOE Results

The oxide layer, porosity, geometrical characterization and hardness of each run were measured and analyzed. The following sections present and discuss each set of results.

#### 6.3.1.1  Oxide Layer and Porosity

The average internal porosity was measured from image analysis of the optical microscopy images for each build's vertical cross-section. A single, vertical cross section was obtained from the center of each wall. Controlling porosity is an ongoing issue for printing 17-4PH stainless steel using the PTA-AM system [13]. As a result of the process adjustments to minimize defects, the average value of porosity was determined to be 0.58% with a standard deviation of 0.26 % for all 18 walls. Only one of the 18 walls had an average porosity higher than 1%, with 1.17% porosity. Different AM processes, including PBF and SLM, result in at least 99% build densification; therefore, the lower porosity achieved using the PTA-AM process falls within the present range of porosity in other AM processes using 17-4PH stainless steel [33], [78]. Figure 6-1 shows optical images of the walls with the lower and upper porosity limits. The figures also show no presence of any oxide layers, which was investigated on the cross sections of all 18 walls. *Figure 6-2* is a cross section of one of the walls and is evidence of the lack of oxide layers in the printed parts. Larger pores sections, labeled as *cavity*, were found in the cross-sections of some of the 18 walls; however, no further analysis of them was conducted as is explained in Appendix C. Lack of complete adhesion between walls and substrate were noted in some of the walls; however, no direct mechanical effects resulted from the delamination so they are not discussed in this Chapter. Appendix D gives examples of full and partial wall adhesion.

## 6.3.1.2 Wall Characterization Measurements

Wall measurements were taken and used in the Minitab analysis to determine the most influential process parameters on the results. Wall height for all the runs was set to 20 mm, with a nominal layer height of 500 µm, resulting in 40 layers. However, the actual wall heights and respective layer heights were different from the nominal values as shown in *Figure 6-3* (the red lines mark the nominal values for total height and layer height). Layer height was calculated by dividing actual wall height for each of the 18 walls by total number of layers (40 layers).

The actual wall height measurements had an average of 22.81 mm, with 17.6 mm as a lower limit and 28 mm as an upper limit. The variation in height resulted from the changing process parameters that directly correlate to a range of layer heights. For this reason, the influence of each process parameter on final part height was analyzed. A direct correlation was found between increasing powder feed rate and the resulting increasing final part height, Figure 6-4. This implies that as powder feed rate is increased a taller build is achieved.

The resulting height variations from the different process parameters, resulted in different layer heights for each build (given in Appendix E). The preset layer height for all 18 walls was 500 µm. However, the varying layer heights in the 18 walls due to the variations in process parameters had to be controlled in order to maintain the same offset distance (and voltage: 32 V for 7 mm offset and 34 V for 9 mm offset) between the torch and substrate. To control the same offset distance, and hence voltage, manual adjustments of torch position (z-axis offset) were done during the printing process.

The wall thickness was dictated by the width of the single bead as deposited and not by G-code. It was found that wall thickness was dependent on the individual and coupling of the eight process parameters in each of the 18 walls. *Figure 6-4* shows the dependence of final part height on one of the process parameters. Likewise, *Figure 6-5* shows a linear relationship between wall thickness and layer height, indicating that thicker walls result in shorter layer heights and, thus, shorter walls (based on *Figure 6-3*). Wall thickness was at an average of 7.22 mm with a standard deviation of 1.16 mm for all 18 walls.
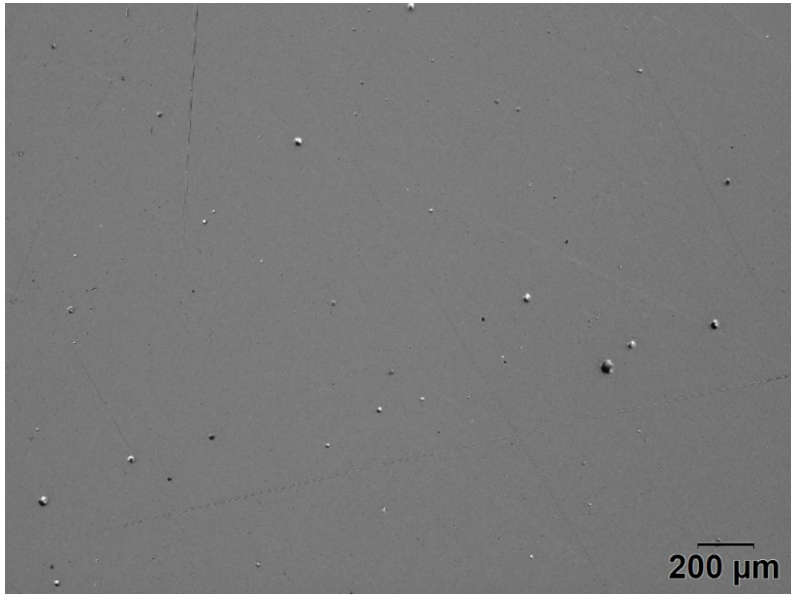
(a)
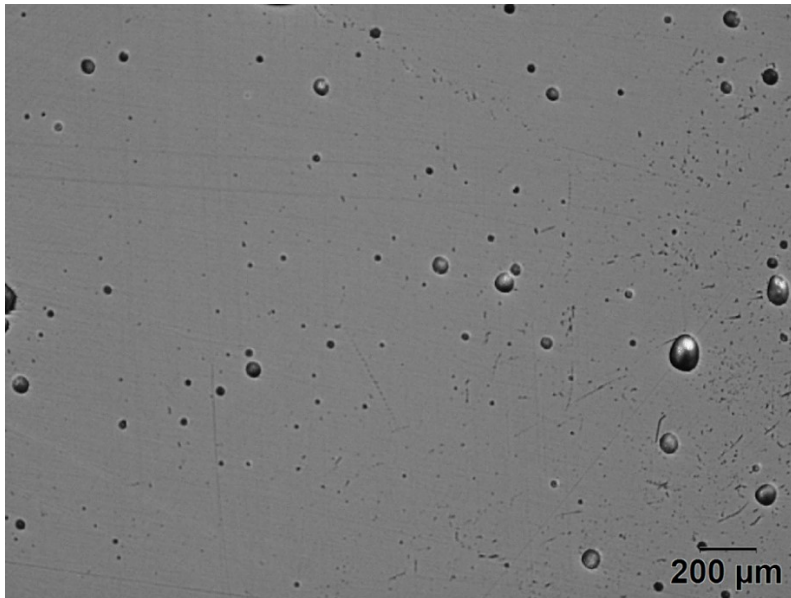


(b)

*Figure 6-1 Optical images from vertical cross-sections of the wall with the lowest porosity, 0.19% (a) and the wall with the highest porosity percentage, 1.17% (b).*
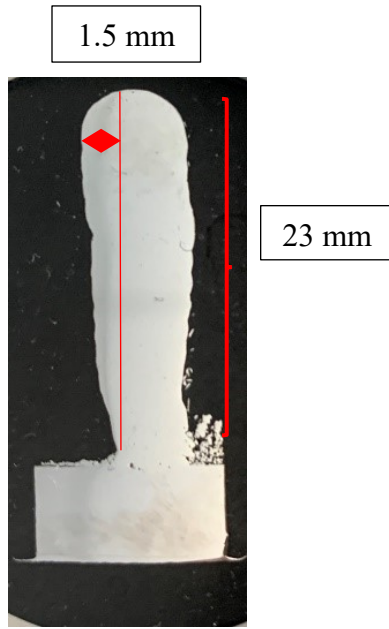
*Figure 6-2 Cross-section of one of the walls showing no oxide layers.*
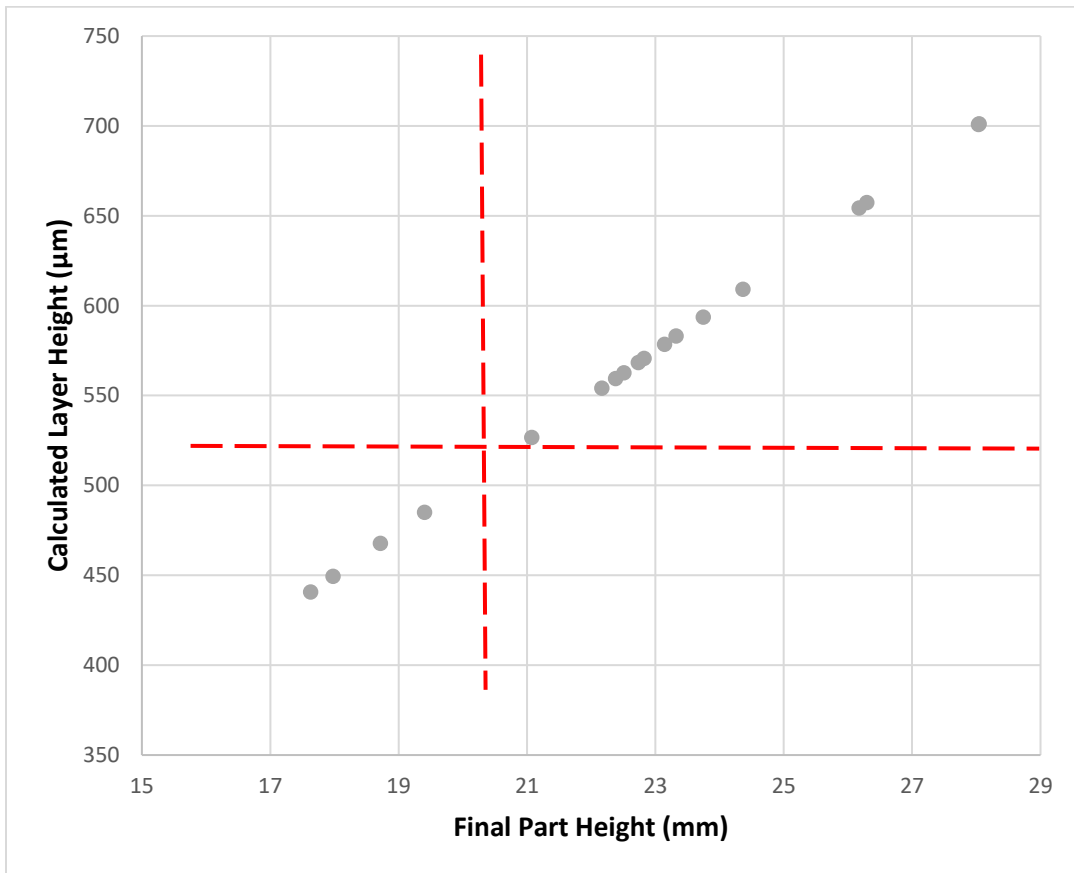


*Figure 6-3 Final wall height vs. calculated nominal layer height for all 18 walls.*
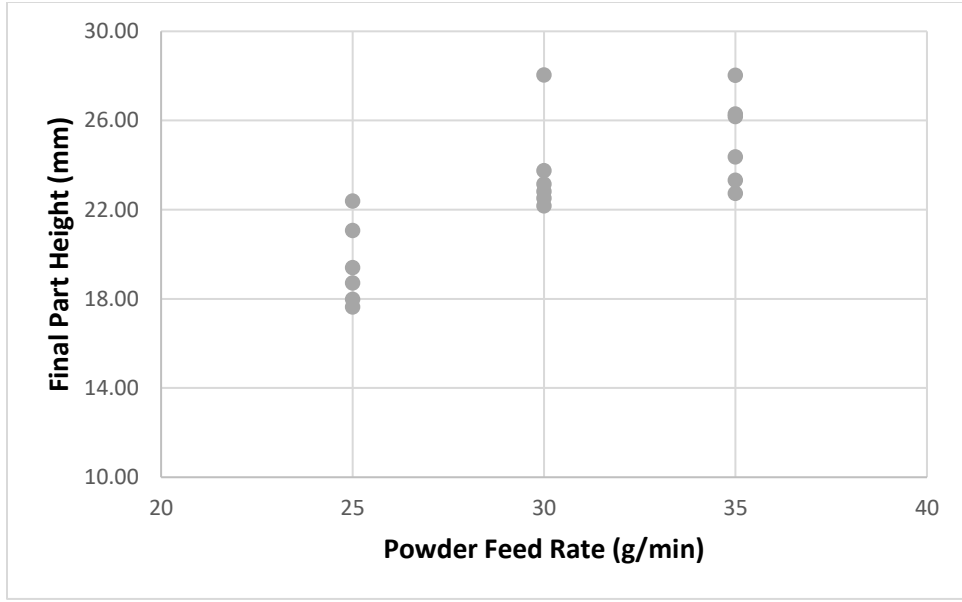
*Figure 6-4 Powder feed rate vs. final part height for all 18 walls.*
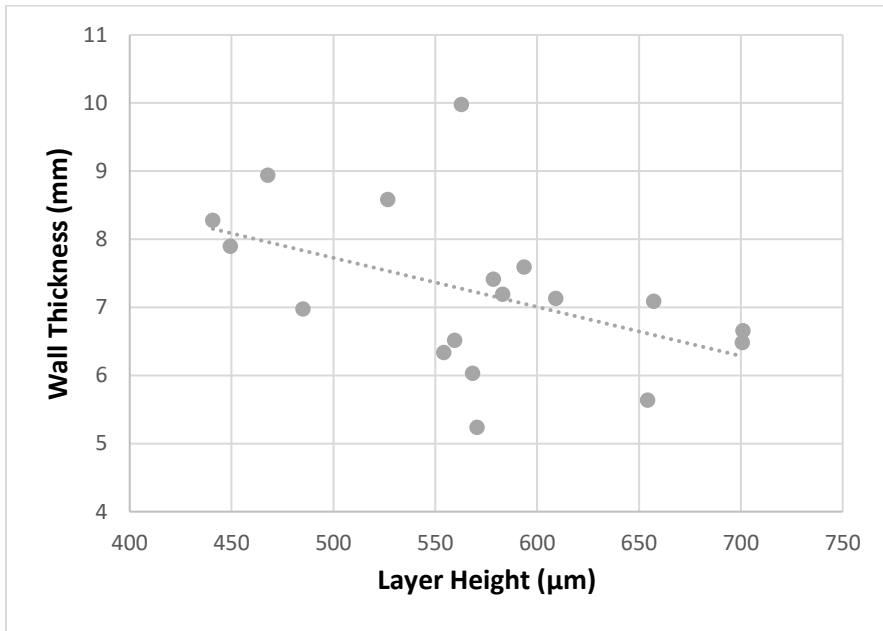


*Figure 6-5 Relationship between height and wall thickness.*

To further understand the discrepancy in total heights between all 18 walls, an analysis with non-dimensional parameters was conducted. *Heat Ratio* and *Length Ratio* are developed in Equations 6.2 and 6.3 and plotted in *Figure 6-6*. An $R^2$ value was obtained for the plotted linear line to approximate the relevance of the plotted linear line to the actual data.

$$Heat\ Ratio\colon X-axis = \frac{Heat\ input*Perimeter}{Heat\ of\ fusion*\frac{Mass}{Layer}}$$   (Equation 6.2)

$$Length\ Ratio\colon Y-axis = \frac{\frac{Height}{Layer}}{Perimeter}$$   (Equation 6.3)

Where the units of each parameter are as follows: heat input (J/mm), perimeter (mm), heat of fusion (J/g), mass/layer is g/layer and height/layer is mm/layer. The mass/layer was calculated by multiplying the actual volume of deposited steel, respective to each geometry and associated actual height, with the density of the 17-4PH stainless steel.

*Heat Ratio* is the relationship between the amount of heat going into each layer of the printed part defined by the process and the amount of energy required to completely melt powders of single layer of the printed part. Ultimately, *Heat Ratio* translates into the excess heat left in the system after powders are melted. The heat of fusion for 17-4PH stainless steel was obtained from Thermocalc 2020a (Appendix F) and found to be approximately equal 217 J/g. The mass/layer was calculated using the following Equation:

$$\frac{Mass}{Layer} = Powder\ feed\ rate \ * \ \frac{Time}{Layer} = g/layer$$   (Equation 6.4)

The time/layer was calculated by dividing the perimeter of the part by the table speed in that respective run.

The *Length Ratio* is the relationship between the height of each layer and the respective perimeter of each geometry. As perimeter is calculated as a constant value for the experiments, respective to geometry, *Length Ratio* basically refers to layer height.
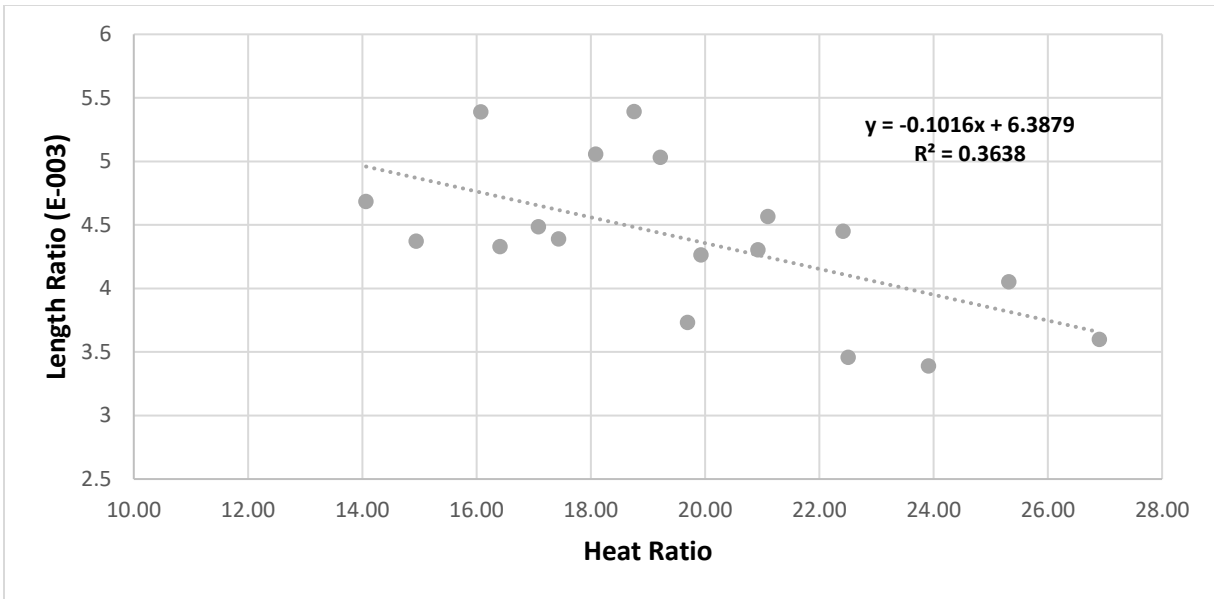
*Figure 6-6 Heat Ratio vs. Length Ratio for all 18 walls.*

From Figure 6-6, it is shown that increasing the *Heat Ratio* (the excess heat in the system) results in a lower *Length Ratio* (layer height). This relationship explains the resulting increased thickness of shorter walls, concluding that shorter walls were thicker as a result of excess heat in the system. More excess heat in a system leads to longer solidification times. Additionally, more excess heat results in reduced viscosity of the melted powder, lower surface tension and a lower contact angle with the substrate. The decrease in all these three phenomena increases the flowability of the melted powder and increase surface wettability, which allow for thicker walls to form.

Maximum wall deviation was measured from the vertical cross sections of each of the walls, as shown in *Figure 6-2*. This measurement was assessed as follows. A vertical line was drawn perpendicular to the substrate using the origin as the surface of the wall with the substrate. The maximum wall deviation from this perpendicular line was measured as shown in the red diamond in Figure 6-2. The average maximum wall deviation for all the walls was 1.7 mm, with a lower limit of 0.9 mm, an upper limit of 3 mm and a standard deviation of 0.53 mm. A linear correlation was found between maximum wall deviation and wall thickness. An increasing wall thickness led to higher maximum wall deviation, *Figure 6-7*. Based on *Figure 6-5* and *Figure 6-7*, it can be concluded that thicker walls result in higher maximum wall deviations and lower overall heights due excess heat in the build.
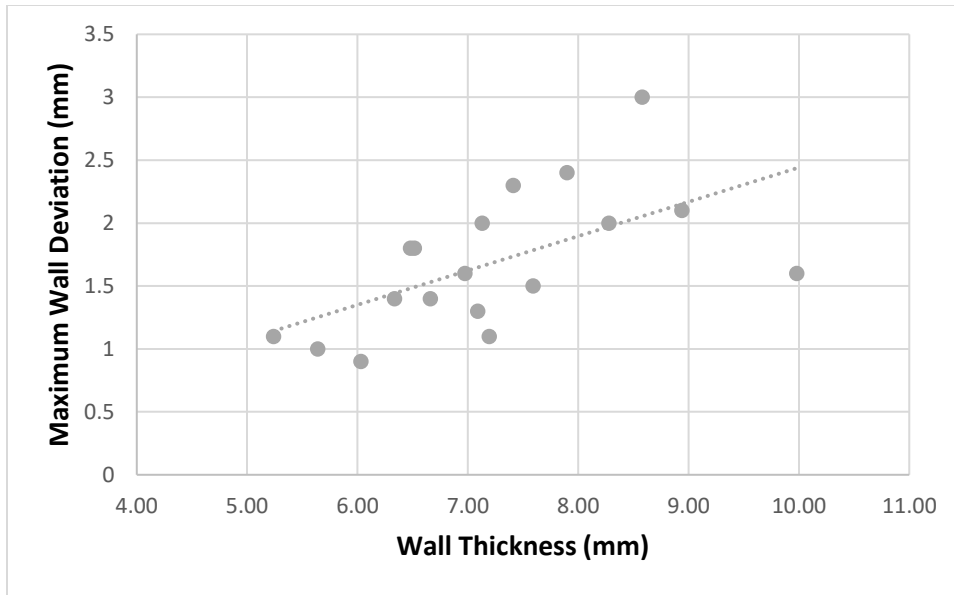
*Figure 6-7 Relationship between maximum wall deviation and wall thickness.*

### 6.3.1.3   Hardness

A correlation between heat input and as-built hardness was sought to verify whether higher heat inputs resulted in lower hardness values. The relationship between as-built hardness and calculated heat input is shown in Figure 6-8.

The expected range of hardness values from the literature [42], [46], [68] are identified by the black box shown in *Figure 6-8*.  The as-built hardness results show that the majority of the data points fell within the upper range of the expected hardness values of 17-4PH stainless steel prior to aging  [42], [46]. Analysis of the upper range of hardness results will be discussed in a later section. Moreover, no direct correlation could be made between hardness and heat input (*Figure 6-8*) or between hardness and all eight parameters (results given in Appendix G). This could indicate that the difference in heat inputs between the 18 walls was not significant enough to directly affect hardness. Because the hardness results fell within the expected range of 17-4PH stainless steel and were not directly or inversely related to any of the process parameters, hardness was not added to the statistical analysis.
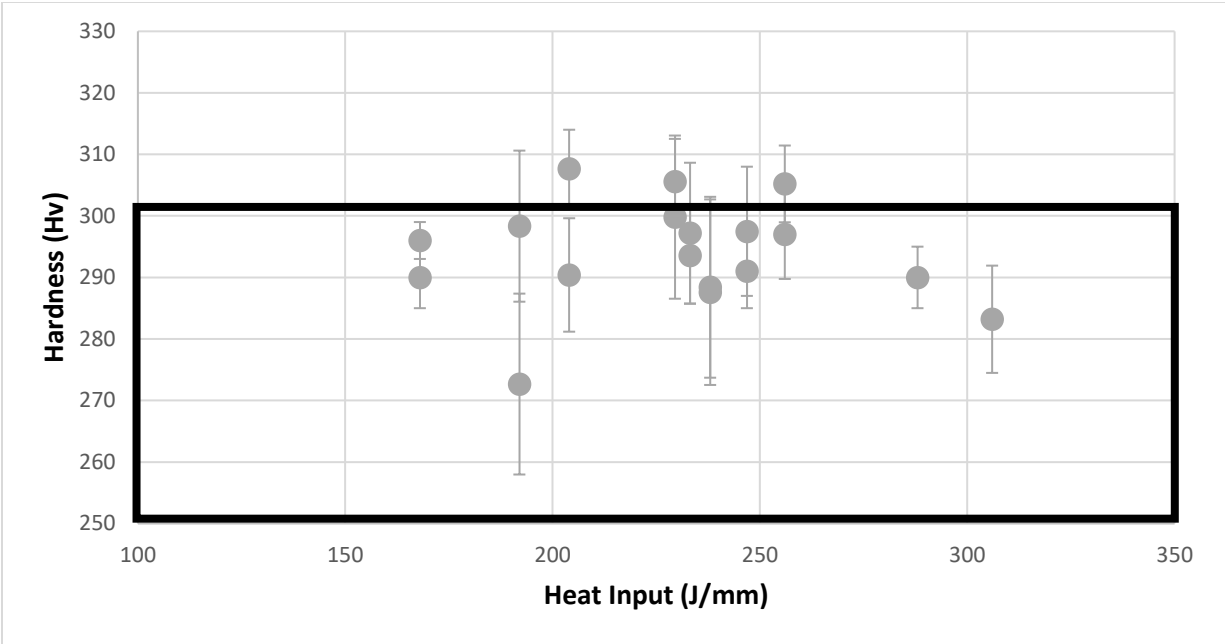
*Figure 6-8 Hardness vs. heat input results for all 18 experiments, with the expected hardness range shown by the black outline.*

### 6.3.1.4 Minitab Analysis

Signal to noise ratio is a method on Minitab that is used to identify which process parameters reduce variability in a process, while minimizing the effect of other noise parameters. The response characteristic for each process parameter that is computed by Minitab include the means and signal to noise ratios (details are given in Appendix H). Each table provides information on the level of influence of each process parameter on the selected response, resulting in a ranking of process parameter. For each process parameter, a delta value is computed, which refers to the difference between the highest and lowest average response characteristic values for each process parameter. In order to rank the results obtained from Minitab, the sum of each delta values for each individual respective parameter was calculated, as shown in Table 6-5. Ranking the total sums of each delta value by sorting them in ascending order for the eight parameters yields the results in Table 6-5.

*Table 6-5 Delta values for each parameter from all four measured results.*

| Output | Delta value for Variable | | | | | | | |
|---|---|---|---|---|---|---|---|---|
| | Offset (mm) | Center (lpm) | Powder (lpm) | Shield (lpm) | Nozzle (°) | PFR (g/min) | Current (A) | Speed (mm/min) |
| Thickness (mm) | 0.96 | 1.43 | 1.19 | 1.11 | 1.38 | 1.51 | 0.76 | 0.52 |
| Porosity (%) | 2.471 | 2.497 | 2.034 | 3.589 | 2.001 | 6.779 | 3.019 | 4.079 |
| Height (mm) | 0.975 | 1.267 | 1.954 | 5.544 | 2.62 | 10.413 | 4.232 | 3.395 |
| Maximum Wall Deviation (mm) | 1.855 | 2.293 | 2.016 | 1.362 | 1.971 | 4.247 | 1.636 | 0.905 |
| Total | 6.261 | 7.487 | 7.194 | 11.605 | 7.972 | 22.949 | 9.647 | 8.899 |
| Rank | 8 | 6 | 7 | 2 | 5 | 1 | 3 | 4 |

The ranked results from *Table 6-5* indicate that powder feed rate was the most influential parameter followed by the shielding gas and current. However, Minitab also produces results on the 'optimized' value of each parameter (given in Appendix H). An optimized value indicates that a certain value of a parameter showed the most favorable outcome for a given result (including wall height, thickness, porosity and maximum wall deviation). This 'optimized' value is selected from the three different values that were given for each parameter in Table 6-2. Shielding gas repeatedly showed an optimized value at 13 lpm in the analysis, for that reason, it was decided that shielding gas was to be kept as a constant parameter for the second DOE. Center gas was optimized at 2 lpm, similarly with the powder gas. The offset distance was optimized at 7 mm, (32 V) and the nozzle angle was to be kept at 45°. Single track walls are not complex shapes and do not require a change of powder deposition angle during the printing process. However, to print parts such as circular and square cross-sectioned tubes, the nozzle angle depositing powder changes its orientation either in a circular manner or from side to side during the printing process, respectively for either geometry. For this reason, a 45° nozzle angle was deemed most consistent in its powder deposition for more complex shapes than walls.

To further explain the effect of nozzle angle on the wall build, *Figure 6-9* shows the powder outlets with respect to the build geometry. These geometries are used in the second DOE. The orange circle refers to the torch location at two different points in time, on the same geometry, and the

two black circles refer to the location of the powder ports depending on the selected nozzle angle. Having the powder ports at 45° will lead to the least change in powder deposition angle during the printing process of both geometries, as compared with 0° and 90°. From *Figure 6-9*, it can be seen that angles 0° and 90°, in both circular and square cross-sectioned tubes, result in a 90° change in nozzle angle as the torch moves from one side of the build to the other. Such a change is not witnessed in the 45° nozzle angle as the same nozzle angle is maintained throughout the entire part. This justifies the choice of 45° nozzle (port) angles in circular and square cross-sectioned tubes. However, it must be noted that the change in the corners of the square tubes results in milliseconds of slower table speed, a phenomenon that does not occur in the consistent rotational shape of a circular tube. The slightly slower table speed on the corners of the square tubes are likely to result in more excess heat in those corner locations.
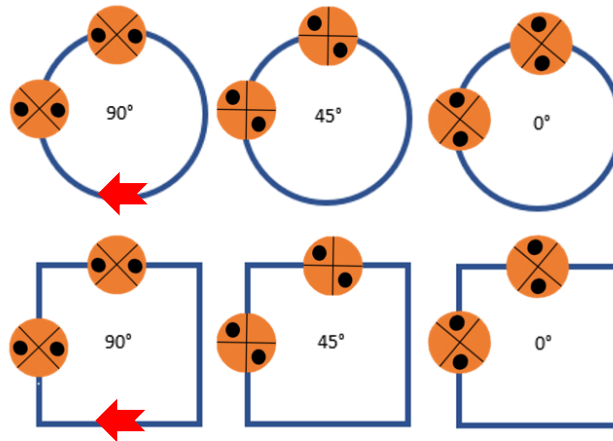


*Figure 6-9 Location of powder ports on circular and square cross-sectioned tubes with three different nozzle angles: 90°, 45° and 0°. Direction of motion is indicated by red arrows.*

Referring to *Table 6-5*, table speed is ranked highest after powder feed rate, shielding gas and current. Because shielding gas was to be kept constant, powder feed rate, current and table speed were selected as the variable parameters in the second DOE. All the other parameters were kept constant at the 'optimized' values calculated from the Minitab analysis. *Table 6-6* summarizes the parameters that will be used in the second DOE.

*Table 6-6 Summary of optimized parameters from DOE and range to be explored for the most influential factors.*

| Parameter | Value |
|---|---|
| Offset (mm) | 7 (32 V) |
| Center Gas (lpm) | 2 |
| Powder Gas (lpm) | 2 |
| Shield Gas (lpm) | 13 |
| Nozzle Angle (°) | 45 |
| Powder Feed Rate (g/min) | 25-35 |
| Current (A) | 50-70 |
| Table Speed (mm/min) | 600-800 |

### 6.3.2   Second DOE

The second DOE was designed to assess the variation of powder feed rate, current and table speed operational values that would result in the building of geometrically and metallurgically stable simple 3D shapes. Parameters summarized in *Table 6-6* are used for all the following experiments. Results from the second DOE would identify an operation window for deposition of 17-4PH stainless steel using the PTA-AM system to allow for process repeatability and reproducibility. To ensure that the three process parameters are consistent for different geometries, the second DOE was repeated for two different CAD files: circular tubes and square tubes. Figure 6-10 shows examples of a circular tube (Run 2-5) and square tube (Run 2-2).
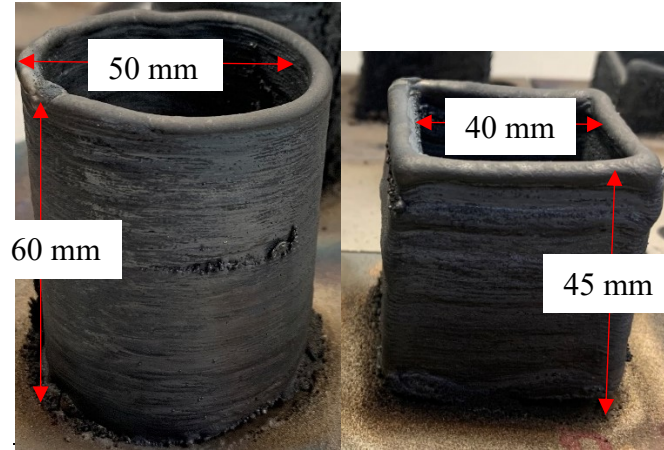
*Figure 6-10 Examples of circular tube (left) and square tube (right) using parameters from the second DOE.*

### 6.3.2.1   Part Thickness and Porosity

All experiments listed in Table 6-3 were successful and only minor visual variations in geometry were noted. Porosity, wall thickness, final part height and hardness were measured for each deposit. Porosity for all 18 parts in the second DOE was at an average of 0.48% with a 0.25% standard deviation. Low values of porosity were attained by ensuring that there is sufficient heat input to melt all powders and prevent lack of fusion porosity, as explained in the previous section. No direct correlation was found between porosity and any of the three variable parameters in the second DOE (data given in Appendix I).

Circular tubes had an average wall thickness of $5.2 \pm 0.45$ mm, while square tubes had an average wall thickness of $5.10 \pm 0.33$ mm. Results from *Figure 6-11* show the relationship between part thickness and current, powder feed rate and table speed. From the heat input equation (given by Equation 6.1), heat input is directly dependent on current and inversely dependent on table speed. Results in *Figure 6-11* (a) and (c) support the two relationships: as current increases, heat input increases (and excess heat) resulting in thicker parts, while faster table speeds do not allow for the lingering of excess heat in the system and result in thinner parts. Increasing powder feed rate in the system results in the printing of taller builds (as will be explained in the next section), taller builds result in thinner parts as observed by *Figure 6-11* (b).

The lower variation in part thickness in the second DOE as compared with the wall thickness from the first DOE (average 7.22 mm with a 1.16 mm standard deviation) is likely attributed to the higher heat inputs used in the first DOE and the larger layer height in the second DOE. The heat input of the system must be sufficient to completely melt the powder; however, too much heat in the system can result in slumping and thicker overall builds. Figure 6-12 illustrates the linear relationship between increasing heat input with larger part thickness for walls and circular and square tubes and highlights the thicker walls produced by the higher heat inputs in the first DOE.
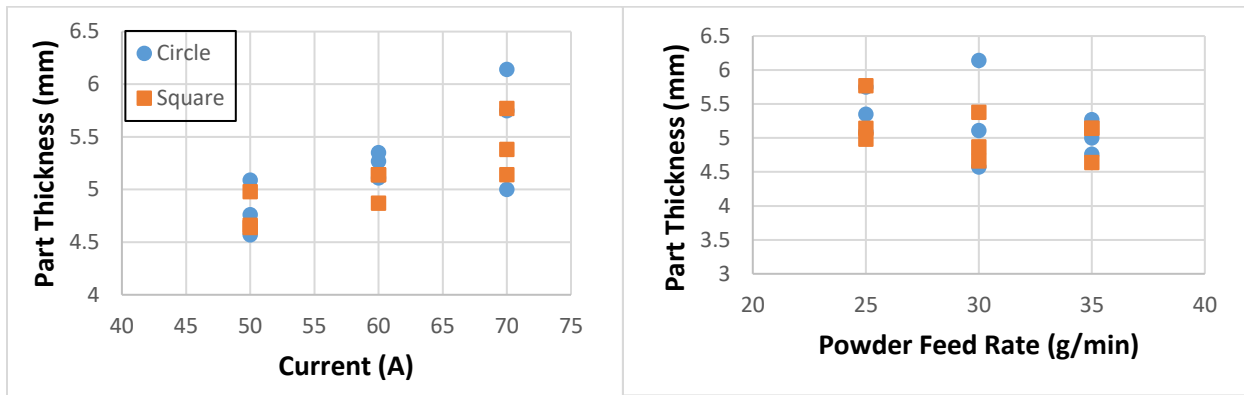


(a)

(b)
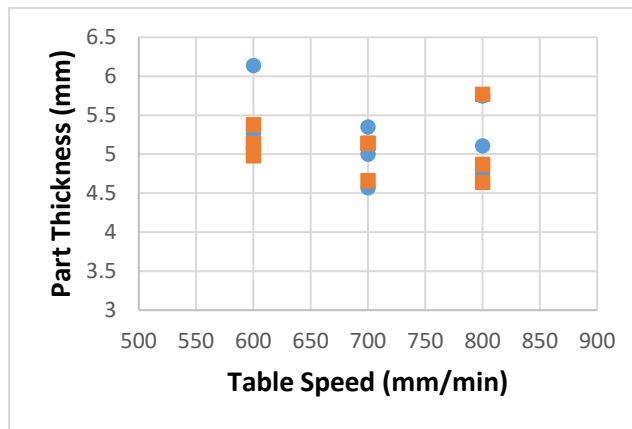


(c)

*Figure 6-11 Part thickness is plotted against a) current, b) powder feed rate and c) table speed for all circular and square tubes.*
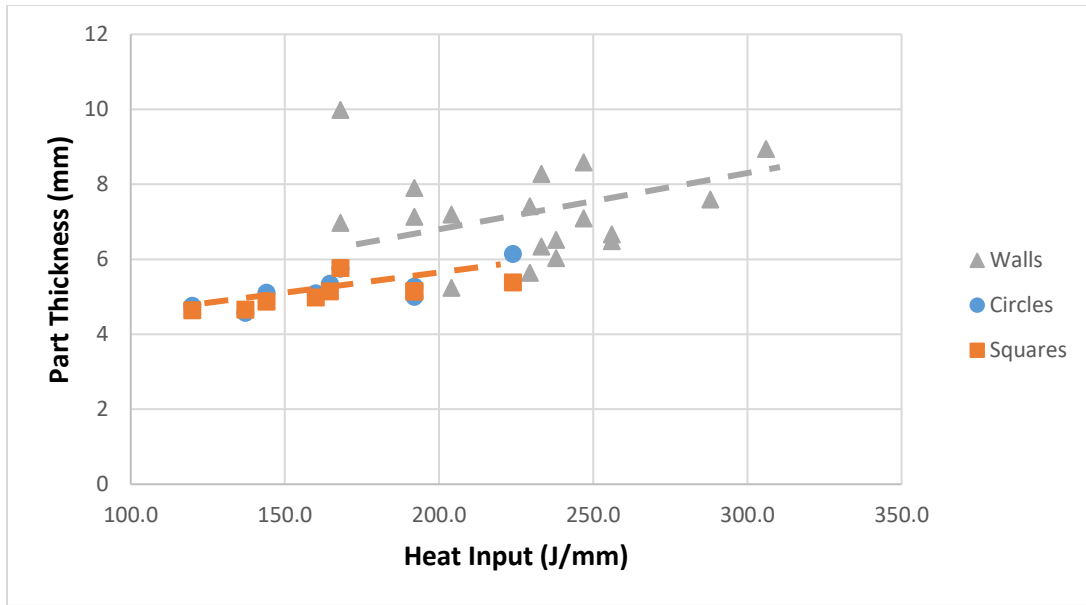
*Figure 6-12 Heat Input vs. Part Thickness for walls and circular and square tubes.*

### 6.3.2.2 Part Height and Influence of Geometrical Differences

The final part height was measured and evaluated as a function of current/PFR/table speed as shown in *Figure 6-13*. It can be observed that final part height has a linear relationship with powder feed rate and an inverse relationship with current and table speed. From *Figure 6-13* (a), increasing current results in higher heat input and, thus, higher excess heat in the system, resulting in slumping and shorter parts. *Figure 6-12* shows that increasing heat input results in thicker parts, which agrees with higher current resulting in shorter walls. *Figure 6-13* (b) verifies that adding more powder in the system linearly results in the printing of taller builds. Even though current and table speed have inverse effects on heat input (based on Equation 6.1), increasing table speed results in shorter builds, according to *Figure 6-13* (c), instead of taller builds. Powder lost is a potential explanation to this phenomenon, which will be discussed in a later in this section. The final part height varied between 42 and 88 mm, which is a significant deviation from the design height of 50 mm.
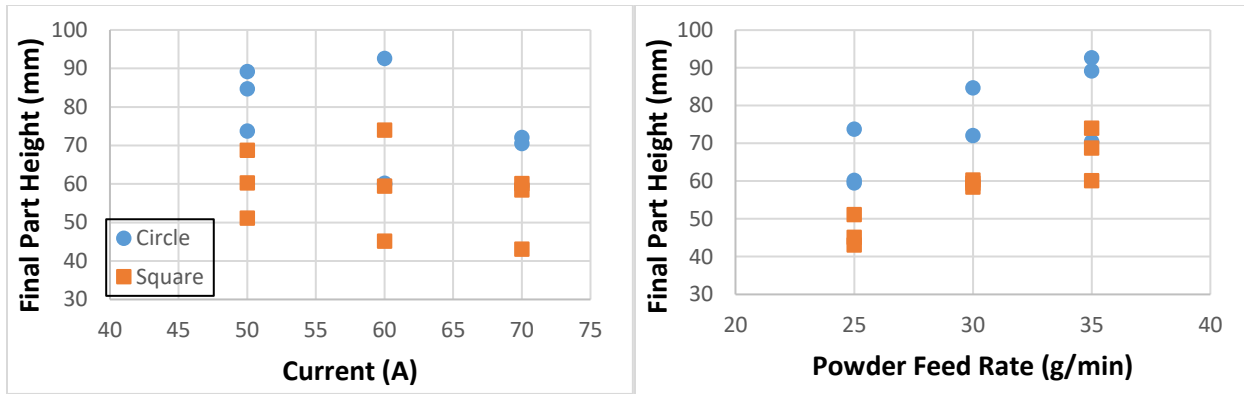
(a)

(b)
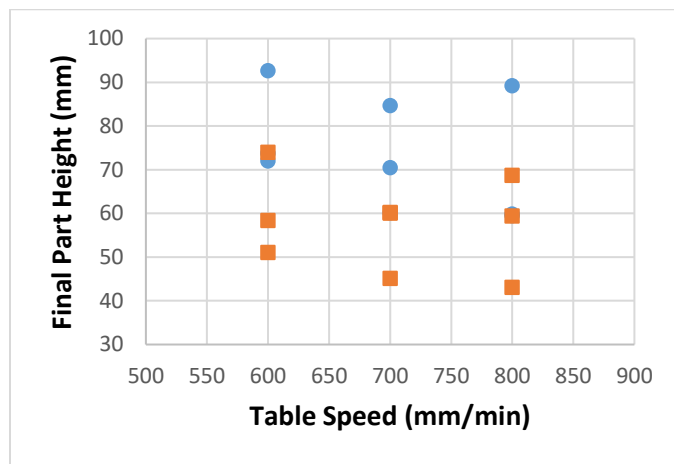
(c)

*Figure 6-13 Final part height is plotted against a) current, b) powder feed rate and c) table speed for all circular and square tubes.*

Although 66 layers were printed, with a pre-determined layer height of 750 um, it can be seen in *Figure 6-14* that the calculated layer height varies directly with part height, between 646 μm to 1270 μm. It is clear that a consistent nominal layer height of 750 um is not reflected in the DOE and layer height is a function of operational parameters. To keep the offset roughly constant at 7 mm, manual adjustments were made during the build. Changes in torch position were done to minimize any effect of changing voltage during the printing process. In order to avoid manual adjustments during the printing process in the second DOE as compared with the first, layer thickness was changed to 750 μm instead of 500 μm. From *Figure 6-6*, *Length Ratio* 4.7E-003 corresponds to the least excess heat (*Heat Ratio*) from all 18 walls. The least excess heat in the

system is what was desired for the next DOE. Accordingly, an inverse problem of Equation 6.3 is used to identify the corresponding layer height of a 4.7E-003 *Length Ratio*. If *Length Ratio* is kept as a constant in Equation 6.3, with total height kept at 50 mm (desired square tube height in the second DOE) and perimeter is kept at 157 mm (desired perimeter of square tubes), a new value for number of layers is calculated.  Dividing 50 (desired square tube height) by the new calculated number of layers results in the new theoretical layer height. The new resulting layer height, rounded to 750 μm, is based on the lowest excess heat from the first DOE. However, from Figure 6-13, it is evident how final part height and, consequently, layer height are directly dependent on process parameters. Accordingly, for future experiments, it is recommended that layer height should not be kept as a constant in the G-code and should depend on the selected process parameters for each individual run. It is also observed in *Figure 6-14* that the circular tubes had taller builds than the square tubes, and that the variation is build height for the square tubes is larger than that of the circular ones.  This will be explored further in this chapter.

Dependence of part width on different process parameters (*Figure 6-11*) and the resulting shorter square tube builds as compared with circular builds (*Figure 6-14*) require further analysis. *Figure 6-15*, is an example of a circular and square cross-sectioned tube with the same process parameters. Arrows point at the square tube indicating bulged corners indicating that more mass per unit distance is present in the corners of the square tube.

The excess heat observed in the square tubes in *Figure 6-15* is further analyzed by comparing layer height and part thickness. *Figure 6-16* graphs layer height versus part thickness for all parts, where the average thickness for all parts (5.15 mm) is marked by a black line. It can be observed from the graph, however, that as layer height increases, the part thickness decreases (as marked by the red line), indicating a conservation of mass during the printing process. Since square tubes have lower layer heights, they also have larger part thicknesses, indicating some slumping in the square tubes. This confirms the outcome of *Figure 6-16*, which explains that the larger layer height in circular tubes indicates that more of the heat going into the system is actually used up in melting more powders to achieve taller builds, as compared to square tubes. Scale build up on both parts may also be attributed to the change of powder deposition during the printing process and the possible deflection of powder.
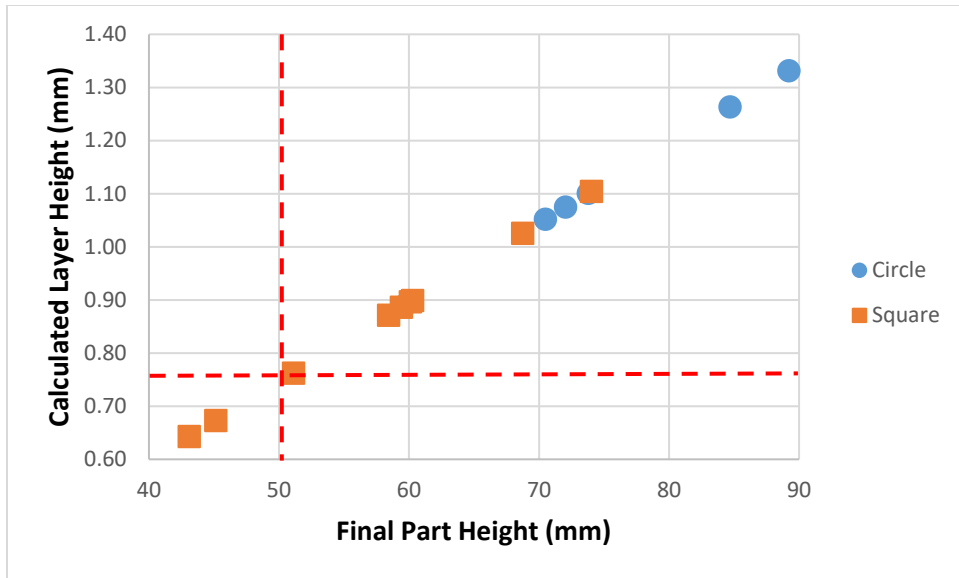
*Figure 6-14 Final part height versus calculated layer height for all parts.*
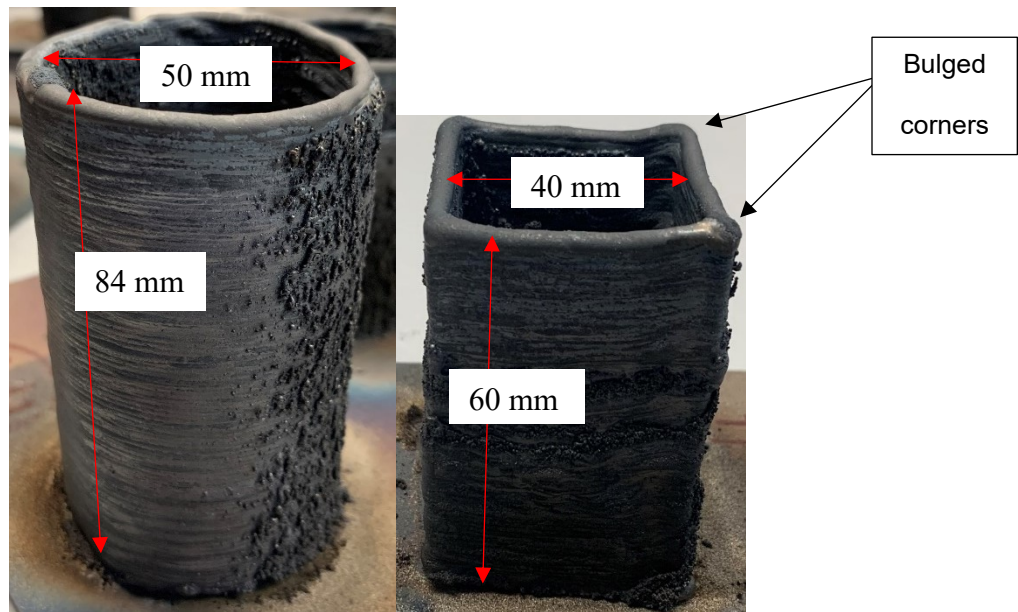


*Figure 6-15 Circular and square cross-sectioned tubes with same heat input (137 J/mm) but different heights. Square tube showing bulged corners.*
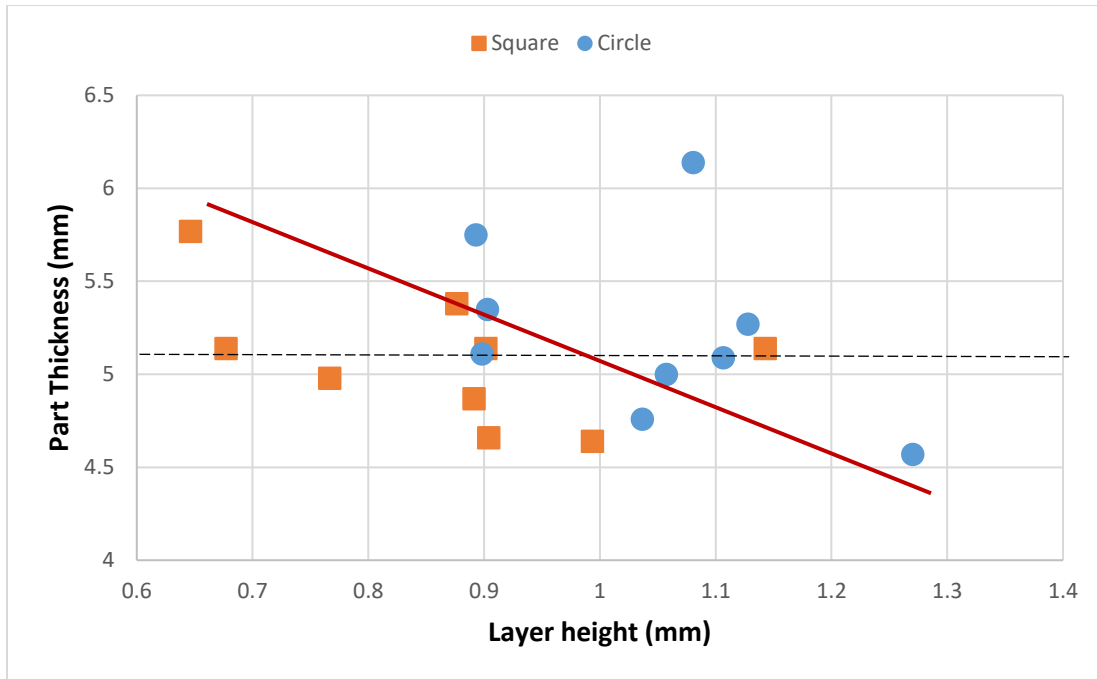
*Figure 6-16 Relationship between layer height and part thickness. The black line marks the average part thickness (5.15 mm), and the red line marks the trend of decreasing part thickness with increasing layer height.*

Slumping did not occur at the corners of all the square tubes. This indicates that there must be another phenomenon taking place with square tubes compared to circular tubes, resulting in shorter builds. Since the powder feed rate was constant for both the circular and square tubes, it could be hypothesized that less powder is actually being melted in the square tubes than the circles, as there was more excess heat in the square tubes than the circular ones. With less powder being melted, the actual mass per layer would be less for the square tube than the circular tube. The percentage of powder lost was calculated based on the difference between the volume of each deposited layer and the delivered volume of powder based on the powder flow rate. The relationship between percentage of powder lost and overall heat input is shown in *Figure 6-17*. It can be observed that square tubes have a higher percentage of powder lost compared to circular tubes, up to 30% powder lost in some cases. If more powder is being lost when building the square tubes, it would be safe to assume that the layer height is smaller. It also indicates that geometry plays a crucial role in the percentage of powder lost, as shown by the difference in build height for circle and square tubes deposited using the same operating parameters. Even though nozzle angle is constant for both geometries at 45°, it is likely that the several abrupt changes in printing directions (due to the sharp

corners of square tubes) can lead to less powder utilization efficiency and, thus, more powder losses. Moreover, the travel speed of the circular tubes remains constant for every layer, as compared with the slightly slower speeds due to the presence of corners in square tubes, and hence the amount of powder lost is significantly less in circular tubes.
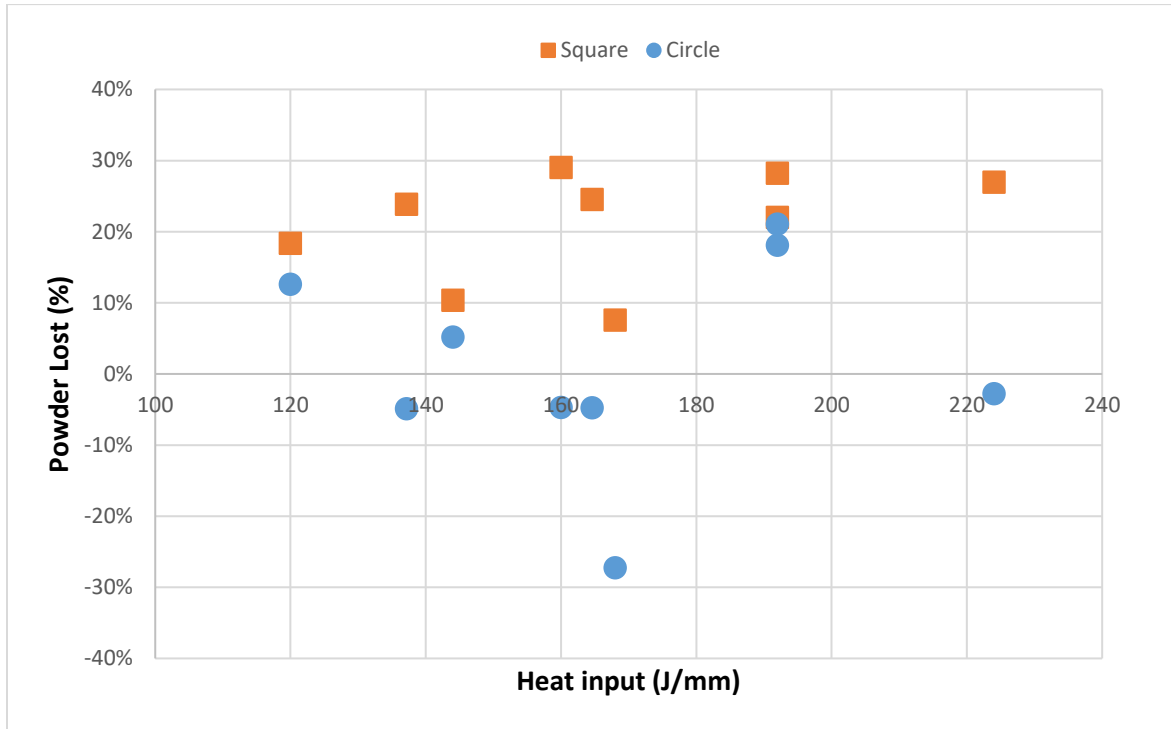


*Figure 6-17 Relationship between powder loss and heat input between square tubes and circular tubes.*

The *Heat Ratio* and *Length Ratio* analysis presented in the first DOE was completed on the results from the second DOE to further understand the discrepancy in layer height between both geometries in the second DOE. Shown in Figure 6-18, the increasing *Heat Ratio* (excess heat in overall system) results in a decreasing *Length Ratio* (referring to layer height). Circular tubes tend to have a lower *Heat Ratio* and higher *Length Ratio* compared to square tubes. This indicates that building circular tubes requires less excess heat and have higher layer heights, which will result in printing taller builds for a constant number of layers. Conversely, building square tubes results in more excess heat and smaller layer heights. The extra milliseconds required to change table direction when building square tubes, as previously noted, is likely to be cause for the excess heat presented in *Figure 6-18*.
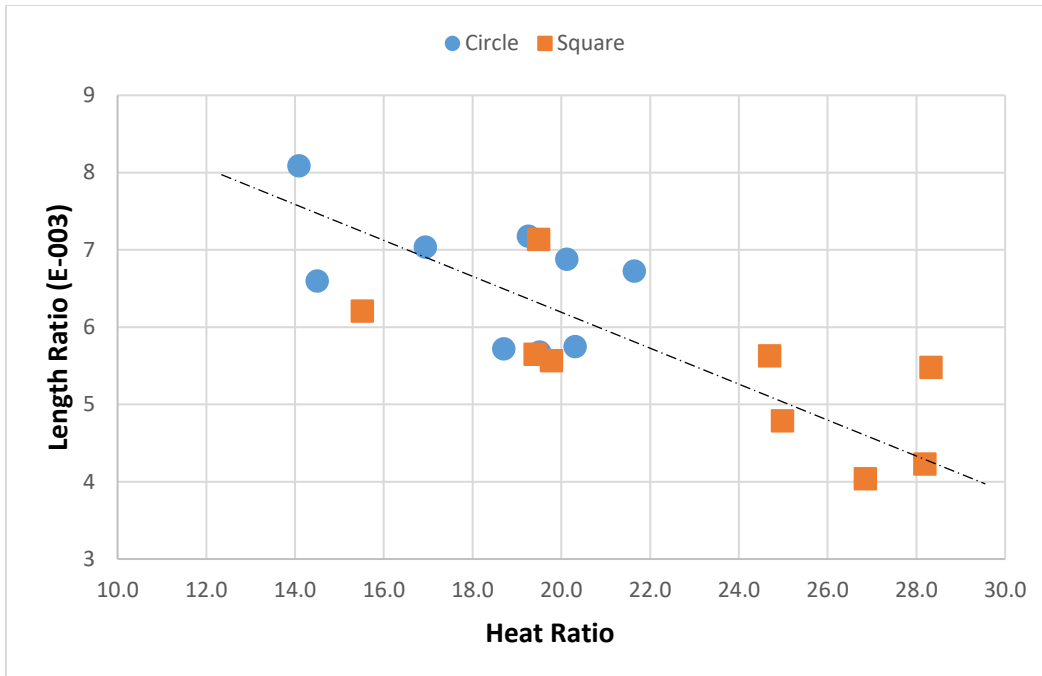
*Figure 6-18 Relationship between Heat and Length Ratios.*

### 6.3.2.3  Mechanical Properties and Heat Treatments

The relationships between hardness and current, powder feed rate and travel speed were analyzed. No correlation between hardness and current/powder feed rate was found (Appendix I); however, one was found between hardness and table speed (*Figure 6-19*). Faster table speeds result in less excess heat and faster cooling rates, faster cooling rates result in higher hardness results [88], [89].

The relationship between hardness and heat input is shown in Figure 6-20. The marked red rectangle indicates the region of average hardness of conventionally produced 17-4PH stainless steel prior to heat treatment as ranging between 250-300 Hv [42], [46], [68]. No direct correlation was found between the compounded effect of heat input on hardness; however, the correlation holds true based on the results in *Figure 6-19* and the relationship between heat input and table speed based on Equation 6.1. Circular tubes, in most runs, appear to have higher hardness values than square tubes with identical process parameters. *Figure 6-18* identifies the higher excess heat (higher *Heat Ratio*) present in the square tubes as compared with the circular tubes. As explained earlier, the higher excess retained heat in square tubes can result in slower cooling rates and, consequently, relatively lower hardness values [88], [89], observed in *Figure 6-20*.
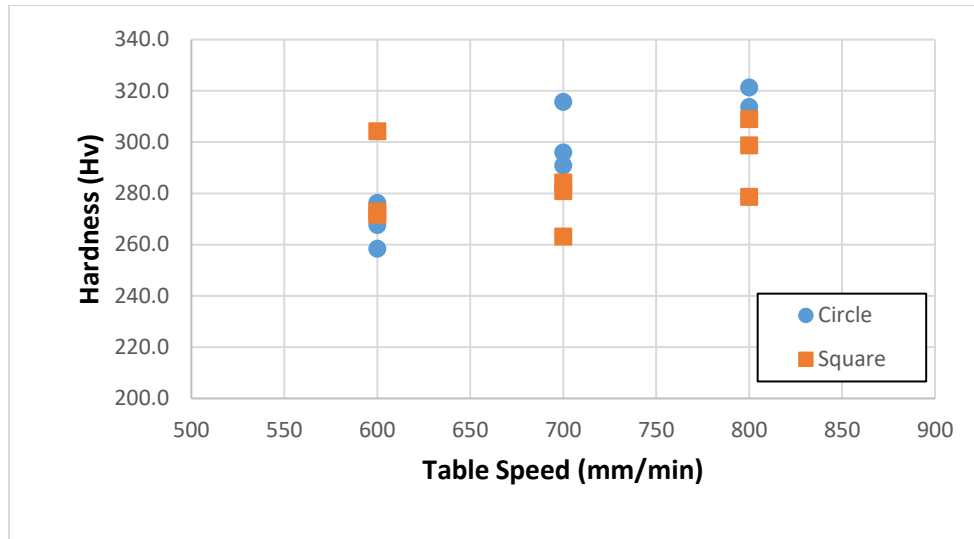
*Figure 6-19 Hardness vs. table speed for all circular and square tubes.*

Approximately 66% of data points in *Figure 6-20* (12 out of 18 samples) fall within the expected hardness range for 17-4PH stainless steel. It has been reported in literature that WAAM, a DED processes, has reached temperatures of at least 450°C during the printing process of steel with a heat input of 570 J/mm, speculating that the precipitation of some copper particles prematurely is possible and thus lead to higher hardness results [28], [38]. In the current PTA-AM experiments, heat inputs ranged between 150-306 J/mm; however, the influence of the added heat input due to the hydrogen in the gas mix of the three gases is not incorporated into Equation 6.1. Additionally, even though no direct heat measurements were taken from the PTA-AM system during the printing processes, peak temperatures of plasma arcs are thought to reach local temperatures of over 16000°K [90]. The hypothesis of higher hardness results in the as-deposited stage, due to the precipitation of some copper particles, as compared with the expected average of 17-4PH stainless can explain the higher hardness results shown in Figure 6-20. The same hypothesis can be used to explain the higher than average hardness results in the printed walls, Figure 6-8.
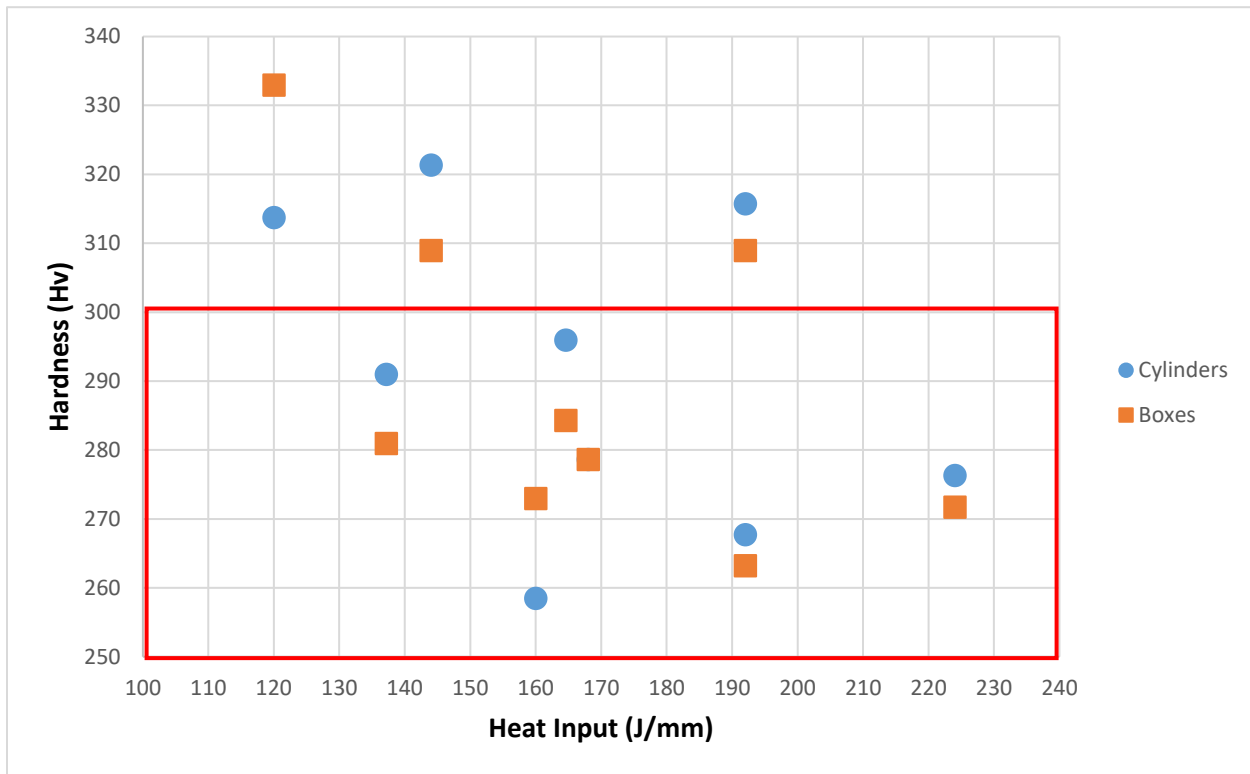
*Figure 6-20 Relationship between hardness and heat input.*

The effect of heat treatment on the mechanical properties was evaluated. The flat surfaces from the square tube samples were more conducive to prepare flat tensile coupons than the curved circular tube samples. It is expected that circular tube samples would have even higher tensile properties than square tubes, based on the higher hardness values they obtain (*Figure 6-20*). Lower excess heat results in faster cooling rates and higher hardness values [88], [89]; higher hardness is linearly related to higher tensile strength [89]. For those reasons, it is expected that the tensile values obtained from the square tubes will be giving the minimum obtainable tensile properties printed from 17-4PH stainless steel using the PTA-AM system. Square tubes 2-4, 2-5, 2-7 and 2-8 (parameters listed in *Table 6-3*) had the lowest *Heat Ratios* (*Figure 6-18*) amongst all square tubes, indicating that they had the least excess heat going into their builds. However, square tubes 2-7 and 2-8 had higher *Length Ratios* than square tubes 2-4 and 2-5. Higher *Length Ratio*s indicate better powder utilization efficiency and less powder lost during the printing process. Moreover, square tubes 2-7 and 2-8 had the minimal scaling on their exteriors, smooth layer transitions throughout and no visible effect of excess heat apparent in the corners of the build, as compared

104

with all square tubes. Their heat inputs were 120 J/mm and 192 J/mm, respectively. For the above reasons, square tubes 2-7 and 2-8 were selected for the analysis in the coming section.

The peak aging heat treatment of 17-4PH stainless steel results in the precipitation of copper particles and optimal mechanical properties [46], [48], [91]. However, a solutionizing treatment of 17-4PH stainless steel must take place before peak aging to ensure that all solutes are in solid solution, resulting in a homogenized microstructure [48]. A controlled, in-furnace, argon cooling process is conducted on the solution treated samples after the 0.5 hrs of heating at 1040°C. The samples are not taken out of the furnace to prevent from oxidation. However, there is very little information in literature about the dissolution rate of copper during the cooling process, making it difficult to confirm the needed cooling rate to ensure complete dissolution [92]. The rate of argon cooling inside the furnace was set to 10°C/minute; this rate was selected based on the capabilities of the furnace.

Square tubes 2-7 and 2-8 were divided into four sections and each section underwent the following heat treatment, as listed in *Table 6-4*: non-HT (as-deposited), solution treated (CA), peak aged with no solution treatment (H900), and solution treated and peak aged (CA+H900). Tensile and hardness results were collected for all samples. However, square tube 2-8 in the four conditions prematurely failed and the results were not added in the following section. Ultimate tensile strength of wrought 17-4PH stainless steel after heat treatment is approximately 1310 MPa [48]. Peak aging (H900) samples from square tube 2-7, without solution treatment (CA), resulted in tensile strengths lower than the expected range from wrought samples. However, when solution treating (CA) was conducted and followed by peak aging (H900), square tube 2-7 resulted in a tensile strength higher than CA+H900 wrought 17-4PH stainless steel and most other AM processes [28], [52], [93]. The sample from square tube 2-7 with CA+H900 resulted in a tensile strength of 1405 MPa and a 12.2 % reduction in area. It was noted that the sample from square tube 2-7 resulted in higher tensile strengths than expected. The tensile fracture mechanisms are critical in understanding the failure mode and should be further studied as is discussed in Appendix J. Moreover, due to the miniature size of the tensile samples, no extensometer was used during tensile testing. The displacement that occurs on the grips of the samples are equated to the extension of the samples when no extensometer is used, and strain is calculated based on the machine's collected extension. The obtained Young's Modulus for all four samples was one order of magnitude lower than what it

should be, likely due to an error with the strain results. No conclusions were made on the source of the error, and the section is further discussed in Appendix J. However, the recorded tensile measurements are independent of strain and are equitable to those of conventionally manufactured 17-4PH stainless steel.

*Table 6-7 Ultimate tensile strength values for four different heat treatment conditions on PTA-AM samples built with two heat inputs. Condition A (CA): 1040°C for 0.5 hrs followed by argon cooling. Peak aging (H900): 480°C for 1 hr followed by air cooling.*

| Condition | Tensile Strength (MPa) |
|-----------|------------------------|
| Non-HT | 953 |
| Condition A | 1078 |
| H900 | 1267 |
| Condition A+H900 | 1403 |

A matrix of 5x3 hardness points was collected on the surface of all four heat treated conditions of samples from square tubes 2-7 and 2-8. From the results, there is a clear overlap between the standard deviations of non-heat treated and Condition A samples, for both samples from square tubes 2-7 and 2-8. According to the hardness results, it is hypothesized that some copper particles prematurely precipitate in the as-deposited, non-heat treated condition giving the as-deposited samples a comparable hardness to the more homogeneous Condition A samples [38]. The overlap between H900 and CA+H900 conditions for both samples from square tubes 2-7 and 2-8 can be interpreted with the same rationale. It can be assumed that prematurely precipitated particles from the as-deposited samples continue to fully mature in the H900 samples, along with newly precipitated particles, giving the H900 samples comparable hardness results to the more homogeneous CA+H900 samples. Results from H900 and CA+H900 samples range around 450-500 Hv; average hardness of wrought CA+H900 17-4PH stainless steel is around 450 Hv, marked by a black line in [46], [47]. The higher average hardness for all conditions in *Figure 6-21*, as compared with conventionally manufactured 17-4PH stainless steel, may be attributed to the resulting fast cooling rate of an AM process. Similarly, higher hardness results than the average for wrought CA+H900 builds of 17-4PH stainless steel were reported from other AM process [28], [42], [47]. In the case of square tubes 2-7 and 2-8, the on-average higher hardness of square tube

2-7 in all four heating conditions can be attributed to its overall lower excess heat in the system (*Figure 6-18*) and its lower heat input. As previously discussed, lower excess heat in the system results in higher tensile results and hardness [88], [89]. The higher hardness in the non-solutionized conditions (in Non-HT and H900 conditions) as compared with the solutionized conditions (CA and CA+H900) can be attributed to the presence of more copper precipitates in a heterogeneous matrix.

It can be concluded that, even though CA+H900 did not deliver higher hardness results than H900, the more homogeneous microstructure achieved by solutionizing and the associated higher tensile results in the CA+H900 make it the recommended heat treatment, as given by *Table 6-7*.
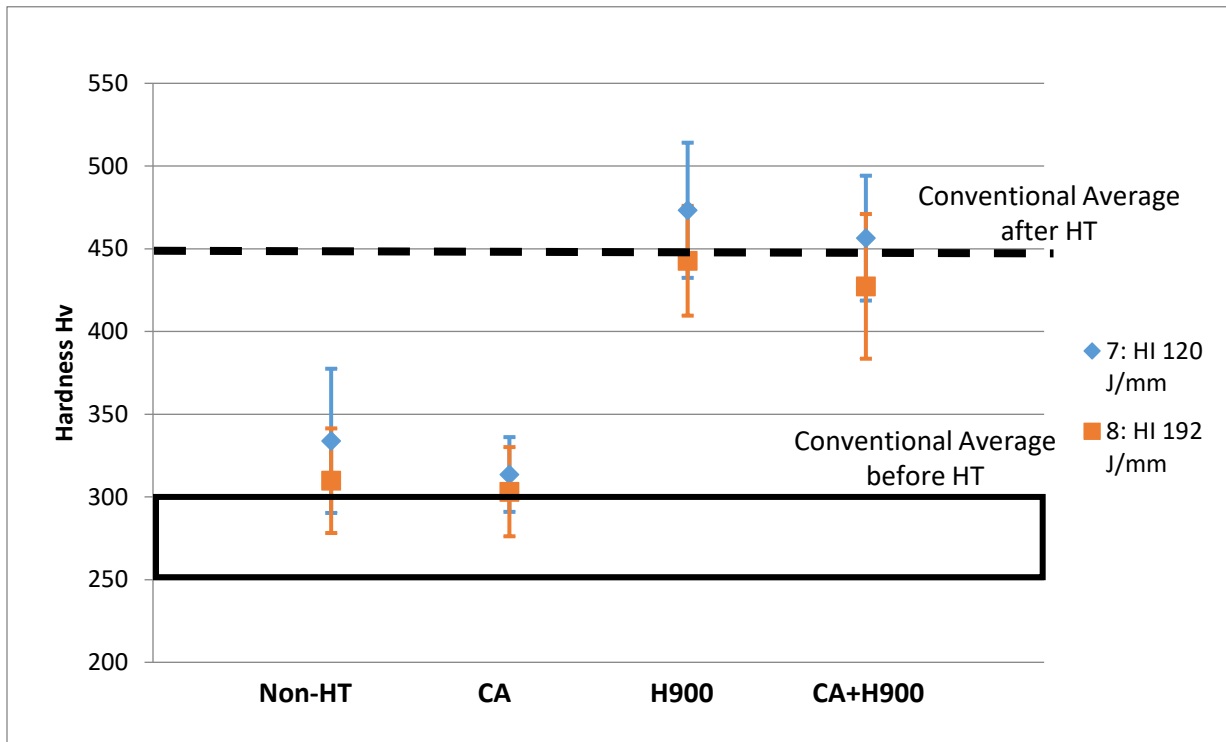


*Figure 6-21 Shows the average hardness from each of the eight samples along with their associated standard deviations; the average hardness of peak aged wrought 17-4PH stainless steel is marked by a black dotted line and by a black box before peak ageing.*

### 6.3.2.4 Resulting Matrix and Microstructure

According to literature, the matrix of 17-4PH stainless steel is well defined when manufactured with conventional processes, as opposed to the variable microstructure developed by the different

AM processes. The matrix of the conventionally manufactured as-received microstructure is identified as martensite with some delta ferrite. After solution treatment the matrix transforms into lath martensite and after peak aging the matrix transforms into tempered martensite and delta ferrite with some retained austenite [47]. The phases and stages of transformation during AM processes are not as clearly agreed upon in literature. It has been found that slight changes in the chemical composition of 17-4PH stainless steel, varying heat inputs from the different AM processes and chemical composition of the gases used for shielding can all play a pivotal role in the resulting phases in the as-deposited stage [28], [47], [52], [54]. The aforementioned differences typically result in varying volume fractions of an austenite phase during the as-deposited stage with AM processes. It has been reported that using a nitrogen shielding atmosphere results in 50-75% increase in the austenite volume fraction as compared with only 8% with pure argon as a shielding gas [52].

Earlier results from 17-4PH stainless using the PTA-AM system have shown a full martensitic matrix, with delta ferrite, but no traces of any austenite before or after heat treatments. However, based on research of AM 17-4PH stainless steel, austenite can be present in the as-deposited phase as a factor of initial powder chemical composition or shielding gas chemical composition [28], [47], [52]. For this reason, it was hypothesized that some austenite may be present in the as-deposited stage, but it transforms into complete martensite due to stress induced phase transformations during the polishing process and before the XRD analysis is conducted. To verify whether this phase transformation occurs, two samples were studied in the as-deposited stage. Both samples underwent the same polishing process, but one sample had its surface milled using a focused ion beam (FIB) milling process to remove any strain transformation effect during the polishing process. Surfaces were milled about 5 µm deep. Images from the FIB process are given in Appendix K. No information was found on the expected depth of a transformed surface; 5 µm was decided upon based on the machine's capabilities. Both samples were analyzed under an EBSD process to identify the microstructures of both processes. However, results consistently indicated the presence of only BCC (martensite and ferrite) microstructures and no FCC (austenite) in both samples, as shown in Figure 6-22. *Figure 6-22* shows EBSD results that confirm that no BCT (martensite) or FCC (austenite) structures are present in the microstructure of all the samples used in the above experiments. However, earlier results explained how martensite can be approximated to a BCC structure, instead of a BCT structure, because of the very low carbon

content in 17-4PH stainless steel [13]. This concludes that all samples from the first and second DOEs have BCC structures (martensite with ferrite). Conclusions from the EBSD microstructure results portray the comparable microstructure of 17-4PH stainless steel printed using the PTA-AM system to results from wrought 17-4PH stainless steel, where all heating conditions result in a martensitic matrix [47].
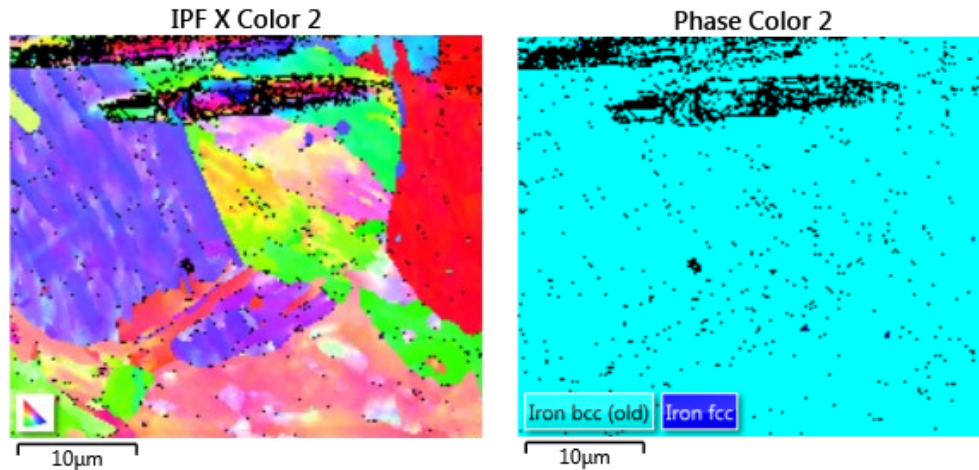


*Figure 6-22 EBSD images of the milled surface showing only a BCC microstructure.*

## 6.4 Conclusions

The number of available process parameters of the PTA-AM system allowed for a significant variation between the build quality of AM samples. Taguchi DOE was used to identify which process parameters were more influential to build repeatable and reproducible coupons on the PTA-AM system using 17-4PH stainless steel. Build height, wall thickness, hardness, maximum wall deviation and porosity of each experiment were measured. Powder feed rate, current and table speed were selected as the process parameters causing the most variability on the walls from the first DOE. Layer thickness was found to be a function of the different process parameters. Increasing it from 500 µm to 750 µm for the second DOE (based on powder feed rate and heat input), still required manual adjustments to try and maintain a constant voltage. The need for manual adjustments in the second DOE indicates that layer thickness should be variable for different combinations of process parameters.

 Keeping five constant parameters, and varying only the three most influential process parameters, has proven sufficient in building basic geometries, such as circular and square cross-sectioned

tubes. The selection of range of process parameters in the second DOE resulted in complete builds; however, the different combinations resulted in different properties for each build. Parameters for square tubes 2-7 and 2-8 proved to have the best combination of *Heat* and *Length Ratio*s. This resulted in them having the least excess heat with the largest layer heights, indicating minimal powder loss in comparison with the other square tubes.

Hardness measurements from the circular and square cross-sectioned tubes fell within the upper limit of expected hardness of 17-4PH stainless steel manufactured with conventional methods. The higher hardness results were attributed to early precipitation of copper in the as-deposited stage. Moreover, the larger number of the collected hardness data points are more representative of the overall mechanical properties of the square tubes, as compared with the tensile results. The tensile results correctly indicate the average tensile strength of samples produced using the PTA-AM system; however, more data should be collected to conclusively differentiate between the resulting tensile strengths from each heat treatment. Height variations between circular and square cross-sectioned tubes printed using the same process parameters were evident. It was concluded that the geometry of square tubes leads to more powder losses due to the abrupt direction change for the square tube during the printing process. The inverse relationship between part thickness and layer height notes results in higher additional excess heat absorbed, as noted in the square tube shape when compared to the circular tubes. However, a comparison between the percentage of powder lost versus heat input in both geometries showed that more powder is lost when printing square tubes.

Solution treatment was found to play a vital role in achieving microstructural homogeneity. Samples that were solution treated and peak aged displayed ultimate tensile results comparable to, or higher than, those manufactured with conventional processes and other AM processes. It was also evident that process parameters influence the resulting tensile strengths in different heating conditions.

# 7 Conclusions and Future work

## 7.1 Conclusions

The main objective of this thesis was to identify the operational process parameters that were needed to build samples 17-4PH stainless steel shapes on the PTA-AM system with mechanical properties higher or equivalent to those conventionally manufactured and with minimum defects. The research groups at Innotech Alberta and the ADAMS and AMPL groups at the UofA are amongst a select number of groups working with the PTA machine as an AM process. For that reason, no literature review was found on the processing of 17-4PH stainless steel using the PTA-AM system. The flow of the work was divided into three major sections. The first section was to conduct initial experiments to understand the basic operational parameters which would yield deposition of 17-4PH stainless steel using the PTA-AM system. The second section was to understand and eliminate the sources of defects in the printed samples. The final section was to identify the range of process parameters that could build basic 17-4PH stainless steel AM shapes on the PTA-AM system and characterize and compare the mechanical properties to those found in literature. The major findings and conclusions are as follows:

1) Replacing argon with nitrogen in the powder gas port, while keeping argon in the shield and center gases, in the PTA-AM system rapidly increased the porosity in the printed 17-4PH stainless steel AM part. Literature review had shown that using nitrogen gas in other AM processes had reduced porosity in 17-4PH stainless steel; however, none of the processes were with a PTA-AM system [11], [12], [56]. Moreover, the nitrogen gas in the PTA-AM system was supplied as a powder gas and not as a shield gas (restricted by the capabilities of the machine). It was concluded that the entrapment of nitrogen gas in the melted weld pool was the cause of excess nitrogen porosity.

2) Two major types of voids were found in the early printing stages of 17-4PH stainless steel: porosity and oxide layers. The reasons of how they were formed, and the work done to eliminate them is as follows:

   a) Oxide layer: An obvious segregation between the layers of the AM coupon was apparent in the initial experiments. At this stage of experiments, the gas used for

the center, shield and powder gases was pure argon. The chemical composition of this layer of segregation was found to be $Cr_2O_3$, a common oxide layer found in stainless steel that forms by the interaction of atmospheric oxygen with the stainless steel's chromium. The presence of this layer in the interlayers of an AM part creates inhomogeneity in the part's mechanical properties and microstructure. To prevent its formation, a shielding hood was designed to ensure a continuous flow of argon gas over the entirety of the AM part as it is being printed and, thus, preventing the interaction of the oxygen and chromium.

b) Porosity: Even though the oxide layer reduced the average percentage of voids from around 18% to 10%, any porosity over 1% was unacceptable. From literature review, it was found that insufficient heat input during the printing process may be a source of porosity [10]. If the heat is not high enough to melt all the powders, porosity may form around the unmelted powders during the printing process. Increasing the heat input by 15% was found to reduce the porosity down to around 2%.

If the initial powders used for the printing process contained internal porosity, it was very likely for the porosity to remain inside the final AM build. With optimum process parameters and the use of the shielding hood, a total of void content of 2v.% was found with powders from Supplier A, which dropped down to 0.4v.% with powders from Supplier B. Builds printing using Supplier B and the hydrogen gas mix resulted in less than 1v.% porosity content.

3) The effect of heat treatment on hardness and microstructure was evaluated. Hardness results of coupons before and after heat treatment aligned with, or exceeded, the average hardness values of 17-4PH stainless steel from literature before and after heat treatment, respectively, verifying the formation of the copper precipitates. This was confirmed by the EDX results obtained from TEM imaging which showed copper precipitates and niobium carbide precipitates. XRD results showed that there were no changes in the matrix before and after heat treatment.

4) Using a 5%H2+95%Ar gas mix was found to have the same effect of eliminating the oxide layers as using a shielding hood. The use of the hydrogen gas mix was found to be more efficient in its consumption of gas and powder as compared to the shielding hood.

5) Influential process parameters were identified using Taguchi DOEs.

   a) Taguchi's L'18 DOE identified the optimal values of the parameters that are to be kept constant: offset torch distance (7 mm), center gas (2 lpm), shield gas (13 lpm), powder gas (2 lpm) and nozzle angle (45°). Powder feed rate, current and table speed are the variable parameters.

   b) The ideal range of parameters was identified when printing complete circular and square cross-sectioned tubes by varying only powder feed rate, current and table speed, while keeping all other parameters constant.

6) Hardness results were consistently within the upper limit of the expected hardness range of 17-4PH stainless steel manufactured with conventional techniques. The hardness value before heat treatment (as deposited) ranged between 250-300 Hv and after heat treatment averaged around 450 Hv, regardless of variations in processing parameters. It was deduced that self heat treatment can occur during the printing process [28], [38], allowing for the early precipitation of some copper particles, explaining the higher range of hardness results.

7) Hardness and tensile values from the circular and square cross-sectioned tubes, before and after heat treatment, confirm that printing 17-4PH stainless steel with the PTA-AM system resulted in comparable or better values than found from conventional manufacturing. It was found that solution treatment is a crucial post processing heat treatment that must be conducted prior peak aging. Solution treatment results in a more homogeneous microstructure and ensures the dissolution of all precipitates in the solid solution. Tensile results from solution treated and then peak aged samples showed the best results, which were comparable to or higher than results from conventional manufacturing processes.

8) Since not enough information is known about the dissolution rate of copper after the solution treatment process, it is recommended that a faster cooling rate be conducted and

mechanical properties compared and analyzed. Water quenching would be recommended as the cooling method after the solution treatment.

9) Tensile and hardness results collected from square tube 2-7 indicate that more tensile data should have been conducted to give more conclusive results. The discrepancy between the non-HT and the CA conditions of square tube 2-7 can be attributed to internal defects in the sample that had a more prominent effect due to the miniature size of the tensile specimen. The larger number of hardness data points collected give a more accurate representation of the expected results of the different heat treatment conditions.

10) Earlier XRD results showed only BCC microstructures in the before and after heat treated stages. However, it was hypothesized that polishing may induce phase transformations from austenite to martensite in the as-deposited stage. FIB milling was conducted on the surface of one sample to remove layers of the material that may have undergone phase transformation, and EBSD was conducted on both milled and non-milled surfaces. Results showed no presence in austenite in either case.

11) Square tube 2-7 had the following process parameters: PFR: 35 g/min, current: 50 A, table speed: 800 mm/min, shield gas: 13 lpm, current and powder gas: 2 lpm, nozzle angle: 45º and offset 7 mm. Square tube 2-7 showed optimal results in terms of *Heat Ratio* to *Length Ratio*, hardness results within the upper range of expected hardness of 17-4PH stainless steel before and after heat treatment and good surface finish. More importantly, square tube 2-7 had mechanical properties that surpassed those of conventionally manufactured 17-4PH stainless steel in the CA+H900 stage. Therefore, the process parameters of square tube 2-7 are recommended when printing 17-4PH stainless steel on the PTA-AM system.

## 7.2 Future work

The main objective behind this thesis was to identify the working process parameters on the PTA-AM system that can print basic 17-4PH stainless steel AM parts with minimum defects and superior mechanical properties. The several chapters of this thesis show the successful delivery of that objective; however, more work can follow to further enhance the quality of the printed parts. The following two points are recommended for future work.

### 7.1.1   Cavity

Cavity was found in some of the printed samples from the first DOE. Several experiments were done to understand how it was formed and why it stopped appearing in the later DOE, however, no conclusive results were made. It is known, though, that cavity can be reproduced by using an identical set of printing process parameters or by printing a part using the minimum peak points, as is explained in Appendix C. The cavity's reproducibility entails that it was not a one-time error that cannot reappear. Further experiments should be done to identify which process parameter (or combination of process parameters) led to the production of cavity and how to ensure it does not reappear in future builds.

### 7.1.2   Process Parameters

Even though basic parts were printed using the final selected process parameters (powder feed rate, current and table speed), further optimization can be done. The final sets of circular and square cross-sectioned tubes do not possess a smooth surface finish. The parts have a very rough surface finish with an inconsistency in layer to layer overlap. This can be attributed to the semiautomatic change of the torch's position during the printing process. Even though the torch is supposed to remain stationary when the 3D table is connected, sometimes the deposited part is building up faster than the table is moving down, allowing the torch to get too close to the deposition. This requires a manual intervention to slightly raise the torch up to ensure a constant offset distance is maintained between the deposit and the torch. The manual change of torch position is not always accurate and can cause abrupt changes to the heat input delivered during the printing process; the change in torch position is directly proportional to the voltage. Hence, the movement of the torch should be fully automated to ensure the smoothest transition between layers. Alternatively, the

selected part thickness in the G-code should be altered depending on the powder feed rate for each part. A build with a higher powder feed rate would need a larger layer thickness in the G-code, and vice versa. Another reason for the roughness of the surfaces can be attributed to nozzle angle. By having only two powder ports, the effect of the powder deposition angle is greatly highlighted. Possibly having more powder ports can ensure a more even distribution of powders during the printing process and eliminate the build up of unmelted powder on the interior/exterior of the printed samples.

### 7.1.3    Tensile Fracture Surface Analysis and Young's Modulus

Tensile samples were obtained from four different samples in the second DOE. Some of the fractures had cup and cone fractures while others had brittle fractures (images are in Appendix J). A further analysis on the methods of fracture in each of the tensile samples, and a correlation to tensile results, is required. Moreover, more tensile specimens should be obtained for each set of process parameters to give more conclusive results.

Additionally, Young's Modulus results are off by a factor of 10 for all four samples in the different conditions. Calculations were thoroughly reviewed but no error was found in them. Literature shows that miniature samples can result in minor differences in their results, as compared with full sized tensile samples; however, no results were remotely close to the discrepancies found in this thesis' Young;s Modulus.

# Bibliography

[1]     S. Park and D. W. Rosen, "Quantifying effects of material extrusion additive manufacturing process on mechanical properties of lattice structures using as-fabricated voxel modeling," *Addit. Manuf.*, vol. 12, pp. 265–273, 2016.

[2]     M. Molitch-Hou, "Overview of additive manufacturing process," in *Additive Manufacturing*, 1st ed., Elsevier Inc., 2018, pp. 1–38.

[3]     W. E. Frazier, "Metal additive manufacturing: A review," *J. Mater. Eng. Perform.*, vol. 23, pp. 1917–1928, 2014.

[4]     A. Zikin, S. Ilo, P. Kulu, I. Hussainova, C. Katsich, and E. Badisch, "Plasma transferred arc (PTA) hardfacing of recycled hardmetal reinforced nickel-matrix surface composites," *Medziagotyra*, vol. 18, no. 1, pp. 12–17, 2012.

[5]     R. Liu, M. X. Yao, P. C. Patnaik, and X. J. Wu, "An improved wear-resistant PTA hardfacing: VWC/stellite 21," *J. Compos. Mater.*, vol. 40, no. 24, pp. 2203–2215, 2006.

[6]     S. Babu, V. Balasubramanian, G. Madhusudhan Reddy, and T. S. Balasubramanian, "Improving the ballistic immunity of armour steel weldments by plasma transferred arc (PTA) hardfacing," *Mater. Des.*, vol. 31, no. 5, pp. 2664–2669, 2010.

[7]     J. Nowacki, "Weldability of 17-4 PH stainless steel in centrifugal compressor impeller applications," in *Journal of Materials Processing Technology*, 2004, vol. 157–158, pp. 578–583.

[8]     M. R. Tavakoli Shoushtari, M. H. Moayed, and A. Davoodi, "Post-weld heat treatment influence on galvanic corrosion of GTAW of 17-4PH stainless steel in 3·5%NaCl," *Corros. Eng. Sci. Technol.*, vol. 46, no. 4, pp. 415–424, 2011.

[9]     M. Murayama, Y. Katayama, and K. Hono, "Microstructural evolution in a 17-4 PH stainless steel after aging at 400 °C," *Metall. Mater. Trans. A Phys. Metall. Mater. Sci.*, vol. 30, no. 2, pp. 345–353, 1999.

[10]    H. Fayazfar *et al.*, "A critical review of powder-based additive manufacturing of ferrous

alloys: Process parameters, microstructure and mechanical properties," *Mater. Des.*, vol. 144, no. Apri;, pp. 98–128, 2018.

[11]   J. W. Elmer, J. Vaja, H. D. Carlton, and R. Pong, "The effect of Ar and N2 shielding gas on laser weld porosity in steel, stainless steels, and nickel," *Weld. J.*, vol. 94, no. 10, pp. 313s-325s, 2015.

[12]   W. Liu *et al.*, "Hybrid Laser-arc Welding of 17-4 PH Martensitic Stainless Steel," *Lasers Manuf. Mater. Process.*, vol. 2, no. 2, pp. 74–90, 2015.

[13]   S. N. El Moghazi, T. Wolfe, D. G. Ivey, and H. Henein, "Plasma transfer arc additive manufacturing of 17-4 PH : assessment of defects," *Int. J. Adv. Manuf. Technol.*, vol. 108, pp. 2301–2313, 2020.

[14]   E. A. Alberti, B. M. P. Bueno, and A. S. C. M. D'Oliveira, "Additive manufacturing using plasma transferred arc," *Int. J. Adv. Manuf. Technol.*, vol. 83, pp. 1861–1871, 2016.

[15]   R. Paul, S. Anand, and F. Gerner, "Effect of Thermal Deformation on Part Errors in Metal Powder Based Additive Manufacturing Processes," *J. Manuf. Sci. Eng.*, vol. 136, no. 3, p. 031009, 2014.

[16]   T. D. Ngo, A. Kashani, G. Imbalzano, K. T. Q. Nguyen, and D. Hui, "Additive manufacturing (3D printing): A review of materials, methods, applications and challenges," *Composites Part B: Engineering*, vol. 143. pp. 172–196, 2018.

[17]   ASTM International, "F2792-12a - Standard Terminology for Additive Manufacturing Technologies," *Rapid Manuf. Assoc.*, pp. 10–12, 2013.

[18]   P. K. Gokuldoss, S. Kolla, and J. Eckert, "Additive manufacturing processes: Selective laser melting, electron beam melting and binder jetting-selection guidelines," *Materials*, vol. 10, no. 6. pp. 1–12, 2017.

[19]   X. Xu, S. Meteyer, N. Perry, and Y. F. Zhao, "Energy consumption model of Binder-jetting additive manufacturing processes," *Int. J. Prod. Res.*, vol. 53, no. 23, pp. 7005–7015, 2015.

[20]   F. Peng, B. D. Vogt, and M. Cakmak, "Complex fl ow and temperature history during

melt extrusion in material extrusion additive manufacturing," *Addit. Manuf.*, vol. 22, pp. 197–206, 2018.

[21] Y. Ling, C. Wang, S. Leong, V. Dikshit, W. Yee, and J. Wei, "Material jetting additive manufacturing : An experimental study using designed metrological benchmarks," *Precis. Eng.*, vol. 50, pp. 275–285, 2017.

[22] P. M. Bhatt, A. M. Kabir, M. Peralta, H. A. Bruck, and S. K. Gupta, "A robotic cell for performing sheet lamination-based additive manufacturing," *Addit. Manuf.*, vol. 27, pp. 278–289, 2019.

[23] Y. Zhang, W. Jarosinski, Y. G. Jung, and J. Zhang, *Additive manufacturing processes and equipment*. Elsevier Inc., 2018.

[24] R. Goodridge and S. Ziegelmeier, "7 - Powder bed fusion of polymers," in *Laser Additive Manufacturing*, Elsevier Ltd, 2017, pp. 181–204.

[25] Y. Zhang *et al.*, "Additive Manufacturing of Metallic Materials : A Review," *J. Mater. Eng. Perform.*, vol. 27, pp. 1–13, 2018.

[26] V. Bhavar, P. Kattire, V. Patil, S. Khot, K. Gujar, and R. Singh, "A review on powder bed fusion technology of metal additive manufacturing," in *4th International conference and exhibition on additive manufacturing technologies*, 2014.

[27] K. Taminger and R. Hafley, "Electron beam freeform fabrication: a rapid metal deposition process," in *Proceedings of the 3rd Annual Automotive Composites Conference*, 2003, pp. 1–6.

[28] A. Caballero, J. Ding, S. Ganguly, and S. Williams, "Wire + Arc Additive Manufacture of 17-4 PH stainless steel: Effect of different processing conditions on microstructure, hardness, and tensile strength," *J. Mater. Process. Technol.*, vol. 268, pp. 54–62, 2019.

[29] G. Fisher and T. Wolfe, "Protective Overlays and COarings Used in Oil Sands," in *Thermal Spray Technology*, 2013, pp. 312–317.

[30] M. F. Buchely, J. C. Gutierrez, L. M. Le, and A. Toro, "The effect of microstructure on abrasive wear of hardfacing alloys," vol. 259, pp. 52–61, 2005.

[31]    V. V. Diaz, J. C. Dutra, and A. S. C. M. D'Oliveira, "Hardfacing by plasma transfer arc process," *Weld. Int.*, vol. 26, no. 2, pp. 87–95, 2012.

[32]    L. Wang, P. Pratt, S. Felicelli, H. Kadiri, and P. Wang, "Experimental Analysis of Porosity Formation in Laser-Assisted Powder Deposition Process," *TMS (The Miner. Met. Mater. Soc.*, vol. 1, pp. 389–396, 2009.

[33]    A. Sola and A. Nouri, "Microstructural porosity in additive manufacturing: The formation and detection of pores in metal parts fabricated by powder bed fusion," *J. Adv. Manuf. Process.*, vol. 1, no. 3, 2019.

[34]    B. Graf, A. Marko, T. Petrat, A. Gumenyuk, and M. Rethmeier, "3D laser metal deposition : process steps for additive manufacturing," *Weld. World*, vol. 62, no. 4, pp. 877–883, 2018.

[35]    C. Li, Z. Y. Liu, X. Y. Fang, and Y. B. Guo, "Residual Stress in Metal Additive Manufacturing," in *Procedia CIRP*, 2018, vol. 71, pp. 348–353.

[36]    R. Li, J. Liu, Y. Shi, L. Wang, and W. Jiang, "Balling behavior of stainless steel and nickel powder during selective laser melting process," *Int. J. Adv. Manuf. Technol.*, vol. 59, no. April, pp. 1025–1035, 2012.

[37]    M. Król and T. Taski, "Surface quality research for selective laser melting of TI-6AL-4V alloy," *Arch. Metall. Mater.*, vol. 61, no. 3, pp. 945–950, 2016.

[38]    J. Xiong, Y. Lei, and R. Li, "Finite element analysis and experimental validation of thermal behavior for thin-walled parts in GMAW-based additive manufacturing with various substrate preheating temperatures," *Appl. Therm. Eng.*, vol. 126, pp. 43–52, 2017.

[39]    ASTM-A564, "Standard Specification for Hot-Rolled and Cold-Finished Age-Hardening Stainless Steel Bars and Shapes," *ASTM Int.*, pp. 1–7, 2010.

[40]    U. K. Viswanathan, S. Banerjee, and R. Krishnan, "Effects of aging on the microstructure of 17-4 PH stainless steel," *Mater. Sci. Eng.*, vol. 104, pp. 181–189, 1988.

[41]    A. M. A. Mohamed and F. H. Samuel, "A Review on the Heat Treatment of Al-Si-Cu/Mg Casting Alloys," in *Heat Treatment - Conventional and Novel Applications*, 2012, pp. 55–

72.

[42]   G. Yeli, M. A. Auger, K. Wilford, G. D. W. Smith, P. A. J. Bagot, and M. P. Moody, "Sequential nucleation of phases in a 17-4PH steel: Microstructural characterisation and mechanical properties," *Acta Mater.*, vol. 125, pp. 38–49, 2017.

[43]   D. L. Olson, "Prediction of Austenitic Weld Metal Microstructure and Properties With advent of new stainless steels, a wider range of alloys must be considered in predicting ferrite," *Weld. Res. SUPPLEMEN*, vol. 64, no. 10, pp. 181–189, 1985.

[44]   W. D. Yoo, J. H. Lee, K. T. Youn, and Y. M. Rhyim, "Study on the microstructure and mechanical properties of 17-4PH stainless steel depending on heat treatment and aging time," *Solid State Phenom.*, vol. 118, pp. 15–20, 2006.

[45]   Q. Luo, "A New XRD Method to Quantify Plate and Lath Martensites of Hardened Medium-Carbon Steel," *J. Mater. Eng. Perform.*, vol. 25, no. 6, pp. 2170–2179, 2016.

[46]   C. N. Hsiao, C. S. Chiou, and J. R. Yang, "Aging reactions in a 17-4 PH stainless steel," *Mater. Chem. Phys.*, vol. 74, no. 2, pp. 134–142, 2002.

[47]   Y. Sun, R. J. Hebert, and M. Aindow, "Effect of heat treatments on microstructural evolution of additively manufactured and wrought 17-4PH stainless steel," *Mater. Des.*, vol. 156, pp. 429–440, 2018.

[48]   P. D. Nezhadfar, R. Shrestha, N. Phan, and N. Shamsaei, "Fatigue behavior of additively manufactured 17-4 PH stainless steel: Synergistic effects of surface roughness and heat treatment," *Int. J. Fatigue*, vol. 124, pp. 188–204, 2019.

[49]   L. Xiao, Z. Fan, Z. Jinxiu, Z. Mingxing, K. Mokuang, and G. Zhenqi, "Lattice-parameter variation with carbon content of martensite. I. X-ray-diffraction experimental study," *Phys. Rev. B*, vol. 52, no. 14, pp. 9970–9978, 1995.

[50]   R. Schroeder, G. Hammes, C. Binder, and A. N. Klein, "Plasma debinding and sintering of metal injection moulded 17-4PH stainless steel," *Mater. Res.*, vol. 14, no. 4, pp. 564–568, 2011.

[51]   Y. Lu, H. Yu, and R. D. Sisson, "The effect of carbon content on the c/a ratio of as-

quenched martensite in Fe-C alloys," *Mater. Sci. Eng. A*, vol. 700, pp. 592–597, 2017.

[52] H. K. Rafi, D. Pal, N. Patil, T. L. Starr, and B. E. Stucker, "Microstructure and Mechanical Behavior of 17-4 Precipitation Hardenable Steel Processed by Selective Laser Melting," *J. Mater. Eng. Perform.*, vol. 23, no. 12, pp. 4421–4428, 2014.

[53] N. Suutala, "Effect of solidification conditions on the solidification mode in austenitic stainless steels," *Metall. Trans. A*, vol. 14, no. 1, pp. 191–197, 1983.

[54] M. W. Wu, Z. K. Huang, C. F. Tseng, and K. S. Hwang, "Microstructures, mechanical properties, and fracture behaviors of metal-injection molded 17-4PH stainless steel," *Met. Mater. Int.*, vol. 21, no. 3, pp. 531–537, 2015.

[55] D. F. Susan, T. B. Crenshaw, and J. S. Gearhart, "The Effects of Casting Porosity on the Tensile Behavior of Investment Cast 17-4PH Stainless Steel," *J. Mater. Eng. Perform.*, vol. 24, no. 8, pp. 2917–2924, 2015.

[56] P. D. Nezhadfar, M. Masoomi, S. M. Thompson, N. Phan, and N. Shamsaei, "Mechanical Properties of 17-4 PH Stainless Steel Additively Manufactured under Ar and N2 Shielding Gas," *Solid Free. Fabr. Symp.*, no. December, pp. 1301–1310, 2017.

[57] F. C. Campbell, *Inspection of Metals: Understanding the Basics*. ASM International, 2013.

[58] ASTM E8, "ASTM E8/E8M standard test methods for tension testing of metallic materials 1," *Annu. B. ASTM Stand. 4*, pp. 1–27, 2010.

[59] A. Kolhatkar, V. Karthik, G. M. S. K. Chaitanya, A. Kumar, and D. Ramchandran, "Development and Validation of a Miniature Tensile Specimen for Determination of Mechanical Properties," *J. Test. Eval.*, vol. 47, no. 5, pp. 3417–3431, 2019.

[60] A. Matsunawa, M. Mizutani, S. Katayama, and N. Seto, "Porosity formation mechanism and its prevention in laser welding," *Weld. Int.*, vol. 17, no. 6, pp. 431–437, 2003.

[61] P. Kah and J. Martikainen, "Influence of shielding gases in the welding of metals," *Int. J. Adv. Manuf. Technol.*, vol. 64, no. 9–12, pp. 1411–1421, 2013.

[62] I. Bitharas, N. A. McPherson, W. McGhie, D. Roy, and A. J. Moore, "Visualisation and

optimisation of shielding gas coverage during gas metal arc welding," *J. Mater. Process. Technol.*, vol. 255, pp. 451–462, 2018.

[63]    R. S. C. Paredes, S. C. Amico, and A. S. C. M. d'Oliveira, "The effect of roughness and pre-heating of the substrate on the morphology of aluminium coatings deposited by thermal spraying," *Surf. Coatings Technol.*, vol. 200, no. 9, pp. 3049–3055, 2006.

[64]    D. J. Corbin, A. R. Nassar, E. W. Reutzel, A. M. Beese, and P. Michaleris, "Effect of substrate thickness and preheating on the distortion of laser deposited ti-6al-4v," *J. Manuf. Sci. Eng. Trans. ASME*, vol. 140, no. 6, p. 9, 2018.

[65]    A. Zadi-Maad, R. Rohib, and A. Irawan, "Additive manufacturing for steels: A review," in *IOP Conference Series: Materials Science and Engineering*, 2017, vol. 285, pp. 012–028.

[66]    J. G. Mercado Rojas, T. Wolfe, B. A. Fleck, and A. J. Qureshi, "Plasma transferred arc additive manufacturing of Nickel metal matrix composites," *Manuf. Lett.*, vol. 18, pp. 31–34, Oct. 2018.

[67]    Z. Hu, H. Zhu, H. Zhang, and X. Zeng, "Experimental investigation on selective laser melting of 17-4PH stainless steel," *Opt. Laser Technol.*, vol. 87, pp. 17–25, 2017.

[68]    S. Isogawa, H. Yoshida, Y. Hosoi, and Y. Tozawa, "Improvement of the forgability of 17-4 precipitation hardening stainless steel by ausforming," *J. Mater. Process. Technol.*, vol. 74, no. 1–3, pp. 298–306, 1998.

[69]    B. Song *et al.*, "Differences in microstructure and properties between selective laser melting and traditional manufacturing for fabrication of metal parts: A review," *Front. Mech. Eng.*, vol. 10, pp. 111–125, 2015.

[70]    T. Liyanage, G. Fisher, and A. P. Gerlich, "Microstructures and abrasive wear performance of PTAW deposited Ni-WC overlays using different Ni-alloy chemistries," *Wear*, vol. 274–275, pp. 345–354, 2012.

[71]    T. Liyanage, G. Fisher, and A. P. Gerlich, "Influence of alloy chemistry on microstructure and properties in NiCrBSi overlay coatings deposited by plasma transferred arc welding (PTAW)," *Surf. Coatings Technol.*, vol. 205, no. 3, pp. 759–765, 2010.

[72] P. H. Huang and M. J. Guo, "A study on the investment casting of 17-4PH stainless steel helical impeller of centrifugal pump," *Mater. Res. Innov.*, vol. 19, pp. S977–S981, 2015.

[73] E. Toyserkani, A. Khajepour, S. F. Corbin, A. Khajepour, and S. F. Corbin, *Laser Cladding*. CRC Press, 2004.

[74] S. K. Yen and Y. Tsai, "Determination of the Critical Temperature for Forming a Chromium-Rich Oxide on AISI 430 Stainless Steel and Its Corrosion Resistance," *J. Electrochem. Soc.*, vol. 143, no. 8, pp. 2493–2497, 1996.

[75] R. Peter, I. Saric, I. K. Piltaver, I. J. Badovinac, and M. Petravic, "Oxide formation on chromium metal surfaces by low-energy oxygen implantation at room temperature," *Thin Solid Films*, vol. 636, pp. 225–231, 2017.

[76] J. A. Slotwinski and E. J. Garboczi, "Porosity of additive manufacturing parts for process monitoring," in *AIP Conference Proceedings*, 2014, vol. 1581, p. 1197.

[77] J. B. Ferguson, B. F. Schultz, A. D. Moghadam, and P. K. Rohatgi, "Semi-empirical model of deposit size and porosity in 420 stainless steel and 4140 steel using laser engineered net shaping," *J. Manuf. Process.*, vol. 19, pp. 163–170, 2015.

[78] W. Tillmann, C. Schaak, J. Nellesen, M. Schaper, M. E. Aydinöz, and K. P. Hoyer, "Hot isostatic pressing of IN718 components manufactured by selective laser melting," *Addit. Manuf.*, vol. 13, pp. 93–102, 2017.

[79] H. H. Alsalla, C. Smith, and L. Hao, "Effect of build orientation on the surface quality, microstructure and mechanical properties of selective laser melting 316L stainless steel," *Rapid Prototyp. J.*, vol. 24, no. 1, pp. 9–17, 2018.

[80] R. G. Davies, "Influence of martensite composition and content on the properties of dual phase steels," *Metall. Trans. A*, vol. 9, no. 5, pp. 671–679, 1978.

[81] M. Onsoien, R. Peters, D. L. Olson, and S. Liu, "Effect of hydrogen in an argon GTAW shielding gas: arc characteristics and bead morphology," *Weld. J. (Miami, Fla)*, vol. 74, no. 1, pp. 10–15, 1995.

[82] A. Durgutlu, "Experimental investigation of the effect of hydrogen in argon as a shielding

gas on TIG welding of austenitic stainless steel," *Mater. Des.*, vol. 25, no. 1, pp. 19–23, 2004.

[83]   J. Tusek and M. Suban, "Experimental research of the effect of hydrogen in argon as a shielding gas in arc welding of high-alloy stainless steel," *Int. J. Hydrogen Energy*, vol. 25, no. 4, pp. 369–376, 2000.

[84]   M. Mohamed, E. Alaa, Y. Aref, M. T. Scott, B. Linkan, and S. Nima, "Mechanical properties and microstructural characterization of selective laser melted 17-4 PH stainless steel," *Rapid Prototyp. J.*, vol. 23, no. 2, pp. 280–294, 2017.

[85]   A. Yadollahi, N. Shamsaei, S. M. Thompson, A. Elwany, and L. Bian, "Effects of building orientation and heat treatment on fatigue behavior of selective laser melted 17-4 PH stainless steel," *Int. J. Fatigue*, vol. 94, pp. 218–235, 2017.

[86]   R. K. Roy, "Formulas in Experiment Method," in *Primer on the Taguchi Method*, 2nd ed., New York: Van Nostrand Reinhold, 1990, pp. 49–127.

[87]   T. Lehmann *et al.*, "Concurrent geometry- and material-based process identification and optimization for robotic CMT-based wire arc additive manufacturing," *Mater. Des.*, vol. 194, p. 108841, 2020.

[88]   M. R. Bin Khiyon and S. M. Salleh, "Effect of heat-treatment on the hardness and mechanical properties of Boron Alloyed Steel," *MATEC Web Conf.*, vol. 90, 2016.

[89]   Z. Chen, P. Nash, and Y. Zhang, "Correlation of Cooling Rate, Microstructure and Hardness of S34MnV Steel," *Metall. Mater. Trans. B Process Metall. Mater. Process. Sci.*, vol. 50, no. 4, pp. 1718–1728, 2019.

[90]   C. E. Leshock, J. N. Kim, and Y. C. Shin, "Plasma enhanced machining of Inconel 718: Modeling of workpiece temperature with plasma heating and experimental results," *Int. J. Mach. Tools Manuf.*, vol. 41, no. 6, pp. 877–897, 2001.

[91]   S. D. Meredith, J. S. Zuback, J. S. Keist, and T. A. Palmer, "Impact of composition on the heat treatment response of additively manufactured 17–4 PH grade stainless steel," *Mater. Sci. Eng. A*, vol. 738, no. December, pp. 44–56, 2018.

[92]  C. Rowolt, B. Milkereit, A. Springer, C. Kreyenschulte, and O. Kessler, "Dissolution and precipitation of copper-rich phases during heating and cooling of precipitation-hardening steel X5CrNiCuNb16-4 (17-4 PH)," *J. Mater. Sci.*, vol. 55, no. 27, pp. 13244–13257, 2020.

[93]  S. KC, P. D. Nezhadfar, C. Phillips, M. S. Kennedy, N. Shamsaei, and R. L. Jackson, "Tribological behavior of 17–4 PH stainless steel fabricated by traditional manufacturing and laser-based additive manufacturing methods," *Wear*, vol. 440–441, pp. 1–8, 2019.

# 8  Appendices

## Appendix A: G-Codes for the 3D Table

This appendix displays the three different g-codes used for printing the walls, circular and square cross-sectioned tubes.

**Walls' G-Code:**

| | |
|---|---|
| #1=100 | (Initial position X) |
| #2=100 | (Initial position Y) |
| #3=0.2 | (Z-increase) |
| #4=600 | (Table speed) |
| #5=130 | (Wall length mm) |
| #6=20 | (Wall height mm) |
| #7=1 | (Counter) |

| | |
|---|---|
| (Main Program) | |
| G21 | (Units in mm) |
| M100 | (Brakes off) |
| G0 X#1 Y#2 Z0 | (Initial position) |
| G1 F#4 | (Set table speed) |
| M0 | (Wait, turn on the PTA) |
| M98 P1 L[#6/#3/2] | (Start sub-routine) |
| M0 | |
| G0 X80 Y30 Z250 | (Park position) |
| M101 | (Brakes on) |
| M2 | (End program) |

| | |
|---|---|
| (Wall sub-routine) | |
| O1 | (Sub-routine name) |

G1 X[#1+#5] Y#2 Z[#7*#3]   (Start line forward)

#7=[#7+1]

G1 X#1 Y#2 Z[#7*#3]          (Start line backward)

#7=[#7+1]

M99

**Circular Tubes' G-Code:**

| | |
|---|---|
| #1=100 | (Initial position X) |
| #2=100 | (Initial position Y) |
| #3=.75 | (Z increase) |
| #4=800 | (Table speed) |
| #5=25 | (Circle radius mm) |
| #6=50 | (Circular height) |
| #7=1 | (Counter @1) |

| | |
|---|---|
| (Main Program) | |
| G21 | (Units mm) |
| M100 | (Brakes off) |
| G0 X#1 Y#2 Z0 | (Go to initial position) |
| M101 | (Brakes on) |
| G01 F#4 | (Set table speed) |
| M0 | (Wait, turn on the PTA) |
| M100 | (Brakes off) |
| M110 P30 Q50 | (Set powder and current values) |
| G04 P17 | (Wait time before powder is deposited) |
| M115 | (Start recording data) |
| M98 P1 L[ROUND[#6/#3]] | (Start helix sub-routine) |
| | |
| M110 P0 Q0 | (End powder and current) |
| G0 Y77 | |
| G0 Y87 | |
| M115 | |
| M0 | (Wait, turn off the PTA) |
| G0 X80 Y30 Z250 | (Park position) |
| M101 | (Brakes on) |
| M2 | (End program) |

(Circular routine)

```
O1                                                   (Sub-routine name)
G03 R#5 X[#1-#5+.7071*#5] Y[#2+.7071*#5] Z[#3/8*#7]   (First eighth of the coil)
#7=[#7+1]                                             (Increase Z-displacement)
G03 R#5 X[#1-#5] Y[#2+#5] Z[#3/8*#7]                  (Second eighth of the coil)
#7=[#7+1]                                             (Increase Z-displacement)
G03 R#5 X[#1-#5-.7071*#5] Y[#2+.7071*#5] Z[#3/8*#7]   (Third eighth of the coil)
#7=[#7+1]                                             (Increase Z-displacement)
G03 R#5 X[#1-2*#5] Y[#2] Z[#3/8*#7]                   (Fourth eighth of the coil)
#7=[#7+1]                                             (Increase Z-displacement)
G03 R#5 X[#1-#5-.7071*#5] Y[#2-.7071*#5] Z[#3/8*#7]   (Fifth eighth of the coil)
#7=[#7+1]                                             (Increase Z-displacement)
G03 R#5 X[#1-#5] Y[#2-#5] Z[#3/8*#7]                  (Sixth eighth of the coil)
#7=[#7+1]                                             (Increase Z-displacement)
G03 R#5 X[#1-#5+.7071*#5] Y[#2-.7071*#5] Z[#3/8*#7]   (Seventh eighth of the coil)
#7=[#7+1]                                             (Increase Z-displacement)
G03 R#5 X[#1] Y[#2] Z[#3/8*#7]                        (Eighth eighth of the coil)
#7=[#7+1]                                             (Increase Z-displacement)
M99                                                  (End routine)
```

**Square Tubes' G-Code :**

| | |
|---|---|
| #1=100 | (Initial position X) |
| #2=100 | (Initial position Y) |
| #3=.75 | (Z-increase) |
| #4=700 | (Table speed) |
| #5=40 | (Rectangle length mm) |
| #6=40 | (Rectangle width mm) |
| #7=50 | (Rectangle Height mm) |
| #9=1 | (Counter@1) |

| | |
|---|---|
| (Main Program) | |
| G21 | (Units in mm) |
| M100 | (Brakes off) |
| G0 X#1 Y#2 Z0 | (Initial position) |
| M101 | (Brakes on) |
| G1 F#4 | (Set table speed) |
| M0 | (Wait, turn on the PTA) |
| M100 | (Brakes off) |
| M110 P25 Q50 | (Start powder and current) |
| G04 P17 | (Wait time for powder deposition) |
| M115 | (Start recording) |
| M98 P1 L[ROUND[[#7]/#3]] | (Start rectangle sub-routine) |
| | |
| M115 | (Stop recording) |
| M110 P0 Q0 | (Stop powder and current) |
| M0 | (Wait, turn off the PTA) |
| G0 X30 Y30 Z250 | (Park position) |
| M101 | (Brakes on) |
| M2 | (End program) |

(Rectangle sub-routine)

| | |
|---|---|
| O1 | (Routine name) |
| G1 X[#1+#5] Y#2 Z[#3/4*#9] | (First edge line X) |
| #9=[#9+1] | (Increase counter) |
| G1 X[#1+#5] Y[#2+#6] Z[#3/4*#9] | (First edge line Y) |
| #9=[#9+1] | (Increase counter) |
| G1 X[#1] Y[#2+#6] Z[#3/4*#9] | (Second edge line X) |
| #9=[#9+1] | (Increase counter) |
| G1 X#1 Y#2 Z[#3/4*#9] | (Second edge line Y) |
| #9=[#9+1] | (Increase counter) |
| M99 | (End routine) |

# Appendix B: Nitrogen Samples

This appendix gives more examples of how samples printed using nitrogen as a powder gas and argon as a shield gas and center gas looked like, and why using nitrogen was discontinued. Surface quality was very poor when nitrogen was used as a powder gas; moreover, large porosities were observed during the printing process and increasing amounts of powder spatter took place.



Figure B -1: Samples printed with different process parameters, using nitrogen as a powder gas, showing clear printing surface defects.

# Appendix C: Cavity

Cavity (Figure C-1) is a feature that appeared in some of the 18 printed walls. It was never an issue present in any of the printed parts from Chapter 5. The source of the cavity was not clearly understood. More importantly, it did not appear in any of the second DOE's build pieces. All of the circular and square cross-sectioned tubes were cut up in many smaller pieces each, and none of them showed any sign of cavity. To try and further understand if the cavity is reproduceable, the best- and worst-case scenarios, given from Minitab (Figure C-2), were used to build prototypes. The idea was to see if the best combination of process parameters, as recommended by Minitab, does indeed minimize the presence of cavity and if the worst combination of process parameters leads to more cavity.



Figure C -1: A cross-section from one of the walls showing cavity.
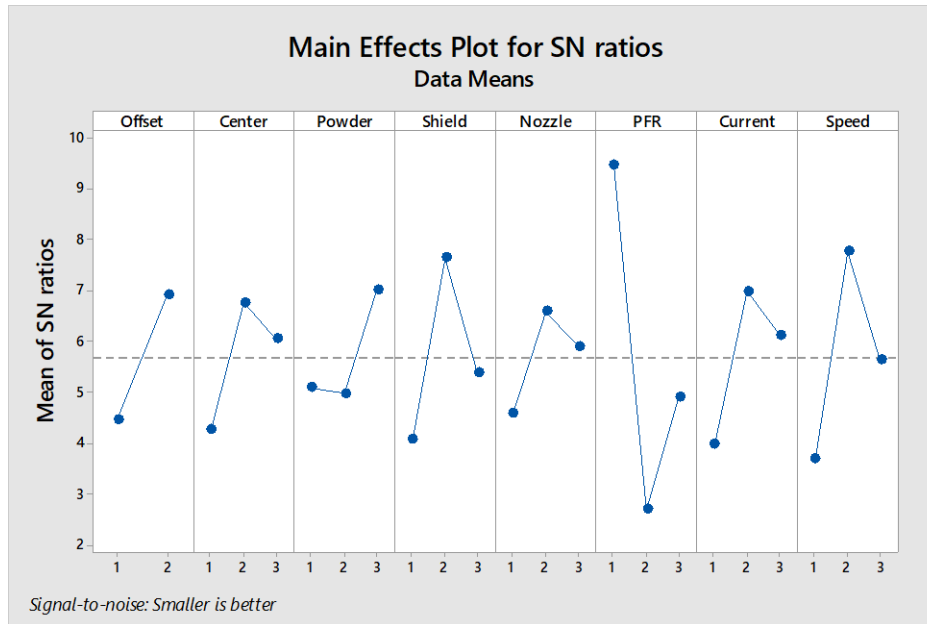
Figure C-2: Minitab plot of cavity's best- and worst-case combinations.

The maximum peak points and the minimum peak points were used to build a wall each. Two cross-sections were taken from each of the walls. Figure C-3 shows the cross-sections of the wall built with the maximum peak points (offset: 7 mm, center gas:1.5 lpm, powder gas: 2 lpm, shielding gas: 13 lpm, nozzle angle: 45°, PFR: 25 g/min, current: 80 A and table speed: 700 mm/min), showing no sign of cavity, and Figure C-4 shows the cross-sections of the wall built with the minimum peak points (offset: 9 mm, center gas:1 lpm, powder gas: 1.5 lpm, shielding gas: 10 lpm, nozzle angle: 0°, PFR: 30 g/min, current: 70 A and table speed: 600 mm/min), showing a great deal of cavity.



Figure C-3: Imaged of two cross-sections of the wall built with the maximum peak points.

Figure C-4: Images of two cross-sections of the wall built with the minimum peak points.

No proper reasoning was found as to why the circular and square cross-sectioned tubes did not have any cavity in them. Even though values in Figure C-2 recommended the best combination of process parameters that would minimize cavity, that combination was not used for all nine circular tubes and nine square tubes that followed. Nevertheless, no cavity was found in any of the second DOE's parts. Due to the lack of understanding of the source of cavity, it is recommended that this effect be explored in future work.

# Appendix D: Adhesion

Adhesion of the printed part to the substrate is another phenomenon that was occurring during the printing of the different AM parts. It is thought to mainly be dependent on heat input and powder feed rate, further experiments need to be conducted to confirm these assumptions. If very high residual stresses are present in the part, they can lead to poor adhesion between the surfaces. The thermal coefficient of expansion of 17-4PH stainless steel is 10.8 µm/m°C and 11.7 µm/m°C for carbon steel. Thus, the thermal coefficient of expansion between the 17-4PH stainless steel AM part and the carbon steel substrate can play a pivotal role in the quality of adhesion between the surfaces. It was concluded, however, that the quality of adhesion between the AM parts and the substrates had no direct impact on the mechanical properties of the final parts. The mechanical properties are solely correlated to the process parameters. Figure D-1 shows an example of a wall with full adhesion, while Figure D-2 shows a wall was less than 50% adhesion to the substrate. Further studies can be made on the effect of adhesion quality on geometrical tolerances of the final AM part; however, that is not the subject of the current thesis.



Figure D-1: Wall showing full adhesion to substrate.

Figure D-2: Wall showing partial adhesion to substrate.

# Appendix E: Final Wall Height vs. Process Parameters

Final wall height for all 18 walls was plotted against all eight process parameters used in the first DOE. Direct relationships between final wall height and powder feed rate and table speed were observed and discussed in Chapter 6. However, no direct relationship was found between final wall height and the other six process parameters, as given by the following graphs.
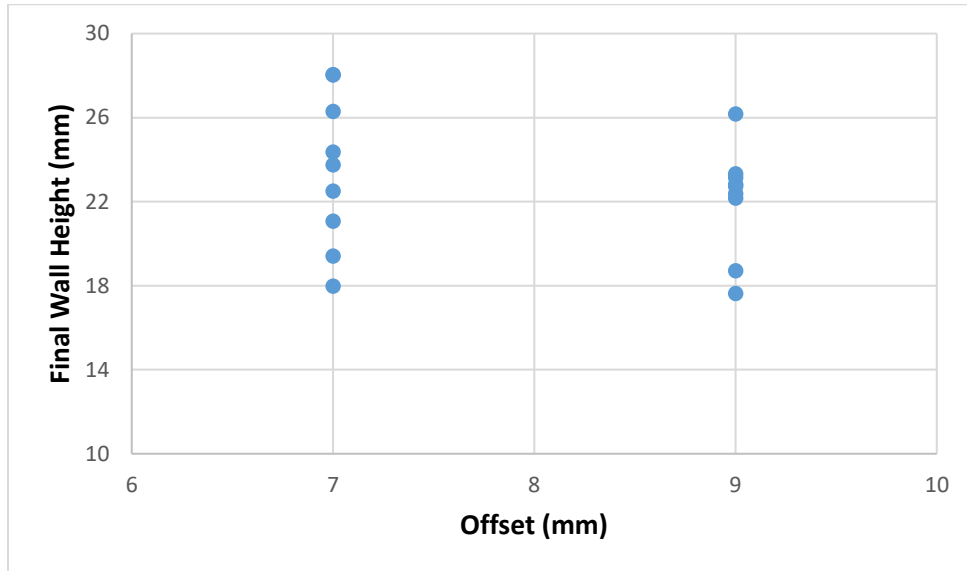


Figure E-1: Final wall height vs. offset for all 18 walls.
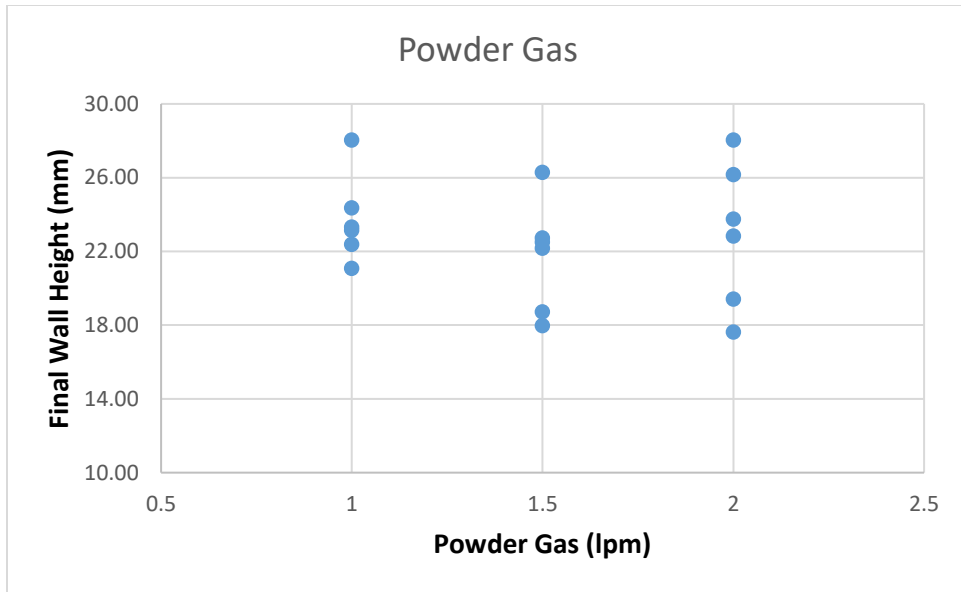
Figure E-2: Final wall height vs. powder gas for all 18 walls.
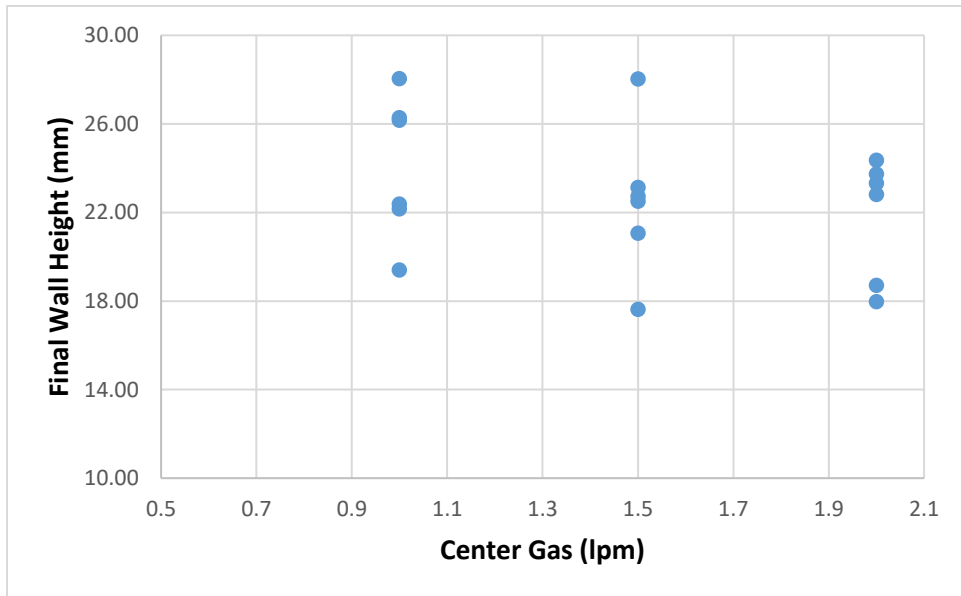


Figure E-3: Final wall height vs. center gas for all 18 walls.
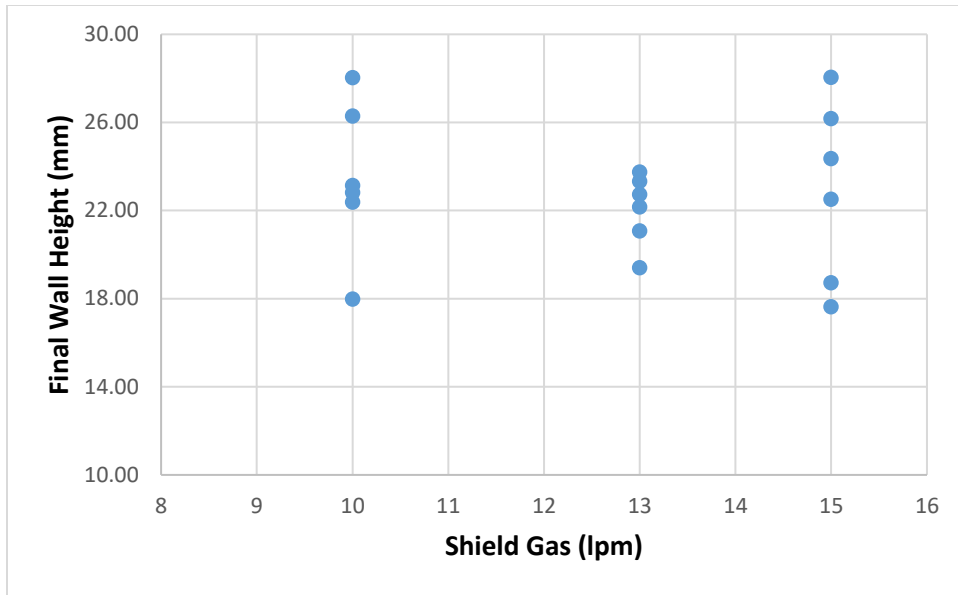
Figure E-4: Final wall height vs. center gas for all 18 walls.
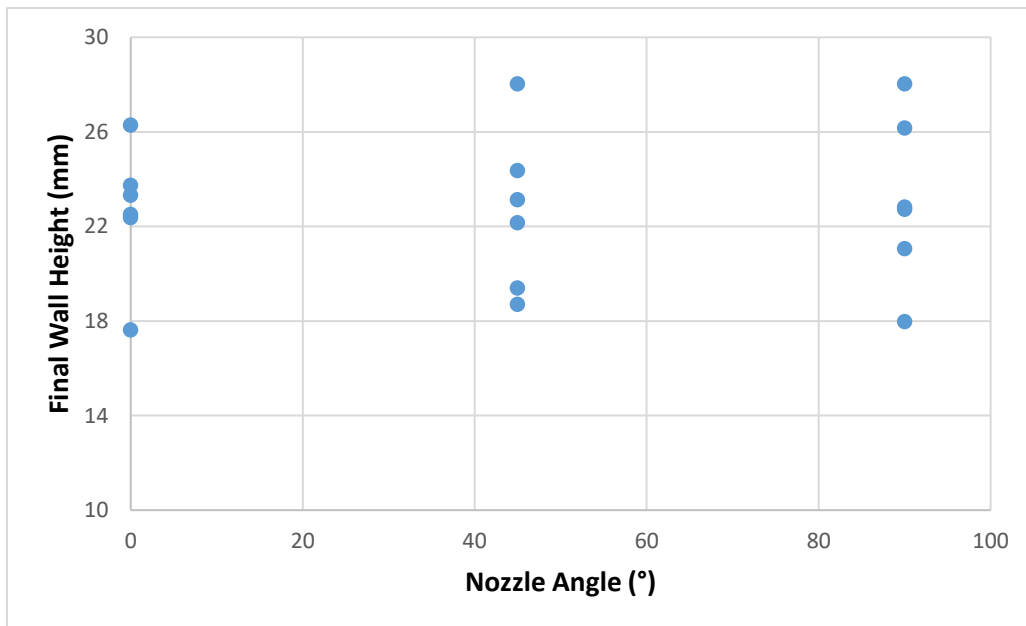


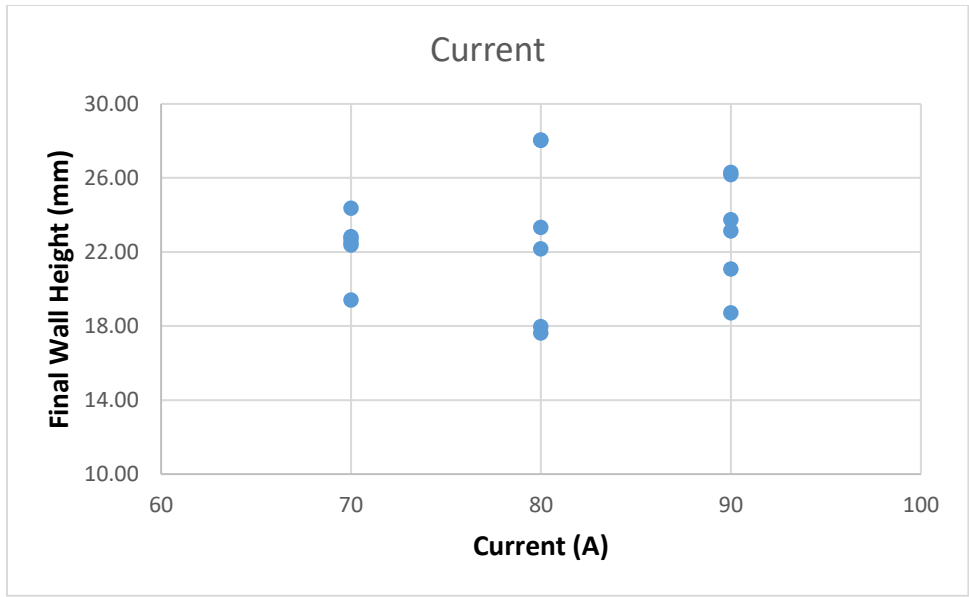Figure E-5: Final wall height vs. nozzle angle for all 18 walls.

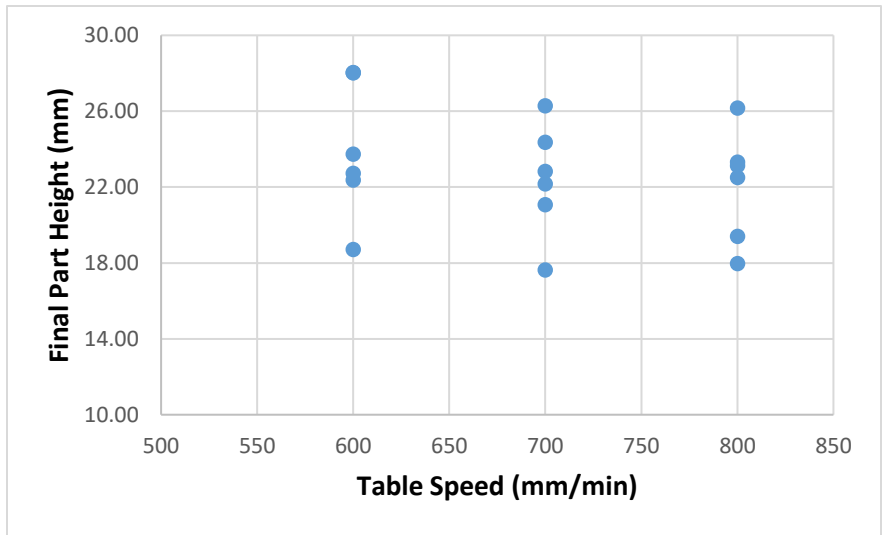Figure E-6: Final wall height vs. current for all 18 walls.



Figure E-7: Final wall height vs. table speed.

# Appendix F: Thermo-Calc

Thermo-Calc 2019b (database: TCFE10) was used to determine the heat of fusion for 17-4PH stainless steel, Figure F-1. It was also used to try and produce a phase diagram with equilibrium cooling (Figure F-2) and with Gulliver-Scheil solidification (Figure F-3). However, an equilibrium phase diagram is not representative of the actual conditions that take place during fast cooling rates in AM processes. Additionally, Gulliver-Scheil solidification did not provide all the information needed as it does not provide information pertaining to aging conditions. It is assumed in Gulliver-Scheil that no diffusion takes place in solid, which is opposite to the process of precipitation in aging heat treatments.
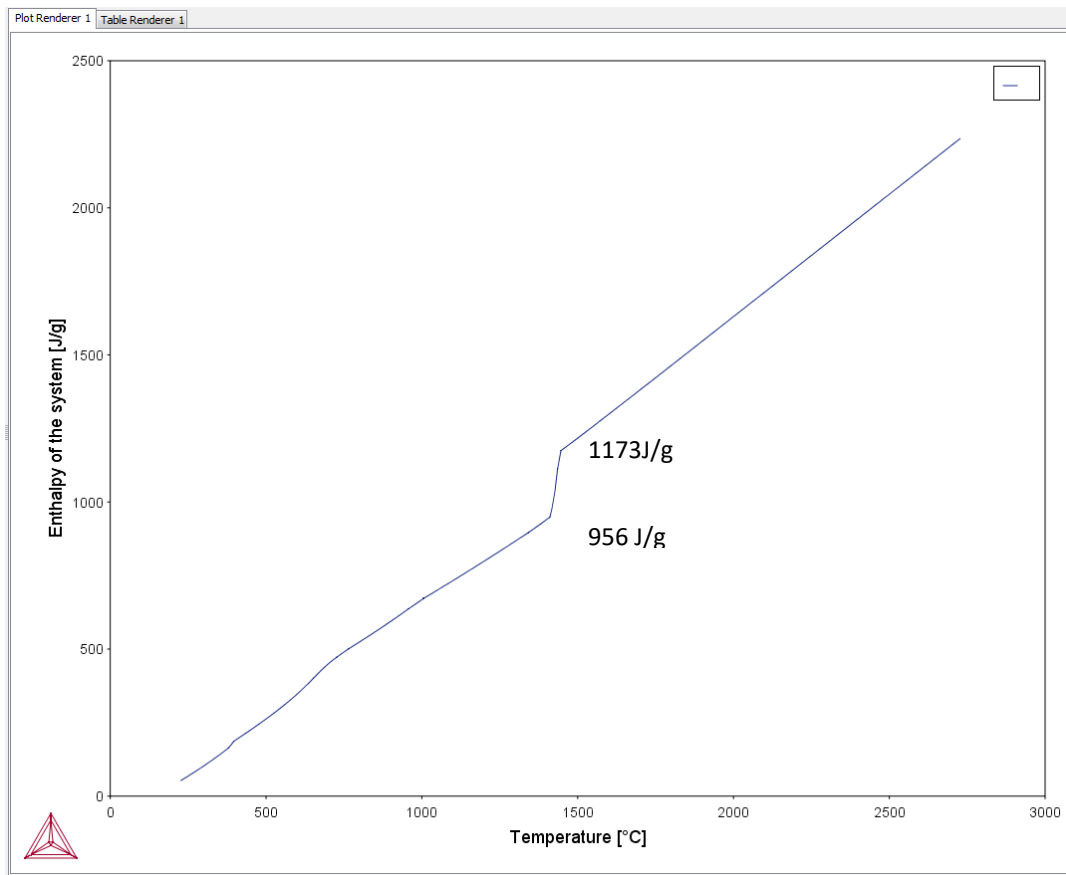


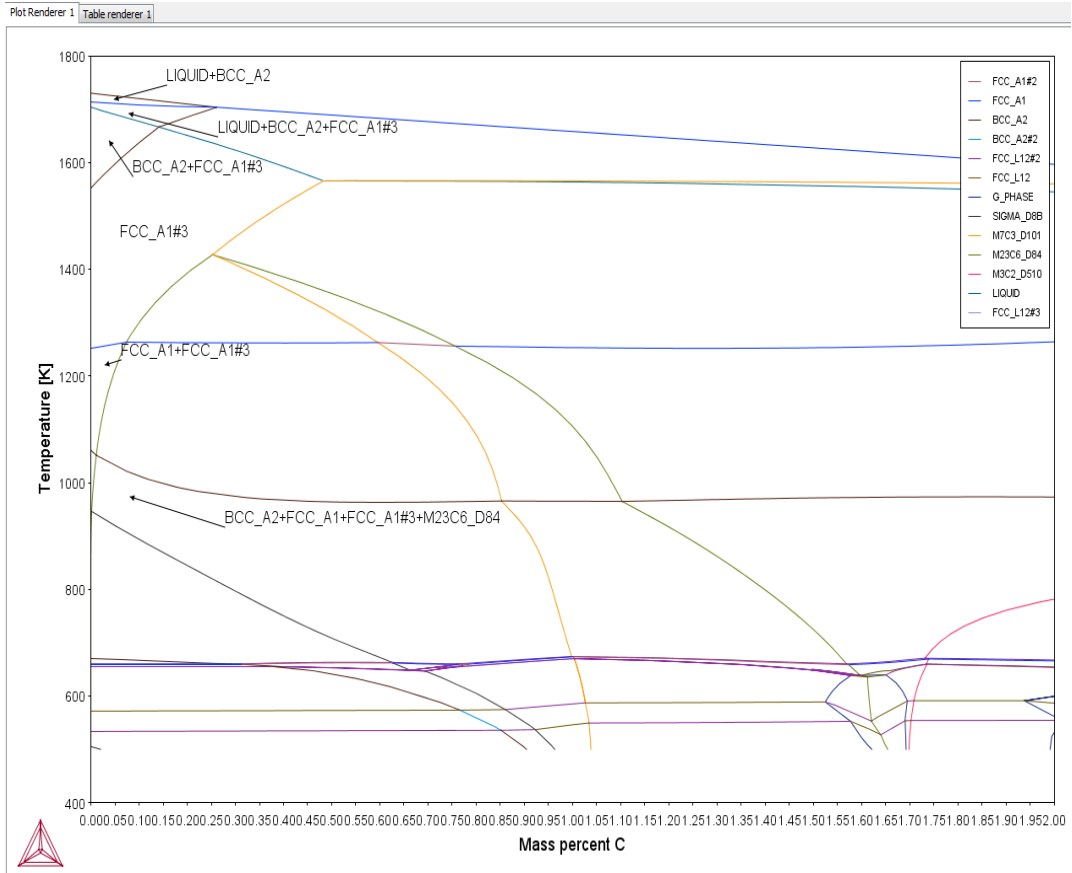Figure F-1: Temperature vs. enthalpy per gram for 17-4PH stainless steel.

Figure F-2: Pseudo binary Equilibrium phase diagram of 17-4PH stainless steel. The following chemical composition was used: C (0.07), Mn (1), Si (1), Cr (16.25), Ni (4), Cu (4), S (0.03), P (0.04), Nb+Ta (0.3), O (0.06), N (0.02) and a balance of Fe.
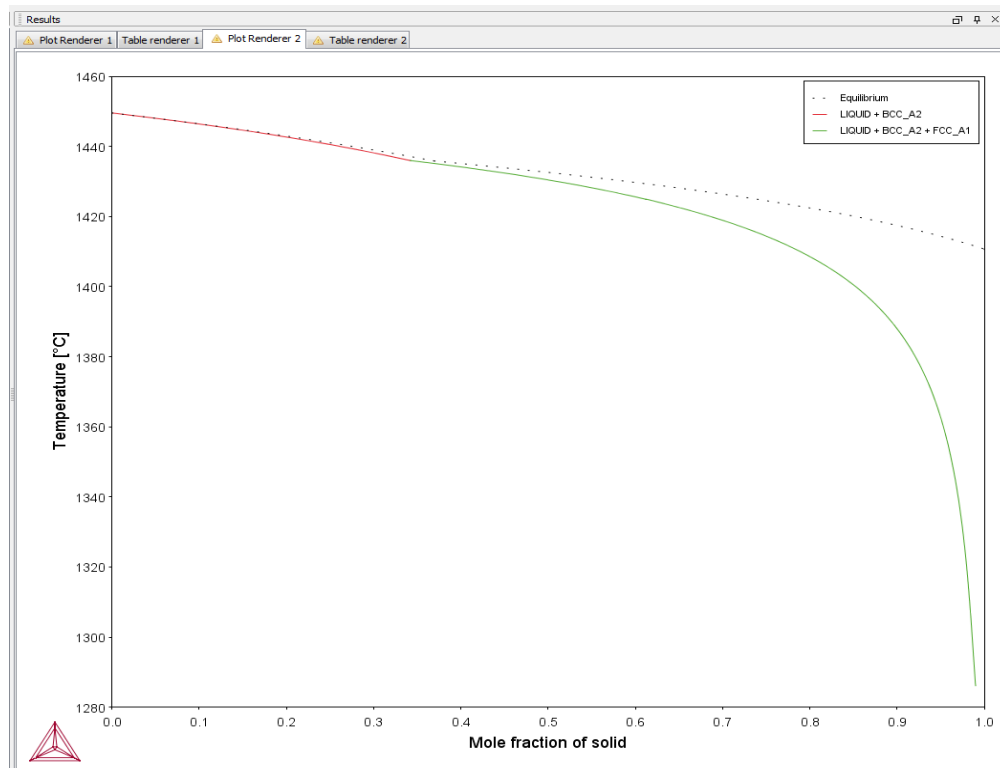
Figure F-3: Gulliver-Scheil solidification diagram for 17-4PH stainless steel.

# Appendix G: Hardness vs. Eight Process Parameters from First DOE

Hardness results were plotted against all eight process parameters for all 18 walls from the first DOE. No direct correlation between hardness and any of the process parameters is found as given by the graphs below.
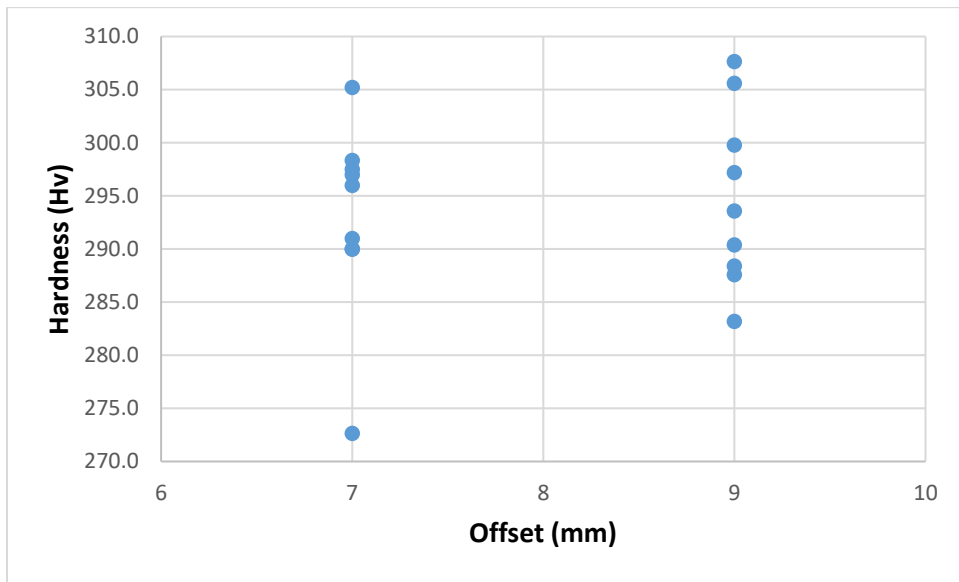


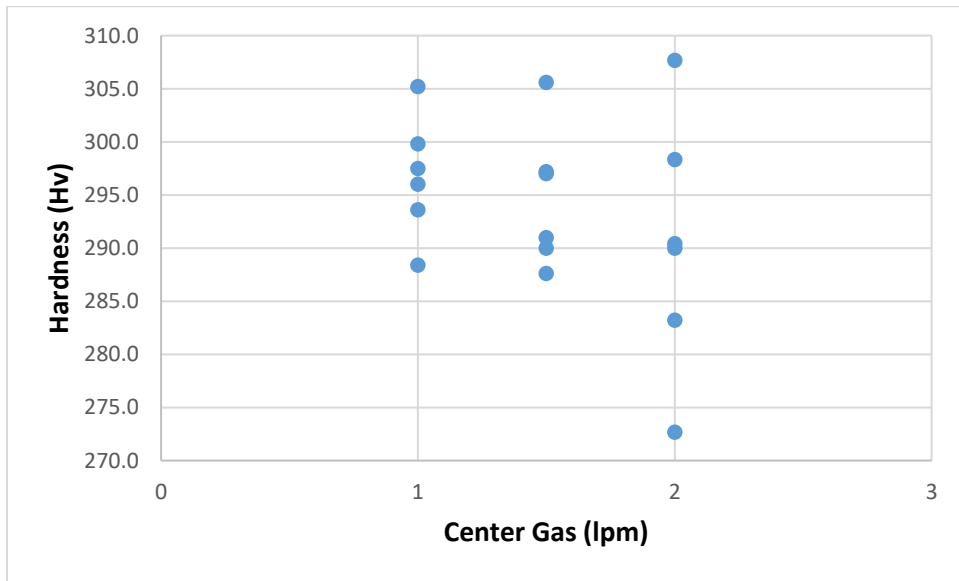Figure G-1: Hardness vs. offset for all 18 walls.



Figure G-2: Hardness vs. center gas for all 18 walls.
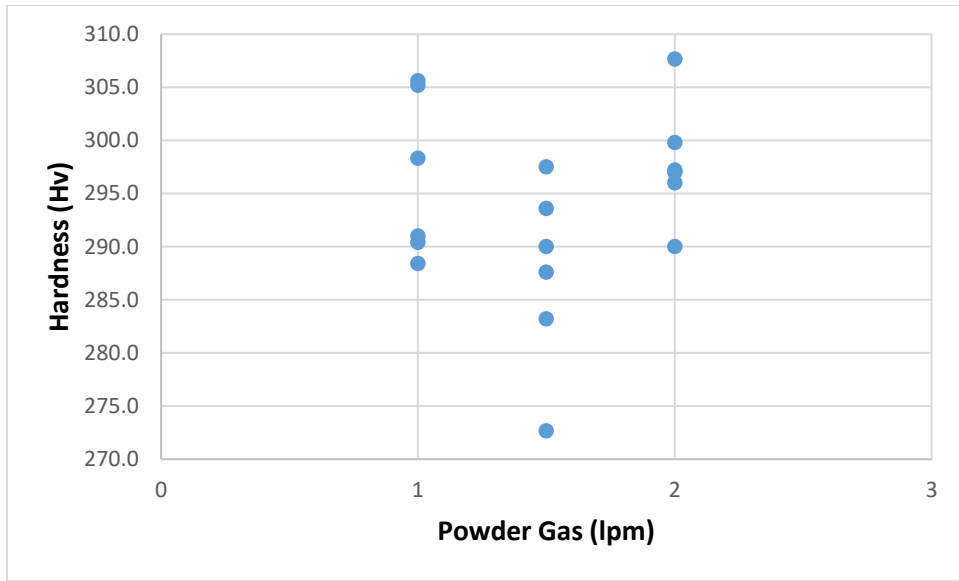
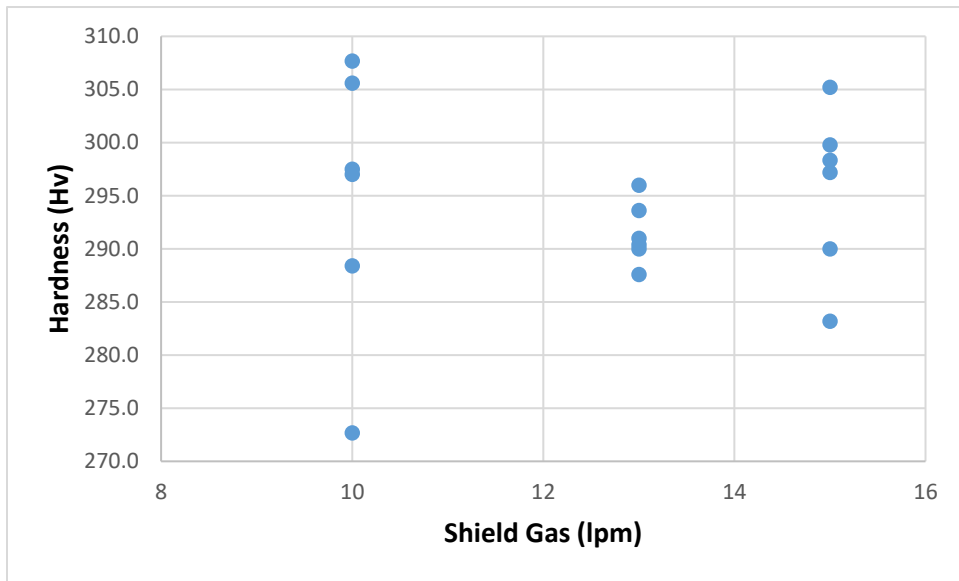Figure G-3: Hardness vs. powder gas for all 18 walls.



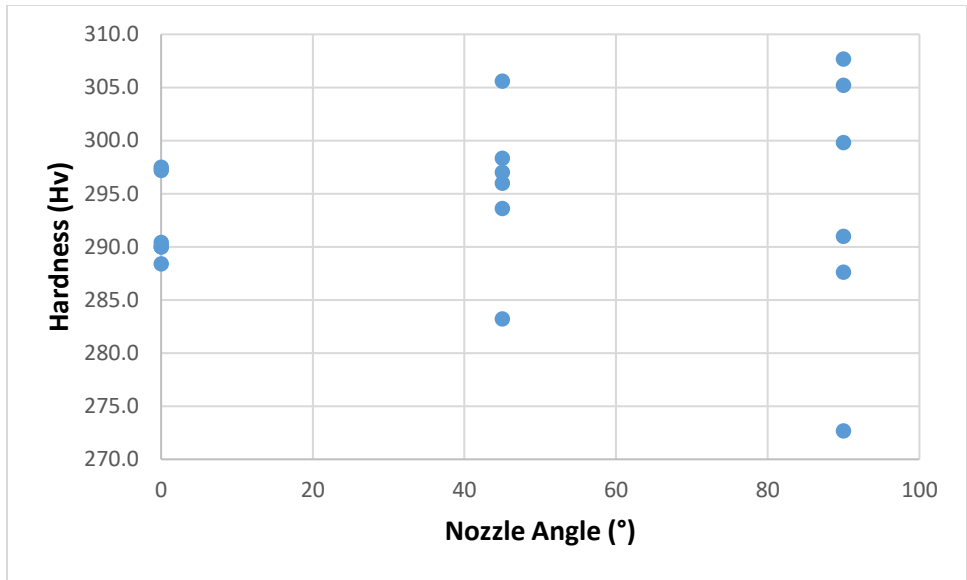Figure G-4: Hardness vs. shield gas for all 18 walls.

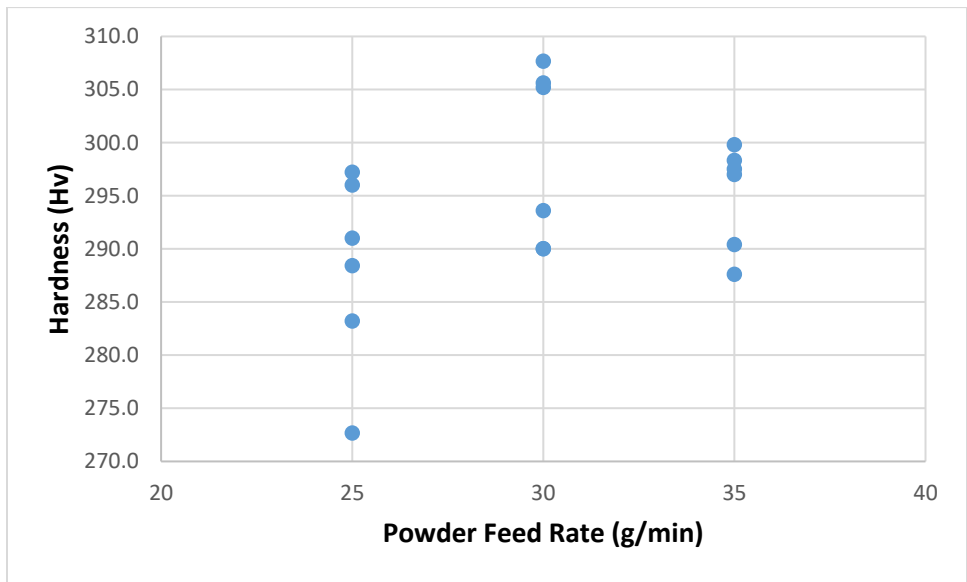Figure G-5: Hardness vs. nozzle angle for all 18 walls.



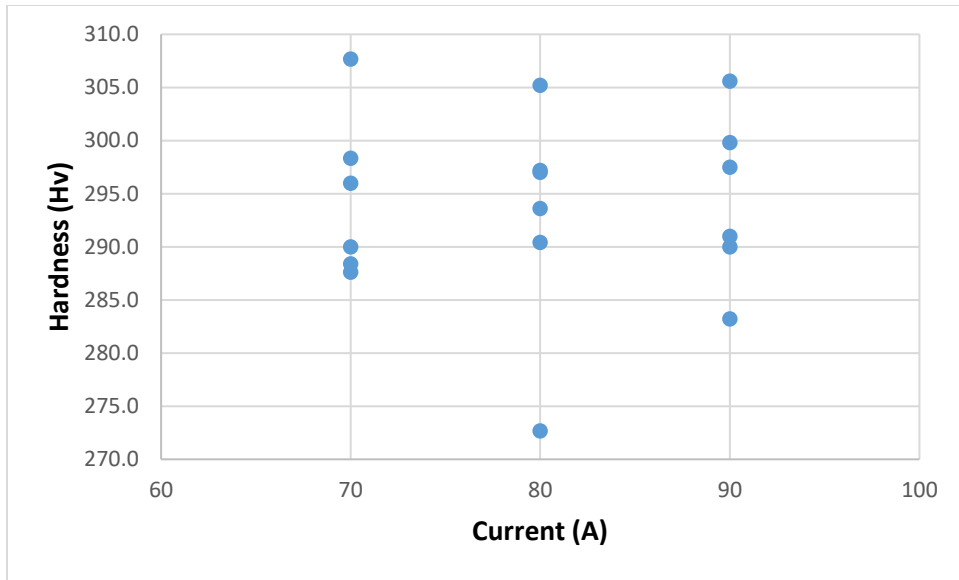Figure G-6: Hardness vs. powder feed rate for all 18 walls.

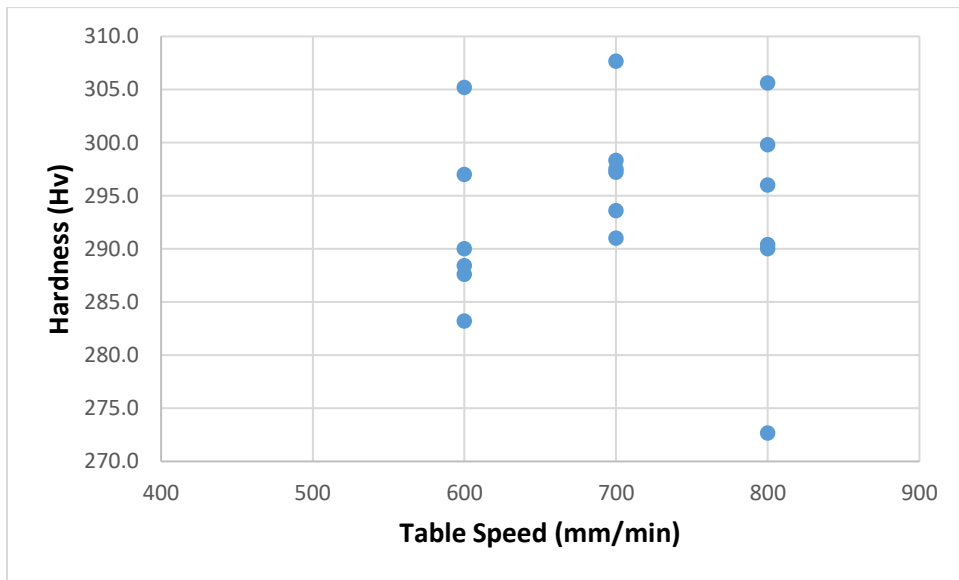Figure G-7: Hardness vs. current for all 18 walls.



Figure G-8: Hardness vs. table speed for all 18 walls.

# Appendix H: Minitab Results

This appendix shows all the results obtained from Minitab's signal to noise ratio for the wall height, wall thickness, adhesion to substrate, cavity, porosity and surface roughness from the walls' Taguchi L'18 DOE. Each figure ranks the order of the most influential parameters for each individual result based on the obtained value. It also provides the optimized value for each parameter that maximizes/minimizes the value of each collected result.

Response Table for Signal to Noise Ratios (Wall Height)
**Smaller is better**

| Level | Offset | Center | Powder | Shield | Nozzle | PFR | Current | Speed |
|-------|--------|--------|--------|--------|--------|--------|---------|--------|
| 1 | -8.653 | -9.937 | -9.908 | -11.117 | -10.153 | -3.232 | -6.929 | -11.023 |
| 2 | -9.628 | -8.814 | -7.954 | -5.574 | -7.533 | -10.546 | -11.161 | -8.770 |
| 3 | | -8.670 | -9.559 | -10.730 | -9.736 | -13.644 | -9.332 | -7.628 |
| Delta | 0.975 | 1.267 | 1.954 | 5.544 | 2.620 | 10.413 | 4.232 | 3.395 |
| **Rank** | 8 | 7 | 6 | 2 | 5 | 1 | 3 | 4 |



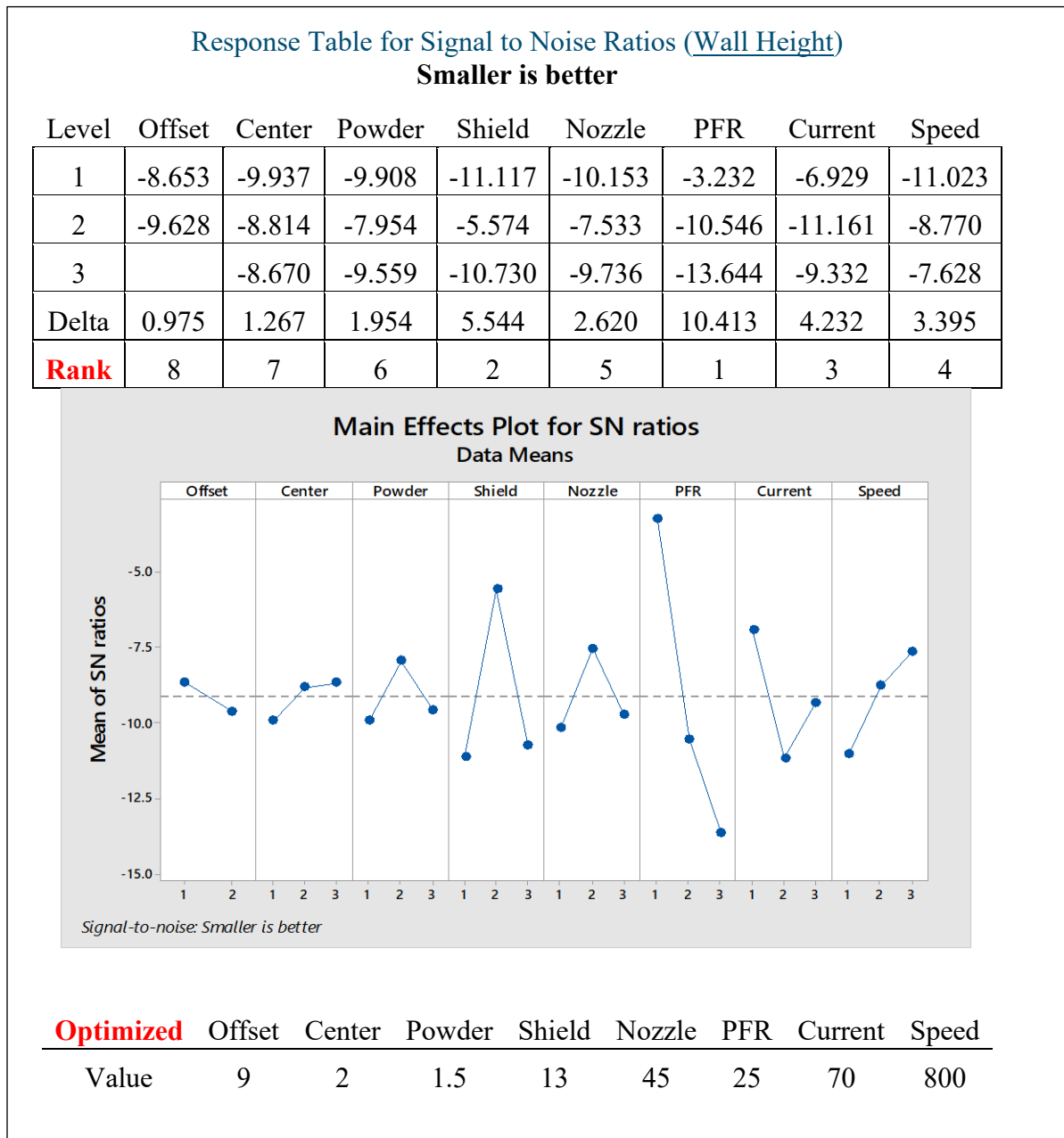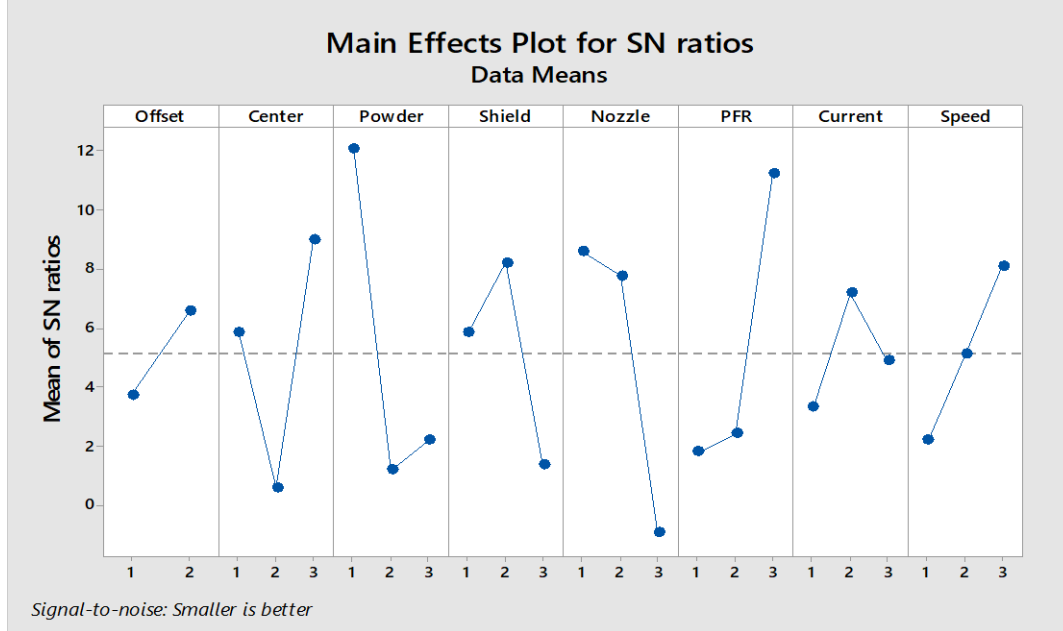| **Optimized** | Offset | Center | Powder | Shield | Nozzle | PFR | Current | Speed |
|-----------|--------|--------|--------|--------|--------|-----|---------|-------|
| Value | 9 | 2 | 1.5 | 13 | 45 | 25 | 70 | 800 |

Figure H-1: Response table for wall height and optimized values using Minitab.

Response Table for Signal to Noise Ratios (Wall thickness)

**Smaller is better**

| Level | Offset | Center | Powder | Shield | Nozzle | PFR | Current | Speed |
|-------|--------|--------|--------|--------|--------|--------|---------|--------|
| 1 | 3.7099 | 5.8175 | 12.0413 | 5.8523 | 8.5813 | 1.7815 | 3.3142 | 2.1798 |
| 2 | 6.5430 | 0.5923 | 1.1693 | 8.1981 | 7.7516 | 2.3919 | 7.1852 | 5.0904 |
| 3 | | 8.9696 | 2.1688 | 1.3290 | -0.9535 | 11.2060 | 4.8800 | 8.1091 |
| Delta | 2.8332 | 8.3772 | 10.8719 | 6.8690 | 9.5349 | 9.4244 | 3.8711 | 5.9293 |
| **Rank** | 8 | 4 | 1 | 5 | 2 | 3 | 7 | 6 |



| **Optimized** | Offset | Center | Powder | Shield | Nozzle | PFR | Current | Speed |
|---------------|--------|--------|--------|--------|--------|-----|---------|-------|
| Value | 7 | 2 | 1 | 13 | 0 | 35 | 80 | 800 |

Figure H-2: Response table for wall thickness and optimized values using Minitab.

## Response Table for Signal to Noise Ratios (Adhesion to Substrate)
### Larger is better

| Level | Offset | Center | Powder | Shield | Nozzle | P.F.R. | Current | Speed |
|-------|--------|--------|--------|--------|--------|--------|---------|-------|
| 1 | -2.79266 | -2.59560 | -2.16326 | -0.20160 | 0.00000 | 0.00000 | -3.75664 | -2.50839 |
| 2 | -1.44217 | -1.95009 | -3.42908 | -3.42908 | -3.08395 | -2.23890 | -2.03730 | -3.28555 |
| 3 | | -1.80656 | -0.75991 | -2.72156 | -3.26830 | -4.11335 | -0.55830 | -0.55830 |
| Delta | 1.35049 | 0.78904 | 2.66917 | 3.22748 | 3.26830 | 4.11335 | 3.19834 | 2.72724 |
| **Rank** | 7 | 8 | 6 | 3 | 2 | 1 | 4 | 5 |



| **Optimized** | Offset | Center | Powder | Shield | Nozzle | PFR | Current | Speed |
|---------------|--------|--------|--------|--------|--------|-----|---------|-------|
| Value | 7 | 2 | 2 | 10 | 0 | 25 | 90 | 800 |
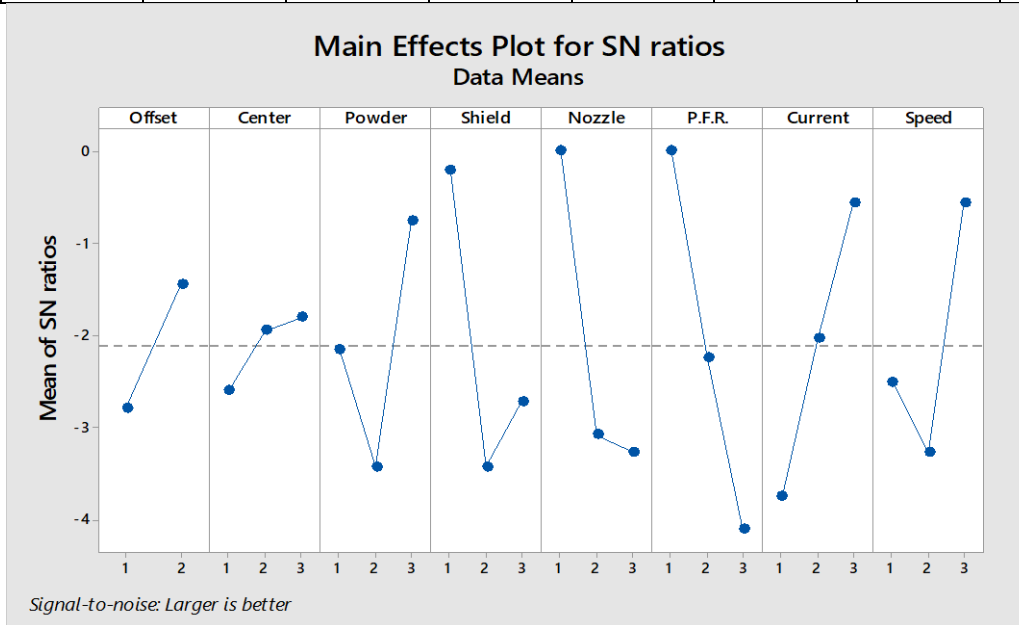
Figure H-3: Response table for adhesion to substrate and optimized values using Minitab.

**Smaller is better**

| Level | Offset | Center | Powder | Shield | Nozzle | PFR | Current | Speed |
|-------|--------|--------|--------|--------|--------|-----|---------|-------|
| 1 | -14.685 | -17.460 | -13.195 | -10.772 | -10.825 | -18.811 | -19.888 | -16.063 |
| 2 | -12.262 | -11.155 | -15.601 | -14.368 | -14.275 | -14.214 | -7.372 | -17.333 |
| 3 | | -10.476 | -9.773 | -23.399 | -15.441 | -4.082 | -16.367 | -8.636 |
| Delta | 2.423 | 6.984 | 5.829 | 12.627 | 4.615 | 14.730 | 12.516 | 8.698 |
| **Rank** | 8 | 5 | 6 | 2 | 7 | 1 | 3 | 4 |



| **Optimized** | Offset | Center | Powder | Shield | Nozzle | PFR | Current | Speed |
|-----------|--------|--------|--------|--------|--------|-----|---------|-------|
| Value | | 7 | 2 | 2 | 10 | 0 | 35 | 80 | 800 |
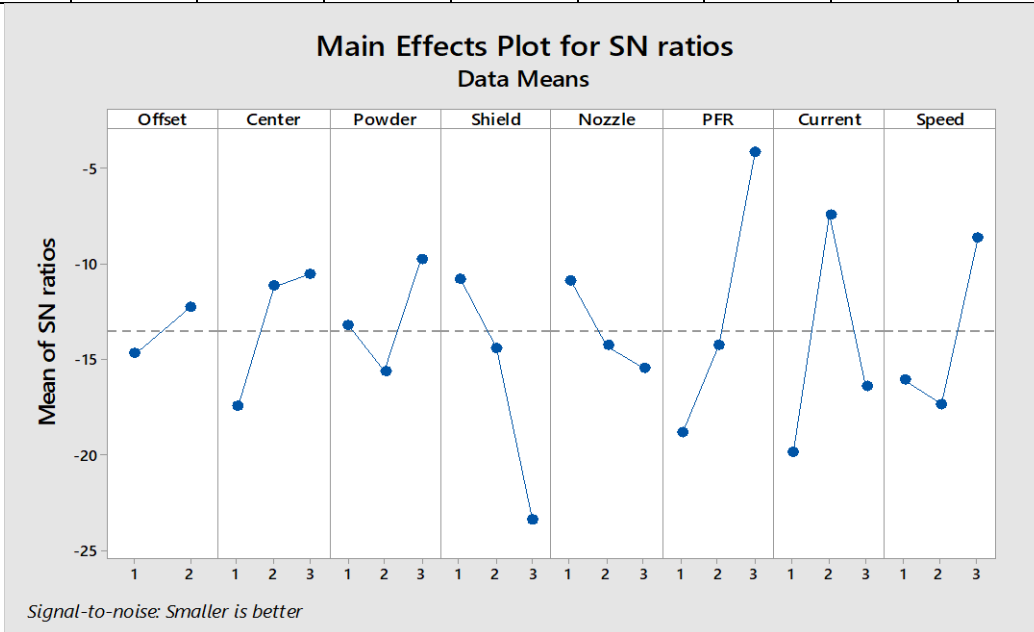
Figure H-4: Response table for cavity and optimized values using Minitab.

## Response Table for Signal to Noise Ratios (Porosity)
### Smaller is better

| Level | Offset | Center | Powder | Shield | Nozzle | PFR | Current | Speed |
|-------|--------|--------|--------|--------|--------|-------|---------|-------|
| 1 | 4.457 | 4.269 | 5.086 | 4.059 | 4.591 | 9.470 | 3.965 | 3.684 |
| 2 | 6.928 | 6.766 | 4.978 | 7.648 | 6.591 | 2.691 | 6.984 | 7.763 |
| 3 | | 6.043 | 7.012 | 5.370 | 5.896 | 4.916 | 6.128 | 5.631 |
| Delta | 2.471 | 2.497 | 2.034 | 3.589 | 2.001 | 6.779 | 3.019 | 4.079 |
| **Rank** | 6 | 5 | 7 | 3 | 8 | 1 | 4 | 2 |



| **Optimized** | Offset | Center | Powder | Shield | Nozzle | PFR | Current | Speed |
|---------------|--------|--------|--------|--------|--------|-----|---------|-------|
| Value | | 7 | 1.5 | 2 | 13 | 45 | 25 | 80 | 700 |
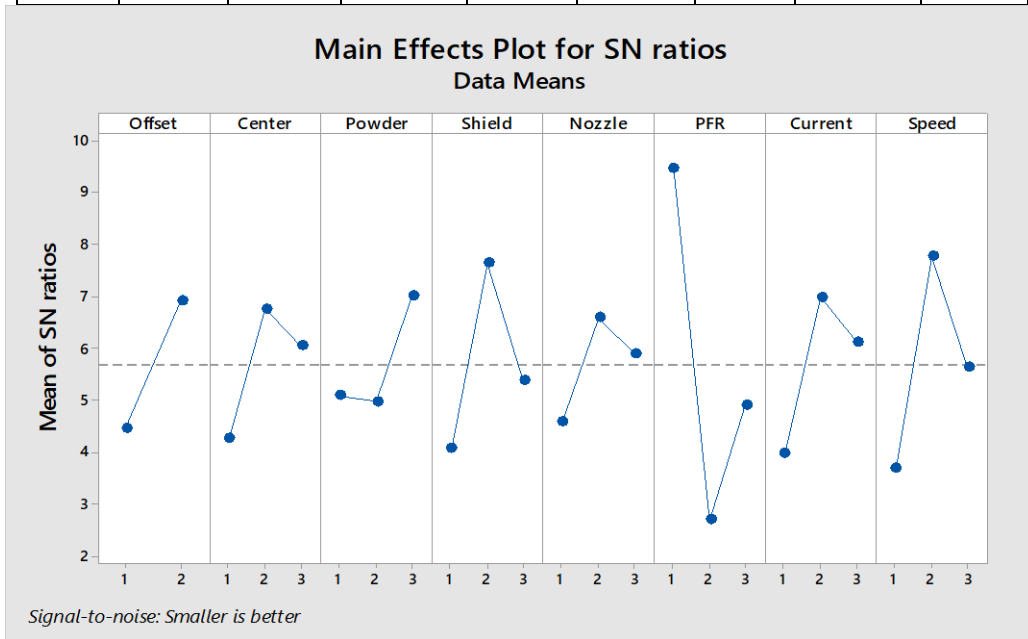
Figure H-5: Response table for porosity and optimized values using Minitab.

## Response Table for Signal to Noise Ratios (Maximum Wall Deviation)
### Smaller is better

| Level | Offset | Center | Powder | Shield | Nozzle | PFR | Current | Speed |
|-------|--------|--------|--------|--------|--------|--------|---------|--------|
| 1 | -3.163 | -2.885 | -5.276 | -4.693 | -3.639 | -6.467 | -3.201 | -3.697 |
| 2 | -5.018 | -5.178 | -3.736 | -3.330 | -5.302 | -3.585 | -4.234 | -4.602 |
| 3 | | -4.208 | -3.260 | -4.248 | -3.330 | -2.220 | -4.837 | -3.972 |
| Delta | 1.855 | 2.293 | 2.016 | 1.362 | 1.971 | 4.247 | 1.636 | 0.905 |
| **Rank** | 5 | 2 | 3 | 7 | 4 | 1 | 6 | 8 |



Main Effects Plot for SN ratios
Data Means
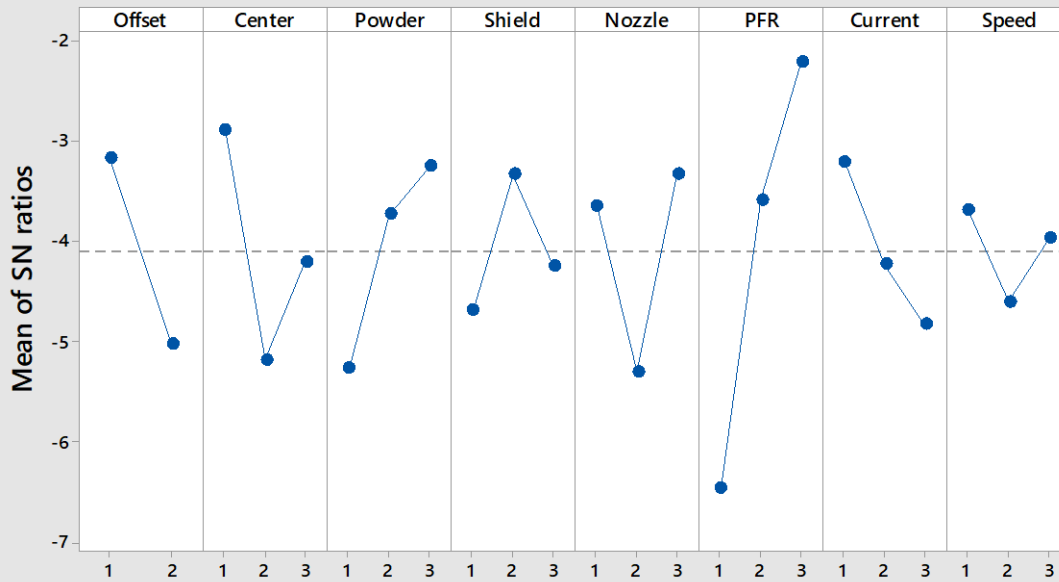
| **Optimized** | Offset | Center | Powder | Shield | Nozzle | PFR | Current | Speed |
|---------------|--------|--------|--------|--------|--------|-----|---------|-------|
| Value | 9 | 1 | 2 | 13 | 90 | 35 | 70 | 600 |

Figure H-6: Response table for wall height and optimized values using Minitab.

# Appendix I: Second DOE Process Parameters

For the circular and square tubes from the second DOE, porosity results were collected and concluded that they were not dependent on any of the three variable process parameters. Figure I-1, Figure I-2 and Figure I-3 show no linear or inverse relationships between porosity and the three parameters. Additionally, Figure I-4 and Figure I-5 show hardness vs. current and powder feed rate. No direct relationship is found between either parameter and hardness.
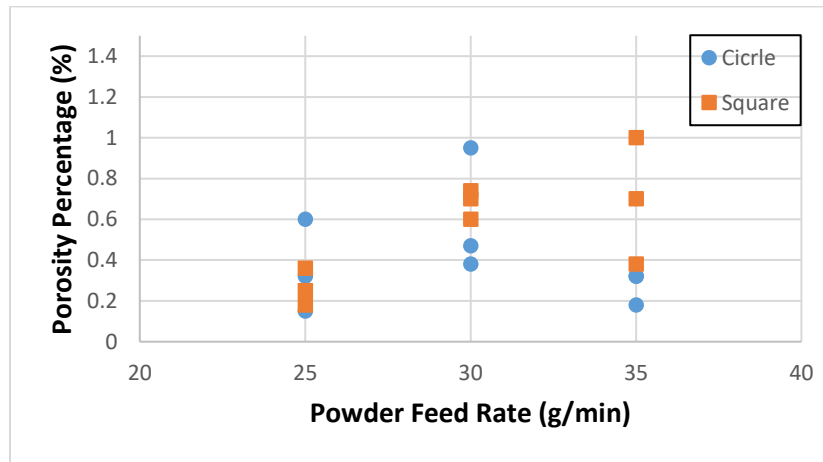


Figure I-1: Porosity percentage vs. powder feed rate for all circular and square tubes.
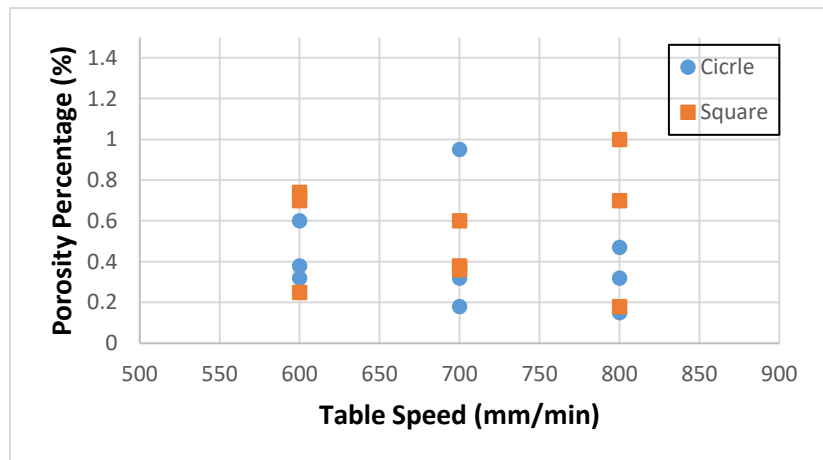


Figure I-2: Porosity percentage vs. table speed for all circular and square tubes.
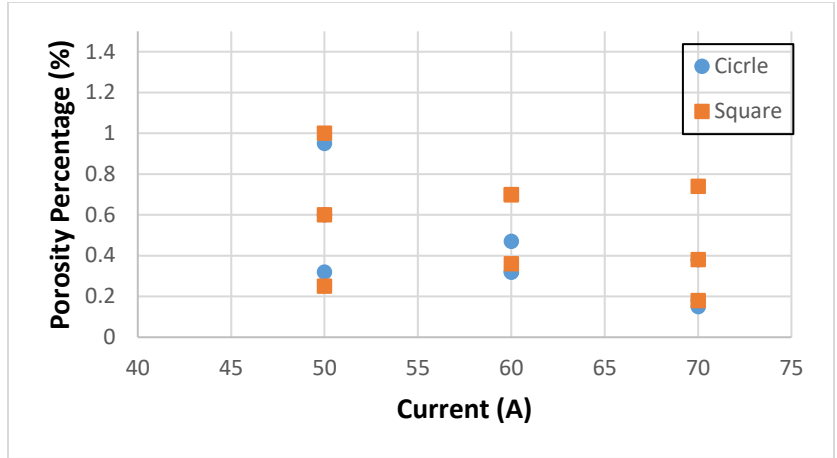
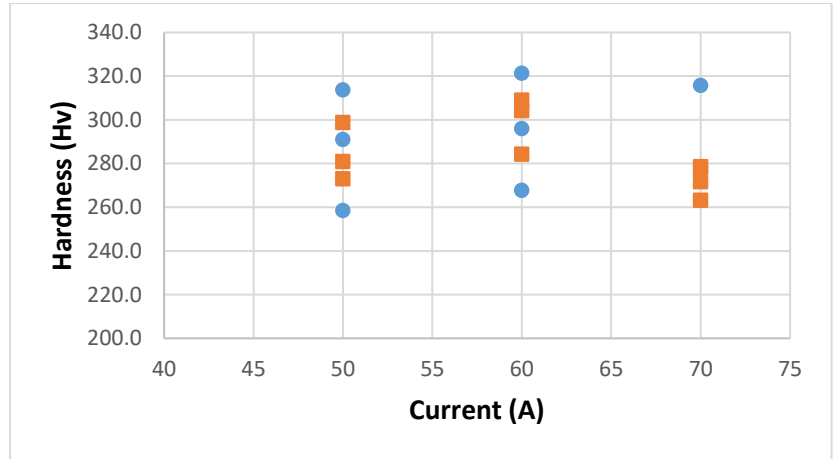Figure I-3: Porosity percentage vs. current for all circular and square tubes.



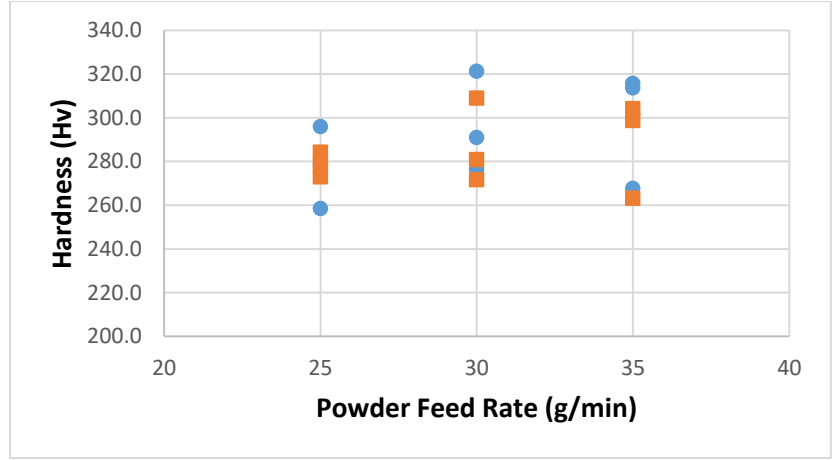Figure I-4: Hardness vs. current for all circular and square tubes.



Figure I-5: Hardness vs. powder feed rate for all circular and square tubes.

# Appendix J: Tensile Fracture Mechanisms

Examples of tensile fracture mechanisms obtained from square tube 2-7 from the second DOE are shown in Figure J-1. A more detailed analysis to correlate fracture mechanisms to tensile properties is required. Figure J-2 shows the stress-strain curves of square tube 2-7 in the four different heating conditions. All the samples underwent complete ductile fracture and have ultimate tensile strengths within the expected values of conventionally manufactured 17-4PH stainless steel. However, the Young's modulus of the four conditions is one order of magnitude lower than what it should be. A thorough analysis of the calculations was made, but no errors were found. The Instron machine is regularly calibrated, so it is unlikely that the source of error is from the machine. However, the extension that is collected for all the samples is a factor of 10 higher than it should be. The source of this x10 factor is unknown and should be further researched. An incorrect Young's modulus is usually correlated to an error during the tensile testing process. Because the samples were miniature samples, no extensometer was used. For this reason, the extension computed for each condition was actually the displacement of the grips. Any slippage that occurs during testing is considered a part of the extension, yielding incorrect results. However, no gripping marks are apparent on the surface of the samples.

Results from the percentage area reduction was calculated for all eight samples; however, some of the samples showed comparable area reduction to wrought stainless steel while others showed little to no ductility (see Table J-1). The method used for area reduction was not completely accurate since areas were only measured after fracture and not before, allowing for a margin of error when back tracking the original dimensions from fractured samples. The lack of a usage of an extensometer, inaccurate method used to calculate reduced area and the need for more data collection from tensile samples make the current tensile analysis incomplete, as stated in Chapter 6. Moreover, a further understanding of the effect of using the UTS extension calculations has on young's modulus should be conducted.

Figure J-1: Tensile fracture mechanisms of three samples from the second DOE. From left to right, sample numbers are square tubes 2-7 CA and 2-7 H900.
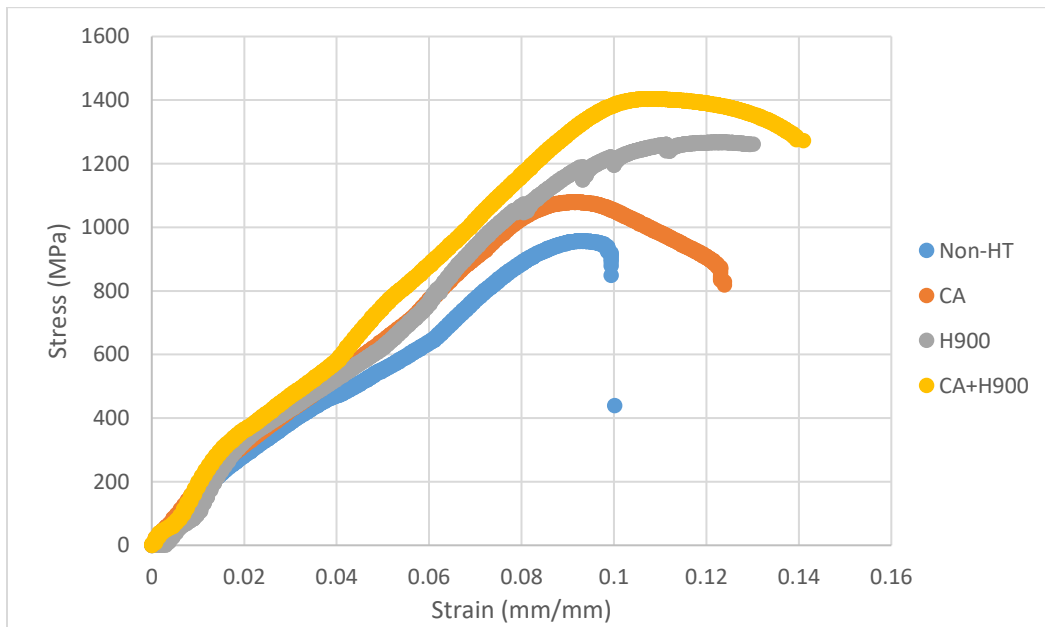


Figure J-2: Stress vs. Strain graph of square tube 2-7 in four different heating conditions.

Table J-1: Reduced area percentages for each of the square tube 2-7 from Chapter 6.

| ID | Reduced Area % |
|---|---|
| 7 Non-HT | 6.21 |
| 7 CA | 0.97 |
| 7 CA H900 | 12.22 |
| 7 H900 | 3.58 |

# Appendix K: FIB Images

Below are images from the sections that were ion milled using the FIB milling process. Figure K-1 shows two sections that were ion milled. Figure K-2 is a higher magnification of one of the milled surfaces.
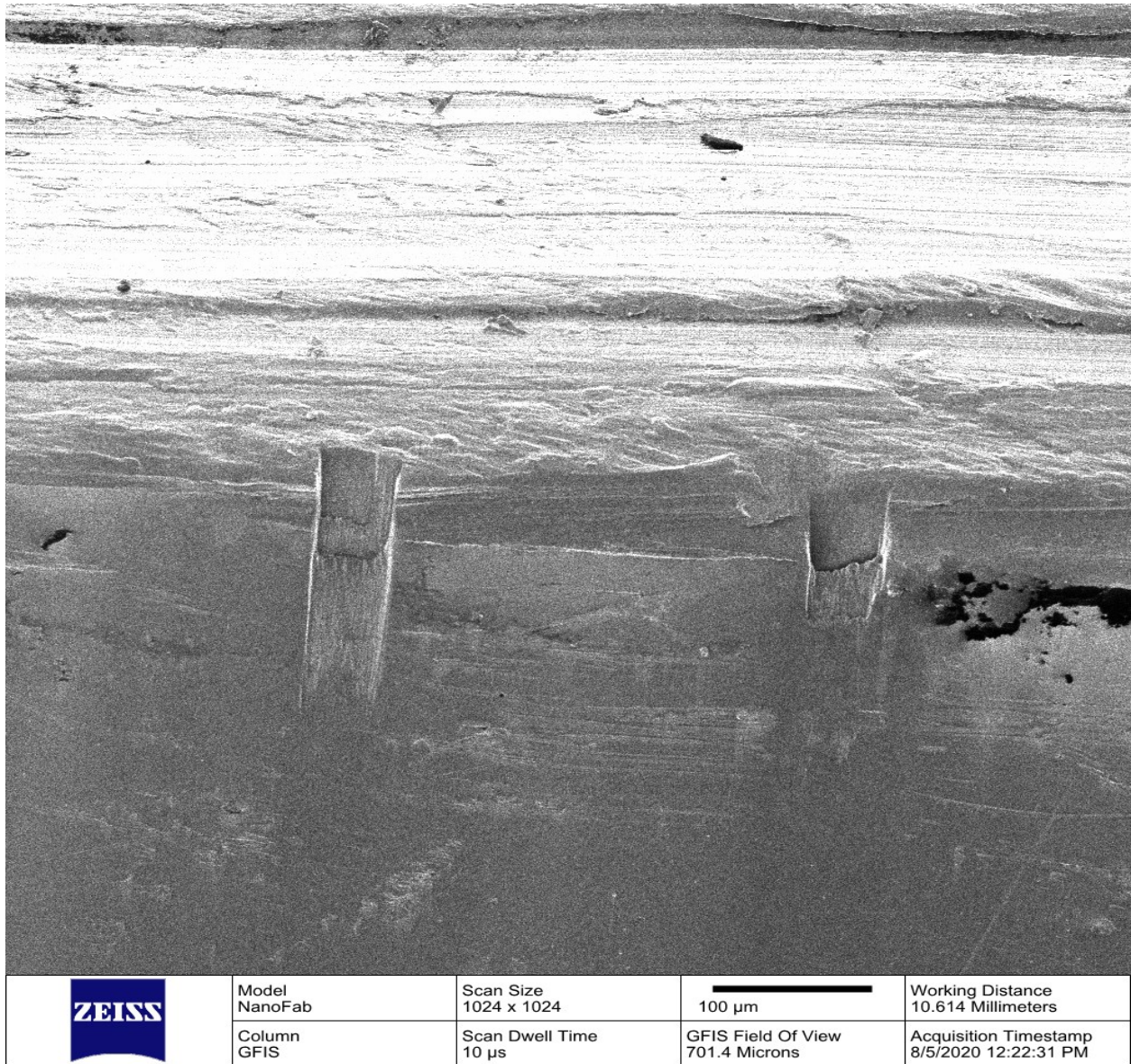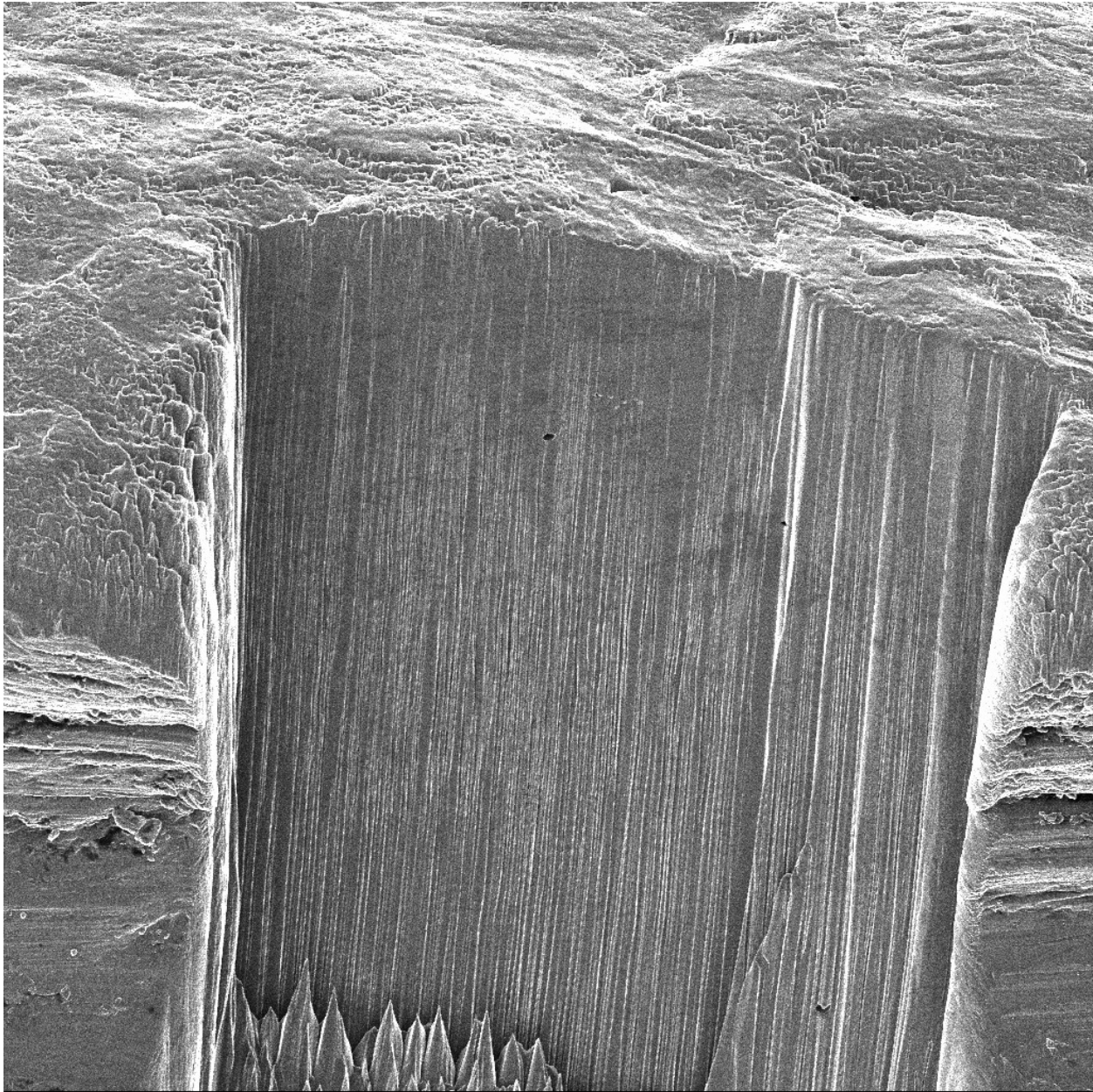


| | | Model NanoFab | Scan Size 1024 x 1024 | 100 μm | Working Distance 10.614 Millimeters |
| ZEISS | | Column GFIS | Scan Dwell Time 10 μs | GFIS Field Of View 701.4 Microns | Acquisition Timestamp 8/5/2020 12:22:31 PM |

Figure K-1: Two milled surfaces using the FIB milling process.

| ZEISS | Model NanoFab | Scan Size 1024 x 1024 | ▬▬ 10 µm | Working Distance 9.902 Millimeters |
| | Column GFIS | Scan Dwell Time 10 µs | GFIS Field Of View 65 Microns | Acquisition Timestamp 8/5/2020 12:26:46 PM |

Figure K-2: A higher magnification of one of the milled surfaces.